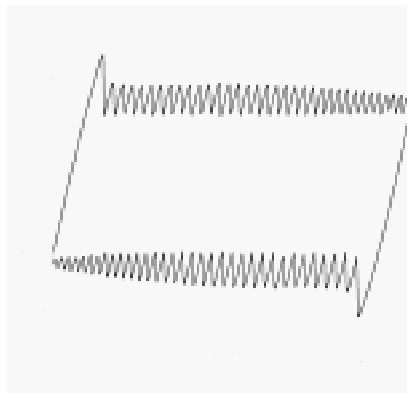VETENSKAP
OCH
KONST

KTH

Force measurements using Scanning Probe Microscopy

Anders Meurk

Stockholm 2000

The Brinell Centre
Inorganic Interfacial Engineering

KTH

Force measurements using Scanning Probe Microscopy

Applications to advanced powder processing

Anders Meurk

YKI

YTKEMISKA INSTITUTET
Institute for Surface Chemistry

Akademisk avhandling

Stockholm 2000

Address to the author:

Anders Meurk
Institute for Surface Chemistry
P. O. Box 5607
SE-114 86 Stockholm
SWEDEN

Front cover: Friction loop showing stick-slip motion (*cf*. Paper V)

Back cover: Being a PhD-student, it is sometimes difficult to separate work from spare time. The top pyramid is fairly new and quite small, whereas the bottom pyramid is extremely old and enormous (photo by the author on location in Stockholm, Sweden and La Reserva Biosférica Maya, Guatemala).

ABSTRACT

The object of this thesis is to apply scanning probe microscopy (SPM) to the field of advanced powder processing. Measurement of interparticle surface forces at conditions relevant to ceramic processing has been performed together with thorough studies of powder friction.

Surface force measurements between silicon nitride and silica surfaces in 1-bromonaphtalene and diiodomethane resulted in an attractive van der Waals force in both media for the symmetric systems and a repulsive van der Waals force for the asymmetric systems. This agreed well with theoretical predictions from Lifshitz theory. Measurements in electrolyte solutions between silicon nitride surfaces with a varying degree of oxidation showed that silanol groups dominated the interactions at a high degree of oxidation, whereas the influence of amine species became stronger after surface etching. Surface charge, surface potential and density of surface groups have been extracted from DLVO computer modelling of the experimental force curves. Surface force measurements have been carried out using a nitrided silica sphere as a colloidal probe, representative for commercial silicon nitride powders. Adsorption of poly(acrylic acid) above the isoelectric point generated a thin polymer layer of an essentially flat conformation.

Friction force measurements were attainable via novel calibration procedures of both the lateral photodetector response and the cantilever torsional spring constant. Combining the method for detector calibration with evaluation of static friction slopes simplified the choice of appropriate contact mechanics theory to evaluate the friction measurements. Applying the method on friction measurements between iron surfaces coated with commercial lubricants showed a substantial surface deformation not seen from the friction force alone. The nanorheological properties of silica surfaces coated with two different stearic acids have been evaluated from friction force measurements. Steady sliding motion was replaced by highly regular stick-slip motion at a critical load and velocity. The stick-slip motion was successfully described and fitted to a phenomenological model. The contact area evaluated from Maugis-Dugdale theory revealed the contact diameter to be very close to the stick-slip periodicity.

Friction measurements were carried out between individual spray-dried ceramic granules as a function of binder concentration and relative humidity. The hygroscopic nature of the binder resulted in a higher adhesion force but lower friction coefficient with increasing humidity. This effect was ascribed to softening of the binder and a lowering of the shear strength of the binder rich surface layer on the granules. Comparison of the friction force between two granules and a granule and a hard metal surface confirmed that resistance to flow during the initial stages of powder pressing is dominated by granule–wall friction and adhesion.

Keywords: Atomic force microscope, AFM, SPM, van der Waals interaction, DLVO-theory, surface forces, colloidal probe, force curve, friction, adhesion, stick-slip, cantilever, calibration, spring constant, silicon nitride, iron, silica.

PREFACE

The thesis you are about to read is the essential work I have carried out since 1995 in the field of ceramic powder processing using a scanning probe microscope (SPM), more popularly known as an atomic force microscope (AFM). When I first set out on the path leading up to this thesis, by kick-starting with a year at Imperial College in London, my instructions from back home were clear, but also of the kind "learn about the AFM", "see what we can do", "get a feeling for it" etc. One of my first lessons in learning the technique was non-contact imaging of soft contact lenses in water. Not exactly being a trivial task, it resulted in a completely damaged piezo (it went "Bang!") and a few great days of London sightseeing waiting for the bill. Since then I have learned a lot, but still drop a $30 cantilever on the floor now and then.

I believe it is a privilege to be encouraged to have an open mind the first part of a PhD-studentship, and that kind of philosophy has followed me ever since. Adopting new AFM methods along the way, as well as trying out one's own ideas, has been a sheer pleasure. Diverting from the original PhD-proposal is probably inevitable, and I thought that happened a long time ago in my case. Looking at the proposal today, I am surprised to find most of the goals achieved, which is obviously thanks to Lennart keeping track of me. Without his guidance, I would certainly have wandered straight away from colloid science and ceramic technology, playing with the AFM in some dark alley of experimental physics.

The AFM is still thriving after 15 years, and I hope after reading this thesis you spot the huge potential inherent to the technique. Imagine, for example, how some measurements presented here, in conjunction with a relevant model, could benefit from normal or lateral sinusoidal modulation of the surfaces. In this context it is my belief that the field of nanorheology - one of the most fundamentally unanswered questions is how energy is dissipated on the nanoscale - will develop as successfully as the colloidal probe technique for normal force measurements did a few years ago.

If that prophecy is fulfilled, maybe this thesis can serve as a basis for future projects.

Stockholm a rainy day the rainy summer of '00

Anders Meurk

LIST OF PAPERS

Papers listed chronologically below are included in the thesis and will be referred to by their Roman numerals.

I.   Anders Meurk, Paul F. Luckham and Lennart Bergström
"Direct Measurement of Repulsive and Attractive van der Waals Forces between Inorganic Materials"
Langmuir, vol. 13, no. 14, pp 3896-3899, 1997

II.   Boris Zhmud, Anders Meurk and Lennart Bergström
"Evaluation of Surface Ionization Parameters from AFM Data"
Journal of Colloid and Interface Science, vol. 207, no. 2, pp 332-343, 1998

III.   Anders Meurk, Ian Larson and Lennart Bergström
"Tribological Properties of Iron Powder Subjected to Various Surface Treatments"
in *Fundamentals of Nanoindentation and Nanotribology*, ed. by N. R. Moody, W. W. Gerberich, S. P. Baker and N. Burnham, Mat. Res. Soc. Symp. Proc. vol 522, pp 427-432, Materials Research Society, Pittsburgh, PA, 1998

IV.   Goran Bogdanovic, Anders Meurk and Mark W. Rutland
"Tip Friction – Torsional Spring Constant Determination"
Colloids and Surfaces B, vol. 19, no. 4, 2000

V.   Anders Meurk
"Microscopic Stick-slip in Friction Force Microscopy"
Tribology Letters, vol. 8, no. 2-3, pp 161-169, 2000

VI.   Anders Meurk, Joseph Yanez and Lennart Bergström
"Silicon Nitride Granule Friction Measurements with an Atomic Force Microscope: Effect of Humidity and Binder Concentration"
Powder Technology, submitted

VII.   Eric Laarz, Anders Meurk, Joseph Yanez and Lennart Bergström
"Silicon nitride colloidal probe measurements: Interparticle forces and the role of surface-segment interactions in poly(acrylic acid) solutions"
manuscript in preparation

I am the sole contributor to the experimental work in all papers except Paper IV, where Goran Bogdanovic is an equal contributor and Paper II, where Boris Zhmud performed the computer modelling part. I am the main author of all papers except Paper II, where Boris Zhmud wrote the computer program and designed the manuscript, Paper IV, where Goran Bogdanovic and Mark Rutland are equally contributive, and Paper VII where Eric Laarz wrote a major part of the manuscript.

Papers listed below are not included in the thesis but are still relevant in the framework of AFM-studies with applications to advanced ceramic processing. When these papers are mentioned in the thesis they will be referred to by their respective Roman numeral.

VIII.   Lennart Bergström, Anders Meurk, Hans Arwin and David Rowcliffe
"Estimation of Hamaker Constants of Ceramic Materials from Optical Data Using Lifshitz Theory"
Journal of the American Ceramic Society, vol. 79, no. 2, pp. 339-348, 1996

IX.   Gavin Braithwaite, Paul Luckham, Anders Meurk and Kate Smith
"Probing Colloidal Interactions Using a Modified Atomic Force Microscope"
in *Modern Aspects of Colloidal Dispersions*, ed. by R. H Ottewill and A. R. Rennie, Kluwer Academic Publishers, Dordrecht, 1998, pp. 101-112.

X.   Boris Zhmud, Anders Meurk and Lennart Bergström
"Application of Charge Regulation Model for Evaluation of Surface Ionization Parameters from AFM Data"
Colloids and Surfaces A, vol. 164, pp 3-7, 2000.

XI.   Ken Darcovich, Floyd Toll and Anders Meurk
"Sintering Effects on the Porous Characteristics of Functionally Gradient Ceramic Membrane Structures"
Journal of Porous Materials, submitted

In the above four papers I have, to a varying degree, performed experimental work and contributed to writing the manuscript.

SUMMARY OF PAPERS

The papers can be grouped into *surface force measurements* and *friction force measurements,* although cross-fertilisation occurs. This summary presents the papers in a format, which does not necessarily coincide with their chronologically given Roman numerals.

The first work in this thesis, **Paper I**, concerns direct surface force measurements between inorganic materials in organic media, where the interactions were limited to a van der Waals force only. Here the main objective was to unequivocally measure a repulsive van der Waals force. A thorough theoretical analysis of the material dependent part of the van der Waals interaction, the *Hamaker constant*, was performed for a selection of ceramic materials (a project actually starting with **Paper VIII**). The electrodynamic origin of the van der Waals force gives either rise to an attractive or a repulsive force, depending on the correlation between the fluctuating dipoles of surfaces and the medium. Based on Lifshitz theory, we used frequency-dependent dielectric spectra for silicon nitride, silica, 1-bromonaphtalene and diiodomethane to design systems with a repulsive van der Waals force. An atomic force microscope was subsequently used for measurement of the interaction between a pyramidal silicon nitride tip, modelled as having a spherical cap, and a flat substrate of either silica or silicon nitride. The experimental force curves resulted in attraction in both media for the symmetric systems and repulsion for the asymmetric systems. This agreed well with the theoretical predictions. **Paper IX** treats similar force measurements. Note that the presence of a repulsive van der Waals force might decrease the loss of resolution due to tip deformation in AFM imaging, if the tip material and medium are chosen properly. There is also a large potential in optimisation of filtration processes or adhesion/friction reduction in various practical applications.

In **Paper II**, we presented a novel procedure for theoretical modelling of experimental AFM force curves using DLVO-theory in order to extract surface ionisation parameters. Silicon nitride and silica surfaces were chosen as interacting materials, based on the relatively well-known surface chemistry of these materials. Altering the composition of a silicon nitride surface from silanol-rich to silylamine-rich by etching procedures shifts the isoelectric point from low to high pH. This strongly influenced the interaction forces measured with AFM. A robust computer program was designed for numerical fitting of the experimental data. Here, the electrostatic interaction was calculated according to the non-linearised Poisson-Boltzmann equation including charge regulation relevant for the interacting surfaces. The good fit of experimental and modelled data served for analysis of several important compositional features. In addition to surface charge and surface potential, the density of surface groups was obtained as a function of pH. Charged surface species of opposite sign coexist in comparable amounts over a wide pH range for silicon nitride. As the surface inherently oxidises, silanol group density increases, thereby dominating the interaction forces. Since actual amounts of surface group densities have been obtained, there are some interesting applications. First, the technique can be used as a complementary technique to pH-potentiometric titration evaluation of net surface charge densities. Second, the results can be used for simulation of force profiles and colloidal stability.

Paper III presents a calibration procedure for quantitative friction force measurements with the atomic force microscope. Our ambition was to establish a relationship between cantilever torsional bending and friction force. The detector was calibrated by diverting the laser at known angles while continuously monitoring the detector voltage. Friction forces were then calculated in a straightforward manner from friction loops. The derived constant relating lateral voltage to probe angle were also used to show how much plastic deformation or energy loss occurred during static friction. The method was tested using friction measurements between a colloidal iron probe and a flat iron substrate. It was shown that when the surfaces had adsorbed layers of commercial lubricants, the friction force was reduced. Evaluation of the contact stiffness, *i.e.* the static friction slope, showed a large hysteresis between loading and unloading curves. This was attributed to substantial surface deformation. Combining our calibration procedure with traditional evaluation of static friction slopes rendered evaluation of the validity of contact mechanics theories possible for this system.

The subject of **Paper IV** recurs to AFM lateral force calibration. This paper describes a novel technique for experimental determination of torsional spring constants for any cantilever, regardless of shape, material or coating. Our approach was based on experimental lateral and normal force curves in conjunction with a sound theory of mechanics of materials. We modified the substrate in a way that the cantilever to be calibrated was slightly bending torsionally during a normal force curve. The lateral force curve deflection data was used for evaluation of the torsional spring constant. Three tipless cantilevers of different lengths were tested and compared to calculations from cantilever dimensions and materials properties. As the calculated values rely on cantilever thickness, which is cubed in the calculation, a small error in thickness determination can yield a substantially erroneous spring constant. This explains the significant discrepancy between our measured and calculated torsional spring constants; depending on the cantilever length, they differed by a factor of 3 to 4. Substantial effort was invested in calibration of the detector, scanner and cantilever, thereby limiting the errors involved in the obtained torsional spring constants to less than 15%. This error is only slightly higher than calibration methods for the normal spring constant.

Paper V investigates the nanorheological properties during sliding friction as a function of velocity and applied load of 12-hydroxy stearic acid (12-HSA) and 2-hydroxy stearic acid (2-HSA) coated silica surfaces. The measurements showed that even lubricated surfaces can give rise to stick-slip motion, a phenomenon industrially associated with wear and high costs. Friction-load measurements for 2-HSA coated surfaces showed a large hysteresis between loading and unloading curves, which was ascribed to energy dissipation due to molecular relaxation. The inital motion also displayed viscoelastic behaviour with a yield point as the static-dynamic friction transition. Steady sliding motion was replaced by highly regular stick-slip at a critical load for low velocities. The stick-slip motion was successfully described and fitted to a phenomenological model. The 12-HSA coated surfaces did not show a yield point during initial sliding and exhibited steady sliding over the entire load and velocity regime studied. Evaluation of the contact area from Maugis-Dugdale theory revealed the contact diameter to be very close to the stick-slip periodicity seen for the 2-HSA case. Thus, the entire contact zone was prone to microscopic stick-slip.

In **Paper VI** the AFM was used for direct measurement of friction forces between individual spray-dried granules and substrates as a function of relative humidity, binder concentration and sliding velocity relevant to powder pressing. One set of experiments was performed between two single ceramic granules, related to internal friction in pressing operations. In another set of experiments, friction forces were measured between a granule and a hard metal substrate. Granule-substrate measurements proved the friction coefficient to decrease with increasing humidity within a specific binder concentration, the effect being more pronounced for low concentrations. The friction coefficient also decreased with increasing binder concentration. The non-linear friction data was evaluated with a simple model that applies to boundary lubrication. This model gives the limiting coefficient of friction and the adhesion force. The coefficient of friction exhibited a strong variation with load due to a strong shear strength and contact pressure dependence. Evaluation of the adhesion force showed a steady increase with both humidity and binder concentration. A substantial difference in the adhesion force, almost an order of magnitude, was seen for the highest binder concentration between low and high humidities. These findings have been attributed to the hygroscopic nature of the binder, poly(ethylene) glycol (PEG). Softening of the PEG at increasing humidities lowers the friction coefficient but increases the adhesion force. The results were consistent with measurements of flowability and angle of repose.

Paper VII presents silicon nitride colloidal probe measurements in polyelectrolyte solutions. Silica spheres were nitrided in ammonia at high temperatures in order to produce a silicon nitride probe. ESCA measurements showed that the surface composition of the probes is representative of commercial silicon nitride powders. Surface force measurements against a silicon nitride wafer at different pH in simple electrolytes conformed to DLVO-theory, using a Hamaker constant and surface potentials typical for silicon nitride. Adsorption of poly(acrylic acid) above the isoelectric point of the surfaces generated a thin polymer layer at the surface. Although the adsorbed amount increased at higher ionic strength, the layer conformation remained flat. Adding small amounts of Y^{3+}-ions to the PAA solution induced comlexation in solution and promoted adsorption, albeit the layer thickness did not exceed 3 nm. The results indicate that PAA adsorbs on silicon nitride by specific surface–segment interactions different from those observed for zirconia or titania.

CONTENTS

Abstract
Preface
List of papers
Summary of papers

Acknowledgements

1. INTRODUCTION TO CERAMIC POWDER PROCESSING

Most people have probably produced a piece of ceramic in primary school using clay and water, relying on hand moulding techniques developed by our ancestors millennia ago. Why this processing method is not satisfactory for space shuttle thermal insulating shields, withstanding incineration during re-entry from space to the atmosphere, is obvious, but also indicates the progress achieved in the field of *advanced ceramics processing*. Advanced ceramics exhibit superior mechanical, or other specific, properties in a wide range of temperatures and environments. Their unique ionic and/or covalent bonding characteristics serves as the basis for use as technically structural and functional materials. Most advanced ceramics are composed of oxides, nitrides, carbides or borides and are tailor-made for optimal design, targeting industrial applications.

Ceramics are intrinsically brittle materials with minimum ability of deforming plastically.[1,2] At a certain degree of local stress build-up around defects within the body, catastrophic failure occurs. There are no ductile processes, such as yielding, to divert the stress. The strength and reliability of a ceramic is thus strongly dependent on the defect size and distribution. Once created, it is very difficult to remove large defects from a ceramic body. Powder impurities and agglomerates introduced in the first processing step eventually lead to formation of cracks or pores persistent during sintering, regardless of which shaping technique is used. A consequence of this is a low reproducibility in manufacturing due to the unique, defect dependent properties of each component, which may lead to rejection in subsequent failure tests. Probability analysis becomes useful in understanding flaw dependence on performance. One way of improving strength is to decrease the maximum defect size and reduce the size variation, another is to increase the fracture toughness via microstructure control. However, avoiding the presence of defects during powder synthesis is overall the primary goal.

Processing of advanced ceramics involves essentially four steps: (1) powder manufacture, (2) powder preparation for consolidation, (3) consolidation of the powder into a green compact of close-to-desired shape, and (4) firing. The final sintering step eliminates pores and provide densification. Additional steps include surface machining to the final shape. This is a potentially detrimental operation, especially for complex-shaped objects, stimulating development of novel processing techniques resulting in near-net shaped compacts.[3]

The starting powder is usually in the colloidal size range, 50-5000 nm. The powder is delivered or manufactured in an agglomerated state and must be prepared and adjusted to suit the subsequent consolidation process. Particle purity is of obvious concern for stoichiometry, sintering rate and defect minimisation. The finer the particle size, the larger the driving force during sintering; an order of magnitude reduction in size can lower the necessary sintering temperature by 200 degrees.[4] Unfortunately, powder handling becomes more difficult the smaller the size. Control of size and size distribution is achieved through milling, which is basically a deagglomeration process. Additional effects of milling include a gain in specific surface area (enhancing sintering) and surface chemical reactions (altering the isoelectric point). Particle size distribution and morphology heterogeneity are important factors in obtaining the desired microstructure, especially if a powder is randomly mixed with other powders.

Contamination of the powder may also introduce potential flaws after the desired properties have been attained. In full-scale industry, cigarette ash or the odd rat hair can be truly catastrophic to the final ceramic component.

1.1 Colloidal suspension consolidation

An effective method of minimisation of large flaws involves dispersing the powder in a suitable liquid where the interparticle forces can be controlled.[5] In these colloidal suspensions, manipulation and control of interparticle forces not only facilitates removal of hard agglomerates but also provides a means of forming a particle network of the desired strength. The ubiquitous van der Waals force acts to agglomerate the suspension, making it disordered and flocculated. Introduction of a repulsive force by controlling salt or polymer concentrations effectively stabilises and orders a suspension of monodisperse particles. Additional advantages of repulsive forces are the tendency to break up weak agglomerates and facilitate mixing of the powders.

The total interparticle potential is strongly linked to the suspension microstructure and the rheological properties. If gravitational forces are negligible, the suspension structure is mainly controlled by Brownian motion, interparticle forces and the particle volume fraction.[6] Optimisation of suspension rheology is important for ideal slurry flow behaviour during consolidation. Deliberate flocculation by sedimentation or centrifugation is sometimes required for removal of hard agglomerates. The dispersed state is then regained by applying a high-shear field to the system.
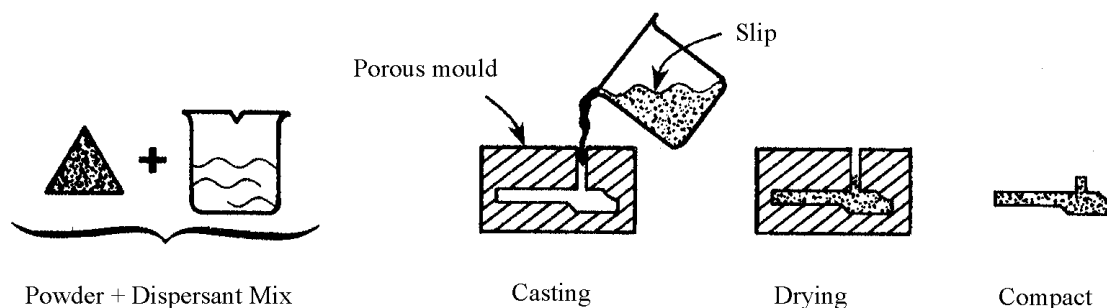

Fig. 1.1 Slip casting process for the manufacture of a ceramic component. From German[7].

Consolidation from slurry may be performed directly from the wet state by various techniques such as injection moulding, slip casting or tape casting. A simplified view of the slip casting process is shown in Fig. (1.1). Complex structures can be formed with minimal machining after sintering. Injection moulding is a process where a powder-binder mix is heated until softened, forced into a mould and resolidified to the desired shape. In slip casting the liquid penetrates the mould walls, leaving a cast layer of desired shape and thickness. The technique can be time-consuming and, is to a large extent, dependent on additive agents, such as binders and dispersants. Tape casting is favourable for production of thin, large, sheets aimed for the electronics industry. High particle volume fraction and low viscosity is required for handling purposes. Cracking and curling may be prevented by a narrow powder size distribution, and addition of a substantial amount of binder (up to 30 vol%). Drying of tape cast sheets is

facilitated if organic, volatile liquids are used. This emphasises the importance of suspension microstructure control via interparticle forces.

Fine powders, of submicron size, do not have free flowing properties due to spontaneous agglomeration. The van der Waals force has a stronger impact than inertial effects, leading to poor flow, clogging of feeding systems and variations in powder density. Deliberate formation of large agglomerates (granules) is achieved by spray-drying a colloidal suspension (Fig. 1.2). The free-flowing granules generally exhibit better flow, die feeding and lubricating characteristics than fine powders. The spray-drying process consists of pumping slurry through a nozzle into hot air. Granule formation occurs in several steps: (1) atomisation of the slurry to droplets, (2) drying of the droplets, and (3) separation of granules from the air. During drying the droplets shrink until the critical point is reached, where particles come into contact and the shrinkage stops.[8] Granules are usually 50-1000 μm and of spherical shape, but their properties are strongly related to additives in the slurry. Granule density, strength and deformability are thus direct consequences of the slurry properties and the spray-drying process. High binder content and high temperatures in the spray-drier result in hollow granules with a large crater on the surface where the liquid escaped during evaporation. Such granules produce low-density compacts due to low packing density.

The strength of a granule should be sufficient to survive handling and feeding to the mould. During the later pressing operation the granules break and the particles slide against each other. Any granules that have remained intact throughout compaction may constitute a fracture origin. Hence, the granulation step determines to a large extent the final compact microstructure and mechanical strength.
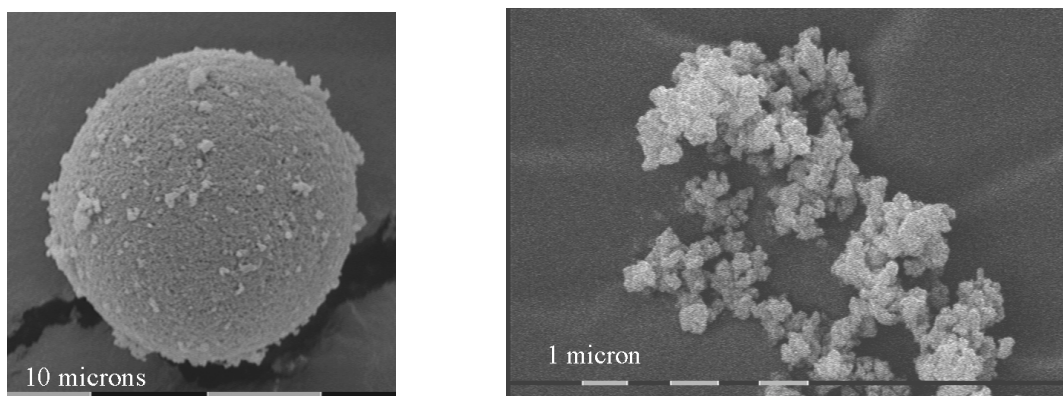

Fig. 1.2 The difference between a silicon nitride based SiAlON granule (left) and the original silicon nitride powder (right).

1.2 Dry powder compaction

One of the most common forming techniques is dry pressing, in which powders are consolidated in a cavity and subjected to an applied pressure in an uniaxial direction.[9] Uniaxial pressing of granules aims at producing a green body of high density and sufficient strength to survive further processing steps. Initially, the applied pressure rearranges the granules in the die. At a certain pressure, the density increases rapidly; this transition is commonly identified as the apparent yield point of the powder body. There is a correlation between the apparent yield point and the mechanical properties of the granules.

The density gradients of a pressed body are related to the pressure distribution during compaction. Friction lowers the effectiveness of compaction and affects the final density distribution within the compact. Friction between die walls and granules, as well as between the individual granules, sets in when the porosity decreases and particles interlock. Optimisation of binder, sintering aids, lubricants and grain growth inhibitors is a means of reducing friction and adhesion. Binders are sensitive to changes in humidity owing to their hygroscopic nature. Changes in binder deformation properties (*e.g.* the shear modulus) therefore affect the entire granule performance; low humidity leads to hard granules prone to fracture, whereas high humidity softens the binder-rich granule surface, promoting deformation.[10]

The dominate manufacturing process of metal powders is uniaxial compaction at very high pressures (Fig. 1.3).[7] Minimal wall friction may be obtained by lubrication with additives, usually based on stearic acid. Common lubricants include zinc stearates or other metal organic compounds. The polar character of the head groups aids in the attachment to the powder surface. The lubricant addition must be minimised because high lubricant concentrations occupy volume between the particles and leads to low green densities. Hence, optimisation of the amount of lubricant is necessary in order to achieve a balance between low friction and low lubricant content.
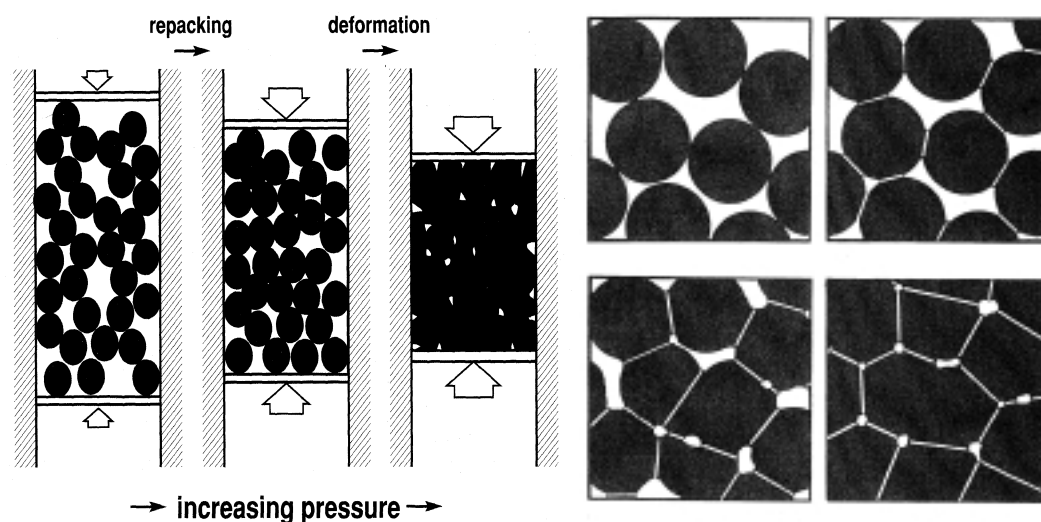

Fig. 1.3 A simplified view of uniaxial compaction process (left) and pore volume shrinkage during sintering (right). From German[7] and Schneider[9].

1.3 SPM in a powder processing context

The emergence of Scanning Probe Microscopy as an imaging instrument has revolutionised many scientific disciplines.[11-13] For the first time, surface topography could be measured in seconds without the need of vacuum or a conductive layer. Surface degradation studies as a function of time under ambient or specific conditions has proven useful in many fields, *e.g.* biochemistry, materials science, paper technology and geochemistry. The versatility of the instrument was further increased due to the development of imaging modes capable of resolving differences in surface elasticity and hardness.

Imaging of pressed components is the obvious choice for the use of SPM in ceramic processing. However, the versatility becomes apparent in surface force and friction force measurements where basically any sufficiently hard material can act as a probe. Well-defined probe geometry allows for a quantitative analysis of the interacting forces.

This thesis focuses on the use of SPM in two related areas relevant to processing of ceramic and metal powders:

(1)   Surface force measurements as a means of evaluating and characterising the colloidal stability of silicon nitride in aqueous suspensions.

SPM measurement of interparticle forces between ceramic materials in aqueous solutions is a direct method for understanding and improving the stability of a colloidal suspension.

(2)   Measurements of powder and granule wall friction during the initial stage of a dry powder pressing operation.

SPM friction measurements between individual ceramic granules and between the die-wall material and a granule is a direct method of comparing and evaluating flowability and pressing behaviour of industrially important ceramic materials.[14] Effects of die-wall lubrication can also be studied by coating the wall material. Metal powders, ungranulated, can be coated with binders and then friction can be measured against a coated or uncoated die-wall substrate. The possibility of determining the influence of particle roughness, adhesion, interaction forces, humidity etc. in friction force measurements truly demonstrates the applicability and versatility of the instrument.

The SPM was not invented for quantitative determination of forces on the nanoscale. Parts of this thesis are therefore concerned with calibration methods for signal conversion to useful measures. Finally a note on terminology: I have chosen to use the abbreviation SPM throughout this thesis because "probe" is more relevant to my work than "atomic".

2. SURFACE FORCES

Below is an overview of surface forces relevant to processing of ceramic materials.

2.1 van der Waals interaction

The van der Waals force is a long-ranged force acting between any surfaces in any media. The force has an electrodynamic origin based on interactions between permanent and induced dipoles. Depending on the orientation of atomic and molecular electric dipoles, their correlations give rise to attraction or repulsion. Three types of interaction add up to the total van der Waals force:[15]

(i)   The *Keesom* or *orientation* interaction is a dipole-dipole interaction, where the electric field created by a permanent dipole affects other permanent dipoles.
(ii)   The *Debye* or *induction* interaction is a dipole-induced dipole interaction, where the field from a permanent dipole induces a dipole in a polarisable atom or molecule, so that the induced dipole interacts with the permanent dipole.
(iii)   The *London* or *dispersion* interaction, occurs when an induced dipole, created by fluctuation of electronic charges, induces dipoles in other molecules.

The Hamaker approach

The van der Waals interaction energy for two macroscopic spheres of equal size, *R*, separated by distance *D*, is

$$V_A(D) = -\frac{A}{6}\left[\frac{2R^2}{D^2 - 4R^2} + \frac{2R^2}{D^2} + \ln\left(\frac{D^2 - 4R^2}{D^2}\right)\right] \qquad (2.1)$$

where *A* is the Hamaker constant. This constant is a material property and was introduced by Hamaker when calculating dispersion forces by adding up mutual pairwise interactions.[16] The earliest expression for interactions between two materials was expressed in terms of number densities, ρ_i, and a constant *C*, so that the Hamaker constant became

$$A = \pi^2 C \rho_1 \rho_2 \qquad (2.2)$$

Eq. (2.2) above is only valid for like materials in a vacuum, because the constant *C* is roughly proportional to the volume of an atom, which makes *A* roughly constant whatever medium separates the interacting bodies.

The theoretical microscopic approach presented by Hamaker is unfortunately subject to a few limitations. The calculations are based on number densities and polarisabilities of the atoms of the interacting bodies, and ignore the effect of the surrounding medium.[17] Apart from this many-body effect, there is also the effect of retardation, which is ignored in Hamaker's theory. Retardation occurs when the distance between the interacting bodies is so large that the propagation of the electromagnetic field can not be regarded as instantaneous. The electromagnetic field created by electron and nuclear motion of a molecule propagates into the surrounding space at the speed of light. If the distance is large enough, the first molecule

has altered its dipole orientation by the time the reflected field from the interacting molecule has returned. This results in a weaker dipole moment and subsequently weaker attraction, and a more rapid decrease with separation distance. The separation distance at which the effect of retardation becomes noticeable depends on the characteristic wavelength of internal molecular motion, λ_0, and is typically on the order of 10 nm.

Lifshitz theory

Lifshitz[18] presented an alternative approach to calculate A where each body is treated as a continuum with certain dielectric properties, which ingenuously incorporates many-body effects and retardation. However, Lifshitz theory is only valid when the interacting surfaces are farther apart than molecular dimensions and the media are homogeneous with constant densities. From Lifshitz theory, the interaction energy per unit area between two half-spaces, composed of materials 1 and 2, separated by thickness D of material 3, is

$$V_{132}(D) = -\frac{A_{132}(D)}{12\pi D^2} \tag{2.3}$$

where the Hamaker constant A_{132} is given by

$$A_{132} = -\frac{3}{2}kT\sum_{n=0}^{\infty}{}'\int_{r_n}^{\infty} x\left\{\ln\left[1 - \Delta_{13}\Delta_{23}e^{-x}\right] + \ln\left[1 - \overline{\Delta}_{13}\overline{\Delta}_{23}e^{-x}\right]\right\}dx \tag{2.4}$$

where

$$\Delta_{jk} = \frac{\varepsilon_j s_k - \varepsilon_k s_j}{\varepsilon_j s_k + \varepsilon_k s_j} \qquad\qquad \overline{\Delta}_{jk} = \frac{s_k - s_j}{s_k + s_j}$$

$$s_k^2 = x^2 + \left(\frac{2\xi_n D}{c}\right)^2(\varepsilon_k - \varepsilon_3) \qquad\qquad r_n = \frac{2D\xi_n\sqrt{\varepsilon_3}}{c}$$

$$\xi_n = \frac{2\pi nkT}{h} \qquad\qquad\qquad \varepsilon_k = \varepsilon_k(i\xi_n) \tag{2.5a-f}$$

and k is Boltzmann's constant, T temperature, h Planck's constant, $\varepsilon_k(i\xi_n)$ the frequency dependent dielectric response function of medium n and c is the speed of light in a vacuum. The prime on the summation term indicates the $n = 0$ term (the zero-frequency, static contribution) should be given half weight.

As $D \to 0$ the Hamaker constant will not be subjected to retardation and Eq. (2.4) may be expanded and integrated. For two half-spaces of material 1 and 2 interacting over medium 3, the non-retarded Hamaker constant is finally written as[19]

$$A_{132} = \frac{3kT}{2} \sum_{m=0}^{\infty} {}' \sum_{s=1}^{\infty} \frac{(\Delta_{13}\Delta_{23})^s}{s^3} \tag{2.6}$$

where

$$\Delta_{kl} = \frac{\varepsilon_k(i\xi_m) - \varepsilon_l(i\xi_m)}{\varepsilon_k(i\xi_m) + \varepsilon_l(i\xi_m)} \tag{2.7}$$

where $\varepsilon_k(i\xi_m)$ and $\varepsilon_l(i\xi_m)$ are the dielectric response functions of material k and l, respectively, evaluated at the imaginary frequency, $i\xi_m$ with

$$\xi_m = m(4\pi^2 kT / h) \tag{2.8}$$

A few interesting points can be deduced from Eq. (2.4-2.8):

- The dominant van der Waals interaction stems from the dispersion force for most materials. However, there can be a significant contribution from the static part for highly polar materials.

- The static contribution is the only temperature dependent part of the van der Waals interaction (provided that any temperature dependence of the dielectric response function is negligible).

- The van der Waals *force*, the derivative of Eq. (2.3) with respect to distance, is always attractive regardless of the intervening medium for two like materials.

- The van der Waals force between two different or similar materials in air (vacuum) is always attractive.

- The van der Waals force between two dissimilar materials across a dielectric medium can be either attractive or repulsive. The requirement for repulsion is that the dielectric properties of the medium must be intermediate of those of the materials, *i.e.* $\varepsilon_1(i\xi) < \varepsilon_3(i\xi) < \varepsilon_2(i\xi)$. Repulsion can also occur in special cases due to retardation, where the force is attractive at small distances but repulsive at larger distances (the static part overcomes the dispersive part).

In order to evaluate the function $\varepsilon(i\xi_m)$, the dielectric response of the material over the entire frequency range must be known. Due to insufficient dielectric data, many researchers restrain from using Lifshitz theory and commonly resort to simple, order-of-magnitude, approximations. However, Parsegian and co-workers have shown that partial knowledge of the dielectric response function is sufficient to estimate the Hamaker constant for many materials using Lifshitz theory.[20-22] They conveniently expressed the imaginary dielectric response function with an oscillator model

$$\varepsilon(i\xi) = 1 + \sum_{j=1}^{N} \frac{C_j}{1 + (\xi / \omega_j)^2} \qquad\qquad C_j = \frac{2f_j}{\pi\omega_j} \tag{2.9a-b}$$

where f_j is the oscillator strength and ω_j the relaxation frequency (in rad/s). This representation simplifies the construction of the required function $\varepsilon(i\xi_m)$. Frequencies are sampled at equally spaced intervals with most of them lying in the UV part of the spectrum at room temperature. At higher imaginary frequencies the dielectric response function drops to unity and does not contribute to the interaction between non-metallic materials. The importance of water in many colloidal systems has recently led to very detailed knowledge of spectral parameters in the ultraviolet, infrared as well as the microwave range. However, it has been shown that most materials with simpler spectra can be well described by one UV and one IR relaxation, since this range of the absorption spectra is the most important for the dispersion interaction.[15]

Paper VIII illustrates how ellipsometry measurements and "Cauchy plots" can provide accurate spectral parameters from refractive index data. A typical Cauchy plot for amorphous (α) and polycrystalline (β) silicon nitride is shown in Fig. (2.1). Comparison of several approximations and novel calculations of Hamaker constants for inorganic materials has recently been performed by Bergström.[23]
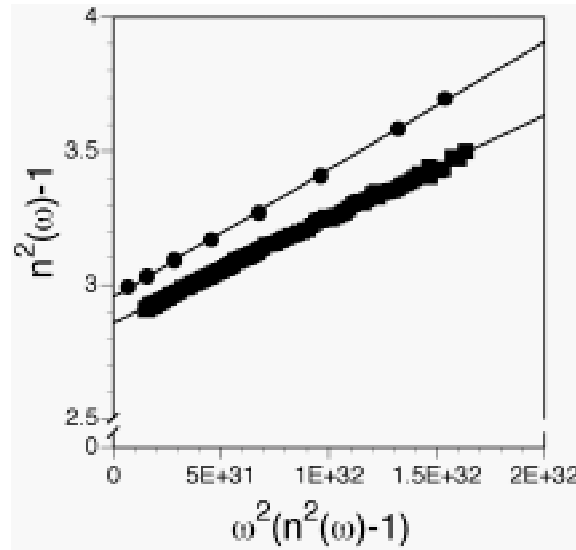

Fig. 2.1 Cauchy plot for noncrystalline (**J**) and polycrystalline (**B**) silicon nitride. The nonretarded Hamaker constant across air for noncrystalline and polycrystalline silicon nitride is 167 zJ and 180 zJ, respectively, and across water 54.7 zJ and 48.5 zJ, respectively.

2.2 Electrostatic double-layer forces

Numerous everyday phenomena are governed by electrostatic coulombic interactions between charged surfaces in both air and water. When the interacting medium is not restricted to vacuum, dry gas or a non-polar solvent but rather a liquid of high dielectric constant, charges will usually occur on the immersed surfaces. The acquiring of charges is predominantly determined by adsorption of ions from solution or dissociation of surface species.[24] Another important charging mechanism of great importance to semiconductor technology is crystal lattice defects.

The surface charges are balanced by oppositely charged counterions in the solution. Counterions bound to the surface form the *Stern layer*, while the remaining counterions form a cloud in rapid thermal motion extending out from the surface. This vaguely defined region is known as the electric double layer (Fig. 2.2).

The counterion density decays exponentially with distance from the surface, described by the Boltzmann distribution

$$\rho = \rho_0 e^{-ze\psi/kT} \tag{2.10}$$

where ρ is the number density of ions of valency z, ρ_0 is the ionic concentration in the bulk and ψ the electrostatic potential. Combining Eq. (2.10) with Poisson's equation for the net excess charge at a certain position x from the surface, gives a relationship between ion thermal diffusion and electric effects. The non-linear *Poisson-Boltzmann (PB) equation* becomes

$$\frac{d^2\Psi}{dx^2} = -\frac{e}{\varepsilon\varepsilon_0}\sum_i \rho_{0,i} z_i \exp\left(\frac{-z_i e\Psi_x}{kT}\right) \tag{2.11}$$

where Ψ_x is the potential at distance x and all other symbols have their conventional meaning. Solving non-linear second order differential equations requires initial boundary conditions. In this case, they are given by electroneutrality between surface and solution and the fact that the electric field is zero at the midplane.

Eq. (2.11) forms the basis of the *Guoy-Chapman (GC) theory* where the right hand part is equal to a sinusoidal hyperbolic function of the surface potential for a flat interface and a symmetrical 1:1 electrolyte. Linearisation of the sinh-function leads to the *Debye-Hückel (DH) approximation*[25]

$$\nabla^2\psi = \frac{d^2\psi}{dx^2} = \left(\frac{\sum z_i^2 e^2 c_0}{\varepsilon_0\varepsilon_r kT}\right)\psi = \kappa^2\psi \tag{2.12}$$

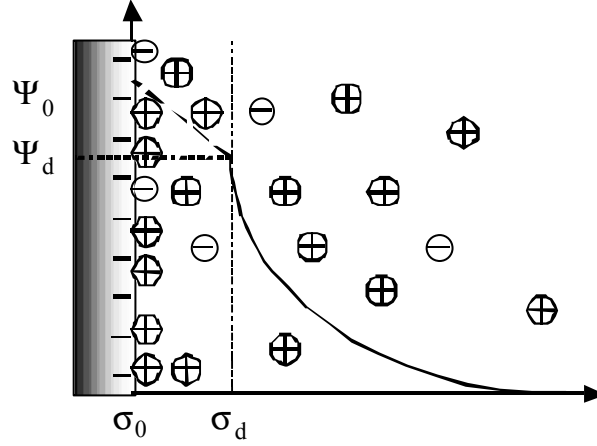where $1/\kappa$ is the *Debye screening length*, and κ is given by

Fig. 2.2 Model of the interface between a charged surface and an aqueous solution. Loosely bound charges exchange with ions in solution, forming the electric double layer. Ψ denotes potential and σ surface charge density.

$$\kappa = \frac{\left(\sum_i \rho_{0,i} e^2 z_i^2 \right)^{1/2}}{\varepsilon \varepsilon_0 kT} \qquad (2.13)$$

The Debye length is an approximate value of the double layer thickness and describes the decay length of the interaction between two surfaces. It is only dependent on the bulk ion concentration, apart from fundamental constants. For a 1:1 electrolyte at 298 K in water, its value is roughly equal to $0.304/\sqrt{\rho_0}$ nm if the ionic concentration is given in mol/l. The Decay length decreases with electrolyte asymmetry, particularly for high valencies. Estimation of Debye lengths for systems with mixed symmetric and asymmetric electrolytes requires substantially complicated computations.[26]

When two surfaces with identical double layers are in close proximity to each other, an increase in counterion concentration between the surfaces compared to the bulk solution gives rise to an osmotic pressure, *P(D)*, given by

$$P(D) = kT \left[\rho(D) - \rho(\infty) \right] \qquad (2.14)$$

where $\rho(D)$ is the concentration of ions at the surfaces. The electric double layer interaction energy is obtained by calculating the work required for bringing the surfaces together from infinite separation. The force is subsequently obtained from the Derjaguin approximation (see below).

Charge regulation

The DH approximation is valid for symmetrical electrolytes, low ionic concentrations and as long as the surface potential does not exceed the thermal energy ($\approx$25 mV at room temperature). Calculated results using the non-linear PB equation suggest that the DH approximation holds for potentials up to 45 mV.[27] Solutions to the Guoy-Chapman model

assume that one or both surfaces maintain constant charge or constant potential during the interaction. If the surface charge arises from irreversible adsorption of charged species or dissociation of strong surface groups, the surface charge density becomes independent of the surface potential and consequently of the separation of the surfaces. The assumption of constant charge may be valid at rapid approach since there is not sufficient time for the potential-determining ions to desorb.[24] On the other hand, if the adsorption-desorption thermodynamic equilibrium is established immediately at every configuration of the interacting particles, the surface potential is independent of the separation and the constant surface potential boundary condition is applicable.[28] The surface potentials should therefore remain constant for two surfaces during interaction when approaching at slow speed. This requires a gradual discharge, eventually leaving no charges on, or between, the surfaces. Surfaces with lattice imperfections are supposed to have constant charge, whereas constant potential is valid for surfaces adsorbing ions.

In reality, the surface charge density of ionisable surfaces is a function of separation when the distance approaches zero. Constant charge constitutes the upper energy limit for the interaction, whereas constant potential constitutes the lower limit. A realistic description of the interaction falls in-between these limits and is known as *charge regulation*[29,30]. Considering the chemical equilibria that are responsible for the development of charges at a dissociated surface, it is seen that the charge density, which determines the potential distribution in the diffuse layer itself, is a function of the surface potential. The thermodynamic background of charge regulation has been treated by Zhmud and Bergström,[31] much in the same way as Reiner and Radke.[32] When a solid is set in contact with a liquid solution, the solvent molecules reorient themselves in the potential field of the solid surface until, after some finite time, adsorption or surface hydroxylation has reached equilibrium. The affinities of ions can be expressed in terms of their chemical potentials and intrinsic equilibrium constants in a mass balance.

An amphoteric surface with ionisable sites (surface species) of the form *AH*, where *A* represents an element such as Si, in a 1:1 electrolyte solution at a certain pH can become positively or negatively charged by gaining or losing hydrogen ions.[33] It can be characterised by the reactions

$$AH_2^+ \leftrightarrow AH + H^+ \qquad (K_+) \qquad\qquad (2.15)$$
$$AH \leftrightarrow A^- + H^+ \qquad (K_-) \qquad\qquad (2.16)$$
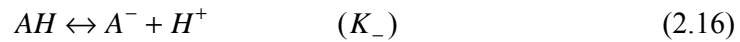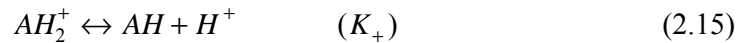
where K_+ and K_- are the corresponding dissociation constants. At equilibrium

$$K_+ = \frac{[AH][H^+]_s}{[AH_2^+]} \quad \text{and} \quad K_- = \frac{[A^-][H^+]_s}{[AH]} \qquad (2.17\text{-}18)$$

For metal oxides, the potential determining ions are H^+ and OH^- and the surface hydrogen ions can further be related to the pH of the bulk electrolyte, $[H^+]_b$, via

$$[H^+]_s = [H^+]_b \exp(-e\psi_s/kT) \qquad\qquad (2.19)$$

where ψ_s is the surface potential. The total number of ionisable surface groups per area, N_s, and the net surface charge density, $\sigma_s(\psi_s)$, is given by[34]

$$N_s = [AH] + [AH_2^+] + [A^-] \qquad \text{and} \qquad \sigma_s = e[(AH_2^+) - (A^-)] \qquad \text{(2.20-21)}$$

Combining Eq. (2.17-2.21) gives the relationship between surface charge and surface potential

$$\sigma_s = eN_s \frac{\left([H^+]_b / K_+\right)\exp(-e\psi_s/kT) - \left(K_-/[H^+]_b\right)\exp(e\psi_s/kT)}{1 + \left([H^+]_b / K_+\right)\exp(-e\psi_s/kT) + \left(K_-/[H^+]_b\right)\exp(e\psi_s/kT)} \qquad \text{(2.22)}$$

which is usually written as

$$\sigma_s = eN_s \frac{\delta \sinh[e(\psi_N - \psi_s)/kT]}{1 + \delta \cosh[e(\psi_N - \psi_s)/kT]} \qquad \text{(2.23)}$$

with $\delta = 2[K_- / K_+]^{1/2}$ and the Nernst potential connected via the isoelectric point

$$\psi_N = \frac{kT}{e} 2.303 \left[\frac{1}{2}(pK_+ + pK_-) - pH\right] \qquad \text{(2.24)}$$

The dissociation constants above are assumed to be functions of temperature and pressure only, *i.e.* no cross-correlation with surface potentials.

Eq. (2.23) displays a non-linear relationship between charge and potential. Chan and Carnie[33] suggested a linearised charge regulation model given by

$$\sigma_0 = K_1 - K_2\psi_0 \qquad \text{(2.25)}$$

where the first constant has the same sign as the surface charge when the surfaces are in isolation. The second constant is referred to as the regulation capacity since it has the dimension of electrostatic capacitance. It is always positive, equals $(d\sigma_0/d\psi_0)_{isolated}$ and reflects the ability of the surface ionisation reactions to maintain constant surface charge. The limit $K_2=0$ corresponds to constant surface charge. The error in using this linearised model is expected to be larger at smaller separations since approximating regulation with a tangent line for the amphoteric charge-potential curve is most accurate in the neighbourhood of $\psi_{isolated}$.

Implementing the charge regulation procedure above requires full treatment of the physical-chemical balance of the electrostatic interaction in the form $\psi_s = f(\sigma_s)$. This function is given by the PB equation (Eq. 2.11), with the appropriate geometry and the boundary condition given by Eq. (2.22).

2.3 Other forces

Describing the *total* interaction between surfaces in solution is a difficult task. Many forces in specific systems are poorly understood with more or less empirical descriptions, particularly interactions in water. Of considerable debate is the question of why hydrophobic surfaces exhibit a long-range attractive force far stronger than the van der Waals force. Without going into detail, the unclear molecular origin has stimulated a variety of possible mechanisms:[35] bubble/cavity formation, electrostatic explanations and changes in water density. Hydrophilic surfaces in aqueous systems exhibit a monotonically decaying repulsive *hydration force*. This important interaction originates supposedly from hydrogen-bonding surface groups disrupting the hydrogen bond network of water.[15] Silica experiences rather long-ranged hydration forces because of hydroxyl surface groups. Counterions in solution affect both magnitude and decay length, a direct consequence of the difference in hydration radius.

Important effects arise when the separation distance becomes comparable to the size of the solvent molecule structure, where the charge distribution no longer satisfies the continuum theory-based PB-equation.[15] Counterion mobility within the double layer is responsible for the attractive *ion-correlation force* at separations below 4 nm.[15] This force increases with surface charge density and valency of the counterions. An additional repulsion appears as the separation distance approaches the size of the ions. Charges can no longer be regarded as points, building up an osmotic pressure in analogy to the excluded volume of a compressed van der Waals gas. As the distance between two surfaces decreases, their electron clouds will eventually overlap, leading to a strong, short-ranged Born repulsion.

Polymeric forces

An effective way of stabilising colloidal suspensions is to graft or adsorb polymer from solution to the particle surface. Grafting provides an efficient means to full coverage but this sometimes proves difficult to achieve. Israelachvili[15] describes the nature of the interactions between adsorbed polymer layers as dependent on the quality of the solvent and the degree of intra-chain versus inter-chain forces; in a good solvent there are no interactions between polymer chains, whereas in a poor solvent intersegment attraction results in collapse into compact coil structures. During confinement in a good solvent, the entropy change associated with chain compression leads to an osmotic, excluded-volume, repulsive *steric* force. Systems involving charged polymers (polyelectrolytes) give rise to *electrosteric interaction* in aqueous salt solutions, where the electrostatic double layer force affects the steric contribution to the total interaction.

2.4 DLVO-theory

The theory of colloidal stability by Derjaguin, Landau, Verwey and Overbeek is a cornerstone in colloid science, explaining the dispersed state of lyophobic particles, and is known as DLVO-theory. [25,36] It comprises the sum of the van der Waals force and the electrostatic double layer repulsion. All other forces are referred to as "non-DLVO"-forces and are not necessarily additive, although short-ranged ion effects tend to cancel each other out.[15]

Interesting effects can arise depending on electrolyte concentration and surface charge density. Low concentrations of salt or highly charged surfaces give rise to an energy barrier

often sufficient for stabilising suspensions. The emergence of a secondary minimum in the interaction energy curve at higher electrolyte concentrations enables particles to be trapped if the well is deep enough (Fig. 2.3). Particles trapped here may resist thermal motion and remain kinetically stable without touching. The particles coagulate above a certain electrolyte concentration, where the energy barrier disappears. Consequently, irreversible coagulation occurs, leading to rapid flocculation. Non-DLVO forces provide a means of preventing such conditions by re-introduction of a repulsive energy barrier.
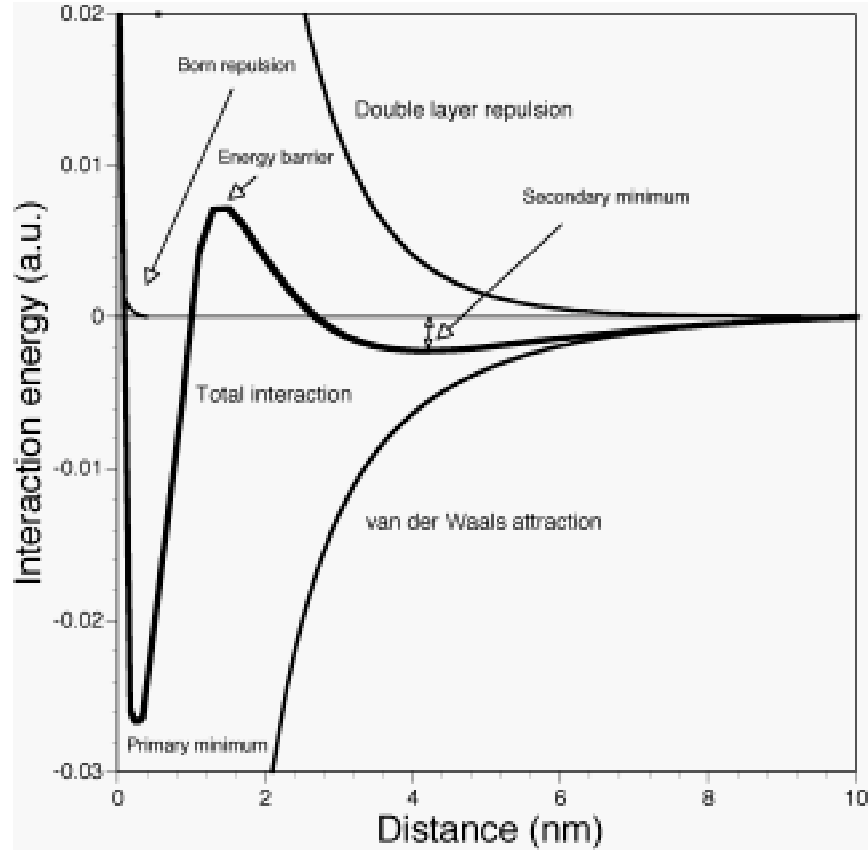

Fig. 2.3 Illustration of DLVO-theory in combination with Born repulsion. The presence of an energy barrier may give rise to a secondary minimum, apart from the primary minimum where the van der Waals force is exceeded by Born repulsion.

2.5 The Derjaguin approximation

Theoretical treatment of interactions between macroscopic bodies is generally given in terms of interaction energy per unit area for the simple case of two plane parallel half-spaces. It is of considerable interest to relate this energy to the actual force, or pressure, between surfaces of other geometry due to the limited number of force measurements using parallel planes. Derjaguin,[37] and later White,[38] derived expressions relating interaction energy to force as surfaces of a certain curvature approach. Thus, the interaction free energy per unit area, *W(D),* is

$$W(D) = \frac{F_{sp}(D)}{2\pi R} = \frac{F_{ss}(D)}{\pi\sqrt{R_1 R_2}} = \frac{F_{cc}(D)}{2\pi\sqrt{R_1 R_2}} \qquad (2.17)$$

where F_{ij} is the force between a sphere and a flat surface (index *sp*), two spheres (*ss*) and two crossed cylinders (*cc*), and R_1 and R_2 denote the radii of curvature of the interacting surfaces.

The Derjaguin approximation is valid for any type of interaction, provided that

- the curvature of the interacting bodies is large compared to the surface separation distance *D*
- the smallest radius of curvature of the system is larger than the length scale on which the interaction decays to zero.

Stancovich and Carnie state that the accuracy of the Derjaguin approximation improves with high surface potentials due to large gradients near the surface, smaller curvatures and large values of κR.[39] They calculated interactions between spheres and a sphere and a plate using computational procedures for the non-linear PB equation.

3. FRICTION AND ADHESION

3.1 Adhesion energy

The work of adhesion per unit area, W_{132}, is equivalent to the energy required to break contacting bonds. The associated creation of new bonds determines the total irreversible change in interfacial free energy, $\Delta\gamma$, given by the Dupré equation[24]

$$W_{132} = \Delta\gamma = \gamma_{13} + \gamma_{23} - \gamma_{12} \tag{3.1}$$

where index *1,2* and *3* refer to the two contacting materials and the medium, respectively. Considering the Derjaguin approximation for a disjoining pressure between two flat surfaces, the interaction energy per unit area equals the work of adhesion. The adhesion force, F_{ad}, between a sphere of radius R and a flat surface is given by

$$F_{ad} = 2\pi R W_{132} \tag{3.2}$$

This solution is a simplification since elastic or plastic deformation occurs as a consequence of the attractive force (or the externally applied load).

3.2 Friction laws

Early theories of friction dependence on applied load were based on plastic deformation of multiple asperities in contact.[40] The friction coefficient is traditionally given by the ratio between friction force, F_f, and applied load, L, and is independent of contact area and sliding velocity. However, many observations of a finite friction force at zero load and the strong dependence on contact area for adhering surfaces at low loads, have highlighted the significance of elastic deformation. This adhesion-controlled friction is similar to Amonton's law, but given by[41]

$$F_f = \mu(L_0 + L) = F_0 + \mu L \tag{3.3}$$

where L_0 is the additional load caused by attractive forces, F_0 the friction force due to adhesion and μ the friction coefficient. Note that the friction coefficient is here given by dF_f/dL at $F_f > F_0$.

The plastic junction model of Bowden and Tabor has been extended by Gee[42] and co-workers for surfaces separated by a thin liquid film. Contributions from internal adhesion across the film and the externally applied load are taken into account, giving

$$F_f = S_c A + CL \tag{3.4}$$

where S_c is the shear stress, defined as friction force per unit area A, and C is a constant related to surface shape and molecular configurations in the separating gap. The second term becomes less significant the smoother the contact but may have a pronounced effect at higher loads.

Surfaces which exhibit a boundary type friction behaviour are commonly described by an equation of the form[43,44]

$$F_f = k(L + L_a)^n \qquad (3.5)$$

where k is the friction factor and n the load index. The load index can vary between 2/3 and unity; the former corresponds to an elastic response in accordance with contact mechanics theory, while the latter is equivalent to a multiple asperity contact (Amonton's law). A constant friction coefficient can not strictly be defined from Eq. (3.5), because it is load dependent as long as $n < 1$. However, when the load index equals unity the pressure dependence of the shear strength is negligible, and the friction factor conforms to the friction coefficient. This condition is only met in a region where the influence of load on shear strength is negligible; hence, the friction coefficient must be evaluated at high applied loads.

Although Eq. (3.4) conveniently covers many parameters relevant to friction, there is still an unresolved issue concerning the relationship between adhesion and friction over the small length scales frequently encountered in nanotribological experiments. The work required for bringing two surfaces into contact is generally not equivalent to the work needed for separating them. This *adhesion hysteresis*[45] may be seen as a cycle of loading and unloading. Hence, the adhesion energy consists of a real term describing the energy stored and an imaginary term describing the energy dissipated during the process. The same amount of work can be done by sliding the surfaces laterally instead of vertically. Friction is a highly dissipative process where the loading-unloading cycle frequently displays hysteretic behaviour. The mechanism by which energy dissipates is less known, but is believed to be due to thermodynamically irreversible mechanical, thermal or chemical transitions.

Irreversible adhesion, or friction hysteresis, is a result of lower surface free energy during loading than on unloading, *i.e.* the receding energy is higher than the advancing ($\gamma_R > \gamma_A$). Close correlations exist with contact angle hysteresis and wetting/dewetting phenomena. In boundary lubrication the contact area in friction measurements is restricted to a thin film or adsorbed monolayer region. Under these conditions, the loading friction curves follow the advancing surface energy, whereas unloading curves are a direct consequence of the increased receding energy.[46] The difference between these energies gives rise to hysteresis, and it can be argued that friction is proportional to the adhesion hysteresis, and not the adhesion force.[46,47]
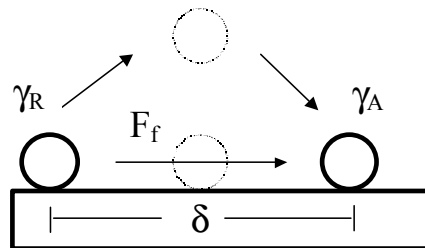

Fig. 3.1 Equilibrium relationship between sliding friction and adhesion hysteresis. Independently of path taken, $F_f \delta = A(\gamma_R - \gamma_A)$, where δ is a characteristic molecular length scale and A the contact area. Rearrangement recurs to Eq. (3.4) at low loads in the wearless regime. Adapted from Israelachvili et al[47].

3.3 Contact mechanics theory

In the absence of plastic deformation or dissipative viscoelastic relaxations, the size of the contact area depends on the elastic response of the materials and the interaction potential. Contact mechanics provide the link necessary for friction and adhesion hysteresis to be quantified with respect to materials properties (such as shear strength), encompassing the size of the actual contact area. Several theories have emerged from the pioneering work by Hertz a hundred years ago, where the adhesion between two smooth elastic bodies has been given increasing focus. Each theory has a well-established validity range and the appropriateness of each must be fully acknowledged when being applied to AFM measurements.

Below is a short description of the most frequently used theories. The geometrical set-up is a sphere of radius R against a flat surface, giving rise to the combined elastic modulus K, given by

$$\frac{1}{K} = \frac{3}{4}\left[\left(\frac{1-v_1^2}{E_1}\right)+\left(\frac{1-v_2^2}{E_2}\right)\right]$$

(3.6)

where v is Poisson's ratio and E Young's modulus of materials 1 and 2, respectively.

Hertz theory

Hertz theory assumes that neither adhesion nor surface forces act between the surfaces. The deformation is induced in the sphere by an externally applied force F. Assuming a circular contact area A with radius a, Hertz theory yields[40]

$$a = \left(\frac{RF}{K}\right)^{1/3} \qquad\qquad A = \pi\left(\frac{R}{K}\right)^{2/3} F^{2/3}$$

(3.7a-b)

Both the adhesion force and the contact radius at zero load are zero. Combining Eq. (3.4) and Eq. (3.7b) reveals that the friction force dependence on applied force is a power law, provided that the shear strength is constant. The necessary conditions for Hertz theory to be valid in AFM measurements are high loads and low adhesion. A rigid AFM tip commonly allows for sample deformation rather than tip deformation. Sneddon mechanics[48] applies to this situation where substrate deformation clearly predominates. If the influence of surface forces is negligible, Sneddon theory in conjunction with Hertz theory can give the total deformation of an easily deformable flat surface and an elastic, spherical, tip.

DMT theory

Derjaguin, Müller and Toporov[49] also included the adhesion force as a contribution to deformation. The expression for contact radius and contact area can be written as

$$a = \left[\frac{R}{K}\left(F + 2\pi\gamma R\right)\right]^{1/3} \qquad A = \pi\left(\frac{R}{K}\right)^{2/3}\left(F + 2\pi\gamma R\right)^{2/3}$$

(3.8a-b)

$$a_0 = \left[\frac{2\pi\gamma}{K} R^2 \right]^{1/3} \qquad\qquad F_{ad} = 2\pi\gamma R \qquad\qquad\qquad (3.9\text{a-b})$$

where a_0 is the contact radius at zero load. DMT theory can lead to an overestimated contact area. Note that Hertz formulae are recovered for non-adhering surfaces ($\gamma = 0$). The adhesive stress is continuous at $r > a$, but discontinuous at $r = a$. It is not physically consistent to have only compressive stresses in the contact area and adhesive outside. Therefore, DMT theory is applicable only to stiff systems with a low adhesion force and a small sphere radius, *i.e.* the regime in which elastic deformation due to surface forces is small compared to the interaction range.
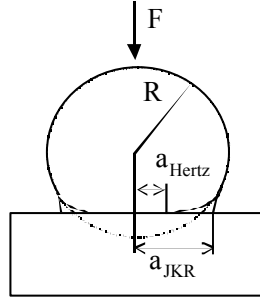

Fig. 3.2 Elastic deformation of a sphere against a flat surface according to Hertz (DMT) and JKR theory.

JKR theory

Johnson, Kendall and Roberts[50] included short ranged, attractive, forces inside the area of contact, but instead neglected long ranged forces outside the area of contact. The corresponding equations are

$$a = \left[\frac{R}{K} \left(F + 3\pi\gamma R + \sqrt{6\pi\lambda RF + \left(3\pi\gamma R\right)^2} \right) \right]^{1/3}$$

$$A = \pi \left(\frac{R}{K} \right)^{2/3} \left(F + 3\pi\gamma R + \sqrt{6\pi\gamma RF + \left(3\pi\gamma R\right)^2} \right)^{2/3} \qquad\qquad (3.10\text{a-b})$$

$$a_0 = \left(\frac{6\pi\gamma R^2}{K} \right)^{1/3} \qquad\qquad F_{ad} = \frac{3}{2}\pi\gamma R \qquad\qquad\qquad (3.11\text{a-b})$$

The abrupt transition at $r = a$ leads to the unphysical effect of infinite elastic stresses at this point. The attractive forces, acting over an infinitesimally small range, deform the profile inside the area of contact, resulting in a neck formation at separation. This causes an adhesion hysteresis between loading and unloading. In order for this condition to be realistic, JKR theory is applicable only when compliant materials of high surface energy and a large radius come into contact, *i.e.* in the regime where elastic deformation due to the adhesion force is large compared to its effective range of interaction. A further limitation is a possible underestimation of the loading force due to surface forces.

BCP theory

Burnham, Colton and Pollock[51] further improved the contact profile by adding a long ranged attractive force outside the area of contact. The surfaces bulge out towards each other on approach. The corresponding equations are

$$a = \left(\frac{R}{K}\right)^{2/3}\left(\frac{F}{R} + 6\pi\gamma K + \pi\gamma\right)^{1/3} \qquad A = \pi\left(\frac{R}{K}\right)^{4/3}\left(\frac{F}{R} + 6\pi\gamma K + \pi\gamma\right)^{2/3} \qquad (3.12a\text{-}b)$$

$$a_0 = \left(\frac{\pi R^{3/2}\gamma}{K}\right)^{1/3} \qquad\qquad F_{ad} = \pi R\gamma \qquad (3.13a\text{-}b)$$

BCP theory falls in-between those of DMT and JKR (see Maugis theory below) and is representative of many combinations of systems frequently used in AFM measurements. However, it may underestimate the pull-off force due to the Hertzian function used for the geometry.

Maugis theory

A universal theory has been formulated by Maugis[52] by modelling the interface as an opening crack. It is the most complete and accurate theory in that it applies to all materials, regardless of compliance, surface energy or sphere radius. The influence of each parameter on contact area is conveniently recognised in the dimensionless parameter, λ, given by

$$\lambda = \frac{2.06}{z_0}\sqrt[3]{\frac{R\gamma^2}{\pi K^2}} \qquad (3.14)$$

where z_0 is a typical equilibrium separation distance on an atomic scale. It is clearly seen that a small radius (R), low surface energies (γ) and stiff materials (large K) give $\lambda \rightarrow 0$, *i.e.* the DMT-limit. Similarly, $\lambda \rightarrow \infty$ for compliant materials, large radius and high surface energies, *i.e.* the JKR limit. BCP theory is valid for moderate values of λ. A continuous transition exists for λ between the two limits, but it must be solved numerically. Maugis's theory has improved the analysis of AFM force and friction measurements since they usually fall in the Maugis region. However, strictly quantitative values of stiffness and surface energy are still hard to obtain; bulk values of stiffness, radius and surface energy may not be applicable because of the local nature of the experiment.

Recently, Johnson investigated the relationship between friction and adhesion by extending the Maugis theory to include both static and sliding friction for a single asperity contact.[53] It was found that the relation between friction and adhesion was restricted to the periphery of the contact, in the presence of both normal and tangential forces. The model should hold for nanometer thin lubricant films if viscous dissipation is of minor importance.

A few important implications from contact mechanics theory should be mentioned. A finite contact area at zero load, dependent on the stiffness of both surfaces, has a major impact on the interpretation of AFM images. Delicate samples may deform and distort the image produced, particularly on a molecular level. Within this framework, it is also recognised that true atomic resolution is not possible on samples below a certain stiffness threshold. The discrepancy between true atomic spacings and that obtained in some contact AFM images has been attributed to atom displacement dependence on tip position, resulting in 75% error in spacing distance.[54] Finally, recalling the Derjaguin expression for the adhesion force (Eq. 3.2), it is instructive to notice how the choice of contact mechanics theory can produce inaccurate values for, *e.g.*, the surface energy. Thus, the validity of contact mechanics models should be scrutinised when applied to AFM adhesion or friction data.

4. SCANNING PROBE MICROSCOPY

The invention of the Scanning Tunneling Microscope (STM) in 1982 provided unique opportunities for obtaining three-dimensional images of surfaces with atomic resolution.[11,55,56] The STM works only for conducting or semiconducting surfaces since a voltage must be applied to both surfaces, creating a current between the tip and surface. The magnitude of this tunnelling current is an exponential function of the tip-sample distance, and it is this strong distance dependence which is utilised for topographic imaging. The limited application to conducting materials stimulated Binnig to develop the Atomic Force Microscope (AFM) with a novel force sensing technique which could be used regardless of material composition.[57] Today, a whole family of Scanning Probe Microscope (SPM) techniques are commercially available, specialising in imaging topographical, chemical, magnetic, viscoelastic, frictional, electrical and thermal features of a surface on the atomic to microscopic scale.[58]

4.1 Fundamental principles

All SPM's consist of a sensor that responds to a force, a detector that measures the sensor's response and a device for scanning. An AFM uses a sharp microfabricated tip at the end of a cantilever as the sensor and a position sensitive photodiode as the detector. The raster scanning necessary for imaging is obtained with the use of a piezo electric crystal (such crystals change size and shape in a controlled manner in response to an applied voltage). The cantilever deflection is measured by a laser beam, deflected off the back of the cantilever onto a detector. The detector response is linked to the piezoelectric crystal via a computer employing various feedback options to display the deflection as a function of position at the sample surface (see Fig. 4.1).
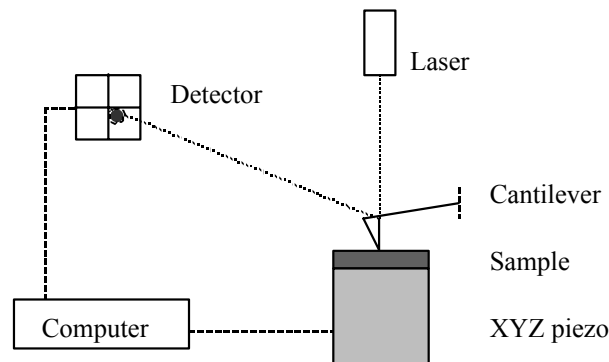

Fig. 4.1 Schematic drawing of the essential parts of an atomic force microscope.

At sufficiently small tip-sample separations the tip force can be estimated from *Hooke's law*[11]

$$F = -k_c \delta_c \qquad (4.1)$$

where k_c is the cantilever spring constant and δ_c the cantilever displacement (deflection). For small enough spring constants (<10 N/m) the sample surface will not be damaged by this deflection. This value is obtained by calculating the stiffness of an atom in a crystal of mass

10^{-27} kg vibrating at a frequency of 10^{14} Hz. However, other forces that contribute to the tip-sample interaction are the long-ranged magnetic, capillary, adhesion, van der Waals and electrostatic forces. This array of forces often requires a feedback loop to maintain a constant force or constant displacement between tip and sample during scanning.

The distance resolution in the normal direction depends on tip shape, cantilever spring constant, imaging mode and feedback loop design, as well as, experimental conditions (vacuum, vibration isolation etc). Generally, the best spatial resolution in the normal direction is fractions of a picometer (0.01 Å), while laterally features with a scale of 1 Ångstrom can be detected. Under normal operating conditions the resolution is decreased by one or two orders of magnitude due to electrical and thermal noise. This should be compared to another technique capable of measuring surface interactions: The Surface Forces Apparatus (SFA). Here, the vertical resolution is 1 Å, the force resolution is 10 nN and the lateral resolution is of a macroscopic scale. The reader is referred to the detailed review of Claesson *et al*[59] for an introduction to the SFA.

In order to enhance resolution, the noise level of all involved instrumental parts must be reduced to a minimum. Noise is a serious problem in AFM measurements and determines the signal to noise ratio (SNR), which must be greater than one for successful detection of cantilever displacements. Low-frequency noise (< 5 kHz) originates from building and instrument vibrations and will be sensed when the tip is in contact with a surface. Internal air flow, which often results from temperature fluctuation, is of immediate concern for the noise level and is probably the most important contribution, although detector noise and fluctuations in the phase and intensity of the laser diode emission also greatly affect the SNR. Fig. (4.2) shows the noise level of our atomic force microscope for a colloidal probe (see below for a definition) in contact with a surface in a liquid, and a bare cantilever in air. The first case represents the highest noise level experienced during a surface force measurement cycle. The second case indicates a low cantilever fluctuation in air, far away from the surface. The amplitude decreases when the surfaces are not in contact, implying that the best resolution for force measurements is better than 1 pN for this particular set-up and cantilever. Under imaging conditions the sampling rate between two points is 16 µs, which is fast enough for the present noise level to be of minor importance if the resonant frequency of the cantilever is higher than 65 kHz (usually satisfied).
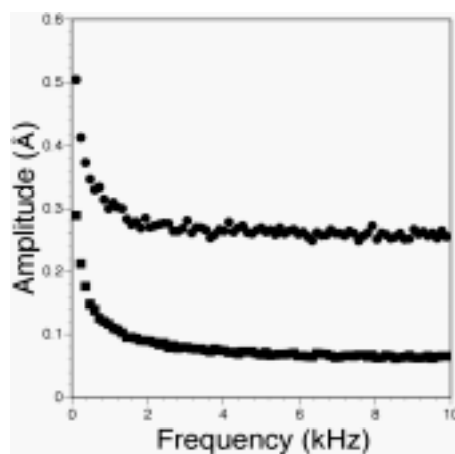

Fig. 4.2 Low-frequency noise detected for a colloidal probe in contact with a surface in liquid (**J**) and a bare cantilever in air far from the surface (**B**).

A good vibration isolation table combined with a hood under stable atmospheric conditions should leave the cantilever noise limited to thermal vibrations, equivalent to Brownian motion of a freely moving particle.[60] Thermal fluctuation in a viscous environment is a stochastic process described by a Langevin equation. The behaviour of a cantilever fixed at one end closely resembles an isolated one-dimensional harmonic oscillator with a total energy of kT and a noise level given by[11]

$$SNR \propto \sqrt{\frac{Qk_c\omega_0}{4kTB}} \tag{4.2}$$

where ω_0 is the resonant frequency and B the bandwidth of the spectrum analyser. Q is the quality factor, given by the full width at half-maximum of the cantilever amplitude divided by ω_0. Low thermal noise is hence achieved by using stiff cantilevers of high resonant frequency. However, the minimum detectable force of a thermally limited measurement for SNR=1 is[61]

$$F_{min} = \sqrt{\frac{4kTBk_c}{2\pi\omega_0Q}} \tag{4.3}$$

thereby providing optimum resolution for cantilevers of high resonant frequency, large quality factor and small spring constant. It has been shown that smaller cantilevers exhibit lower viscous damping, which further improves the force sensitivity.[61] Since the quality factor is roughly inversely proportional to the medium viscosity, the highest resolution will be attainable by immersing the system in a liquid of higher viscosity than air. This has the additional advantage that environmental aspects of noise are reduced.

A serious problem with cantilever design is the reflective metal layer coated on their back to enhance laser reflectivity when immersed in liquids. The resulting bimetallic cantilever will bend as the laser heats up the cantilever. Not strictly a source of noise, this will however cause a large drift in the deflection signal. Over a period of an hour it has been shown to induce deflections of more than 100 nm for a temperature rise of 3 K.[62] Even an uncoated, 100 μm long, silicon cantilever has a thermal coefficient high enough for drifting 1 nm, which may be of importance in sensitive force measurements. Leaving the system to equilibrate is thus rather important.

4.2 Imaging techniques

When the SPM was constructed for imaging there was no intention of including soft biological surfaces in the application - the first image was of an Al_2O_3 ceramic taken with a diamond tip in *contact mode*.[11] In this mode of operation the repulsive force between tip and surface ($\approx 10^{-7}$ N) is kept constant by the feedback loop, and the piezo adjusts the separating distance. Hence, the topographic image in contact mode is a plot of relative piezo voltage as a function of surface position (x,y).

If the feedback loop is turned off, the detector voltage also yields a topographic image. This *error mode* or *deflection mode* should normally be minimised, *i.e.* the feedback should be optimised. However, it is an option for high scanning rates when the feedback response is too

slow. As an example, atomic scale periodicities are scanned in this way to minimise the electrical noise level (see Fig. 4.3).
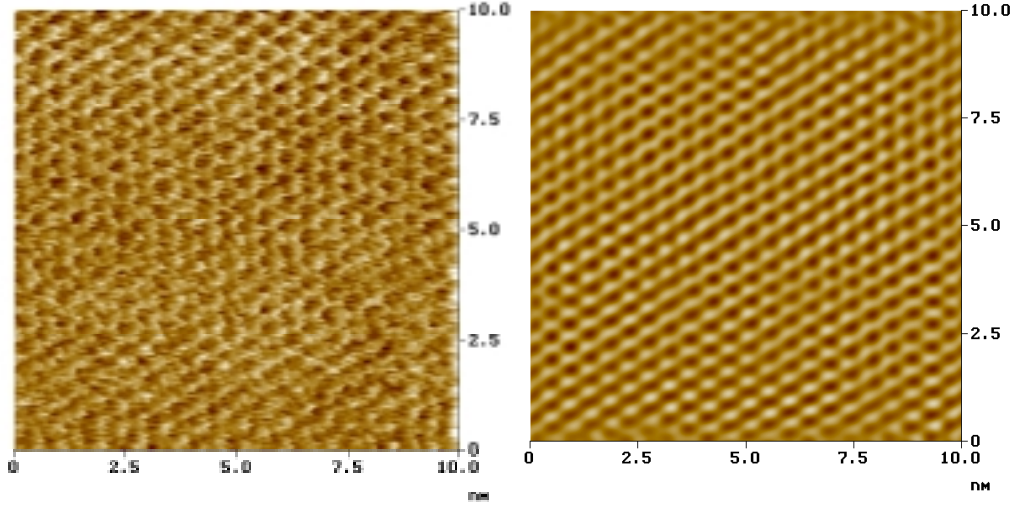

Fig. 4.3 AFM deflection mode image showing the hexagonal structure of mica. Left image
shows raw data whereas the right image has been filtered to reduce noise and
enhance the periodicity. The scan rate was 300 nm/s.

In *non-contact mode,* the cantilever is oscillated above the surface at its resonant frequency. The presence of surface forces (strictly force *gradients*) changes the cantilever resonant frequency as a function of tip-sample separation. Since the spring constant is proportional to the resonant frequency squared, shift in resonant frequency indicates cantilever deflection. Keeping the resonant frequency, or amplitude, constant keeps the separation constant, and the topographic image is generated by the relative piezo scanner position. *Intermittent contact*, or *Tapping Mode^{TM}*, is a resolution improvement over non-contact mode, where the contact time is short compared to the scanning speed that frictional and drag forces, which can be a problem in contact mode, are eliminated. Simultaneous detection of phase variations between the driving oscillator and detector signal during intermittent contact gives information about adhesion and viscoelastic surface properties.

The tip-surface separation distance at which the different modes operate can be seen in Fig. (4.4). Also shown in Fig. (4.4) is an example of SPM *lithography,* where the tip follows a pattern defined by a special algorithm. The letters were inscribed on a gold-coated mica sample by defining areas of higher tip force.

4.3 Force spectroscopy

The basic concept of a force measurement in the normal direction is to record the cantilever deflection (δ_c) as a function of intersurface separation. The controlled distance is the distance Z between the sample surface and the undeflected position of the cantilever, and the actual tip-sample separation $D,$ given by[63]

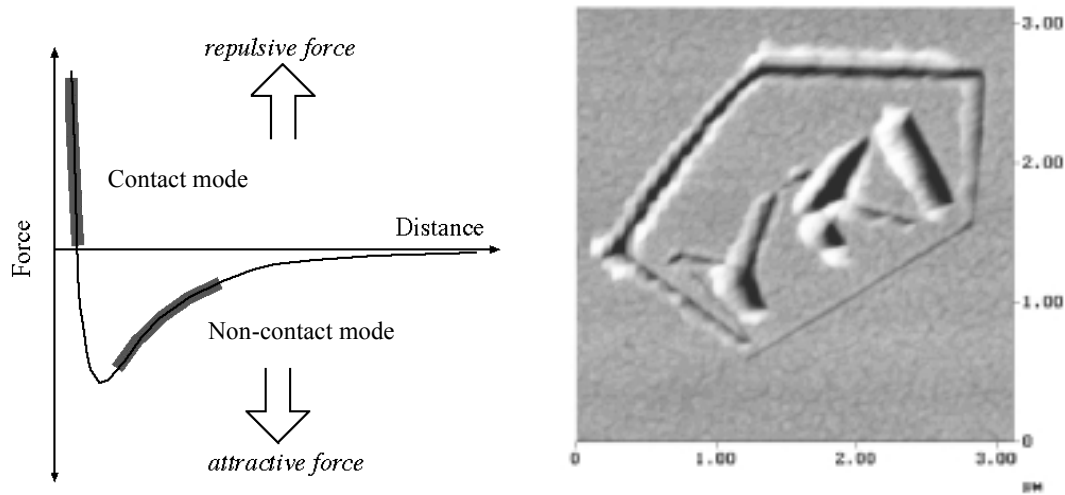$$D = Z - (\delta_c - \delta_s)$$ (4.4)

26

Fig. 4.4 The dependence on attractive and repulsive forces for contact and non-contact imaging (left). Contact mode image of lithographic nanoscale inscription on a gold coated mica (right). Image courtesy of Lachlan Grant and the author.

where δ_s is the sample deformation (see Fig. 4.5). Hence, the force-displacement curve differs from a true force-distance curve; both the tip-sample interaction $F(D)$ and the elastic force of the cantilever F (Eq. 4.1) contribute to the total interaction potential. The cantilever deflects until the elastic force of the cantilever equals the tip-sample interaction force. In other words, the system is in equilibrium at any point above the surface. It is important to remember that the model of springs in series used to characterise the interaction also incorporates deformation of the sample. Although rarely of major importance, the sample deformation becomes comparable to the cantilever deflection if the sample stiffness, k_s, is of the same order of magnitude as the spring constant of the cantilever.
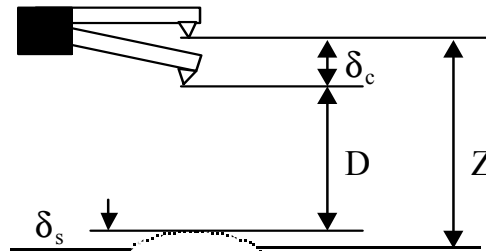

Fig. 4.5 The distance Z measured during a force-displacement curve differs from the actual separation D because of cantilever (δ_c) and sample (δ_s) deformation.

Force measurements are preferably carried out in a cycle of approach and retraction. A great deal of information can be extracted from the different regions of the force-displacement curve, but one should remember that artificial features can be present, the most important being electrical, vibrational and optical noise.

A typical force-displacement curve in the absence of adsorbed species, and the equivalent force-distance curve, is seen in Fig. (4.6). The cantilever starts far above the surface at point *A* where no distance dependent forces act on the probe. Fluctuations at this point give the current noise level. When the piezo has moved the sample (for MultiMode as in Fig. 4.1) to position *B* a repulsive force deflects it upwards, until point *C* is reached, where it jumps into contact with the surface at *D*. One could easily believe point *C* to be the point where *dF/dD=0*, but it is actually an effect of cantilever instability. When the gradient of the tip-sample force becomes larger than the elastic constant of the cantilever, equilibrium can no longer be maintained and the cantilever jumps into contact. The tip-sample distance at which this occurs can be determined by equating the force-distance derivative with the cantilever stiffness. The size of the jump can be reduced if the cantilever stiffness is increased. Increased stiffness lowers the force resolution but produces "nicer" force curves. An infinite stiffness yields complete force curves and can be realised if a feedback loop, *e.g.* a magnet, keeps the cantilever from deflecting during approach.[64] Contact is defined as the point where $d^2F/dZ^2 = 0$, *i.e.* where the curvature changes from positive to negative.[65] Strong repulsive forces may render the contact point impossible to detect. In such cases the sample or cantilever may be modulated and the decrease in amplitude chosen as hard contact.

The contact region *DE* is called the *constant compliance region* and reflects the combined deformation of probe, cantilever and sample. Along this line the contact area increases and can be calculated from[66]

$$k_{tot} = 2aE^*$$
(4.5)

where k_{tot} is the force per displacement required to compress the elastic contact, *a* is the contact radius and *E** the combined Young's modulus of tip, cantilever and sample (see Chapter 3). Hence, the constant compliance region can be used for extracting mechanical properties of the materials in contact, much in the same way as indentation experiments.[67]

However, matching of cantilever and sample spring constants is required if sample properties rather than cantilever properties are to be measured. Non-linear constant compliance slopes arise when the cantilever deformation is non-linear with applied load, or if the piezo crystal movement or detector is non-linear.

The piezo motion is reversed at *E* and the retraction continues via *F* and *G* back to the starting position *H≡A* to complete the cycle. At point *F* the energy stored in the cantilever becomes greater than the adhesive energy and the cantilever jumps to point *G*, where the long-ranged repulsive force still affects the cantilever deflection. Noise is known to affect the jump-off position in a force-distance curve, but applied load, velocity, surface energy, contact area and temperature fluctuations also contribute. Measurement of adhesion forces should therefore be considered as non-equilibrium experiments requiring a substantial amount of data, to be analysed on a statistical basis. The adhesion jump-off distance will always be larger than the jump-to-contact due to van der Waals adhesion. Some chemical bonds formed in contact or sample material wrapped around the tip also contribute to this jump.[68] The jump-off is also large for samples coated with thin liquid films, where a meniscus force prevents the tip from being pulled off. This can be prevented by making the tip hydrophobic.
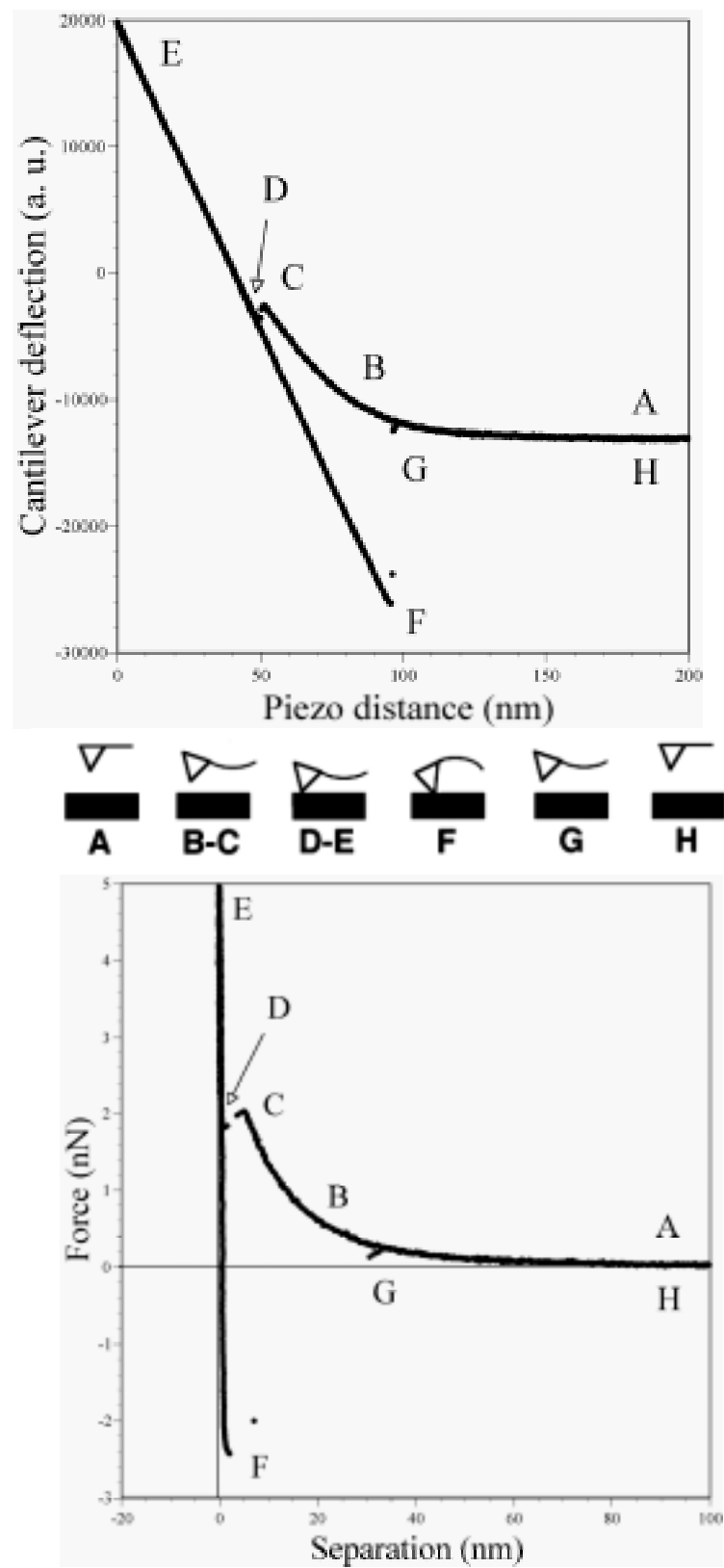
Fig. 4.6 Typical raw force-displacement curves (top) and the corresponding force-distance curves (bottom).

The system may manifest hysteresis between approach and retraction curves in three ways. First, the constant compliance slopes can be offset due to piezo hysteresis, non-uniform cantilever bending or tip friction in contact.[69,70] An inelastic response of the system due to surface deformation may also contribute to this offset. Second, hysteretic behaviour in the negative parts of the two curves just prior to/after contact is due to the work of adhesion. Third, far from contact above the surface the curves may be shifted vertically due to instrument drift at very low speeds, or because the liquid has a high viscosity. Weak cantilevers are affected by viscous drag forces on both approach and retraction, giving an apparently horizontal baseline falsely associated with a zero force. In the constant compliance region of Fig. (4.6), hard contact is assumed between the surfaces and subsequently equal cantilever bending is assumed to occur with equal piezo movement. The slope is therefore used to convert deflection data from detector voltage to cantilever deflection. However, care should be taken for contacts not resembling hard walls, *e.g.* surfaces coated with soft adsorbates like polymers, where the constant compliance slope is more gradual. This results in underestimation of both surface separation and interaction force when used in the conversion.[71] In such cases, a compressibility model must be used for correct scaling of adsorbate force components and layer thickness.

After the deflection data has been converted to a length scale, the cantilever deflection can be transformed to force by inserting the calibrated spring constant into Hooke's law (Eq. 4.1). Surface separation distance is calculated by subtracting cantilever deflection from the total piezo motion. Finally, the detector must be calibrated for each force curve in order to fix the zero separation and zero force - the force curve is detected on an arbitrary position on the detector. Zero separation is set at the onset of constant compliance. Practically this means pushing hard into the surface to ensure that any adsorbed layers are squeezed out. This introduces a delicate balance between finding true hard contact and possible non-linear cantilever bending at high forces resulting in artefacts. Zero force is set at a sufficiently large distance between the surfaces, longer than the range of the interaction force (point *A* in Fig. 4.6). At this point, the baseline can be assumed to be zero force if viscous forces can be neglected. Quite often the baseline is not exactly linear, but rather fluctuates in a sinusoidal fashion; an artefact easily recognised as laser light interference. Some light is reflected from the backside of the cantilever to the detector, but some amount goes through the cantilever or spills over the side. When this light is reflected from the sample surface, it interferes with that from the cantilever. The resulting oscillation in the baseline has a wavelength half of that of the laser (typically λ=330-340 nm for Digital Instrument). This effect is most noticeable for uncoated cantilevers in conjunction with highly reflective samples.

The colloidal probe

As mentioned earlier, in force measurements where other materials and geometry than the pyramidal silicon nitride tip are desirable, there is the possibility of attaching a probe to the cantilever to form one of the interacting surfaces.[72] Herein lies the true versatility of force spectroscopy, since virtually any material can be glued onto the cantilever and used as a probe. All colloidal probes used in this work were attached using a two component resin (Araldite, Casco AB) and were used for force measurements in aqueous electrolyte solutions and all quantitative friction force measurements. Araldite was consistently chosen as glue due to its good chemical and mechanical resistance, short hardening time (fully cured after 24 hours) and ease of use. Other popular adhesives (*e.g.* Epikote 2001) require heating
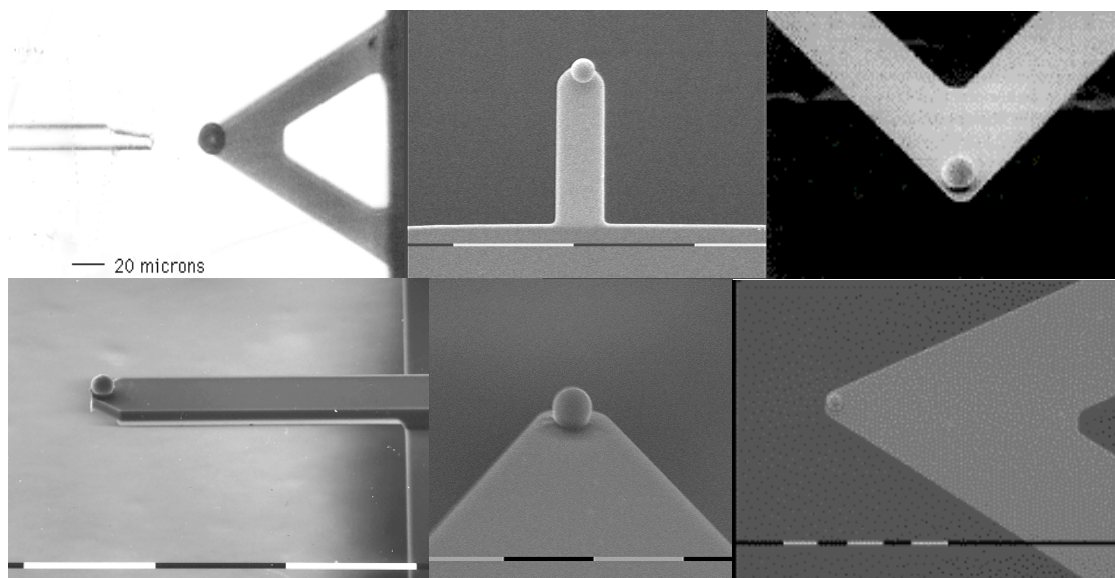
Fig. 4.7   A collection of colloidal probes. Clockwise from top left: micrograph showing glass fibre just after attaching an iron sphere to a tipless cantilever, 16 μm ceramic granule, 10 μm silica sphere, 4 μm silicon nitride sphere, close-up of silicon nitride sphere and a 18 μm iron sphere.

which can warp and permanently destroy the cantilever. Some glues are also prone to wet the cantilever. For immersion in organic liquids, molten granulated sugar is a good adhesive.[73]

The particle attachment procedure is as follows. One glass fibre is dipped in glue spread on a glass slide and moved with a micromanipulator to the apex of the cantilever. After depositing a small amount of glue, a second fresh fibre is used to pick up a sphere and subsequently position it on top of the glue droplet on the cantilever. In the case of attaching spheres smaller than 5 μm in diameter, an even thinner TiN whisker was attached to the end of the glass fibre.[74] The main advantages of this procedure to others are the perfect control of positioning of both glue and particle. Depending on the probe size, the precision of positioning can be within a micrometer. Finally, after the glue has hardened and immediately prior to the experiment, the cantilever with the attached particle is cleaned in order to remove organic and particulate contamination.

4.4 Friction force analysis

In addition to scanning friction *images,* it is also possible to quantitatively obtain the friction *force* when scanning along a line on the surface while monitoring the applied load. Mate *et al*[75] measured friction as a function of load between a tungsten tip and a graphite surface, introducing the term Friction Force Microscopy (FFM). Their results showed that friction exists in the absence of wear on an atomic scale. Since then, FFM has developed into a tool for understanding friction, wear and lubrication on the nanoscale.[76,77] Particular attention has been given to direct testing of contact mechanics theories since the uniform tip represents a single asperity. The rapid progress in cantilever and detector calibration techniques has enabled quantitative friction measurements where properties such as elasticity, shear stress

and relaxation times for viscous systems can be obtained. The quality and usefulness of the data is often set by whether the FFM measurements are static or dynamic, *i.e.* if the sample is modulated at a high frequency. Important improvements include the possibility of varying the probe material, thus making FFM complementary to the tribological Surface Forces Apparatus.

Acquiring and evaluating data from a friction measurement differs significantly from the procedure for force spectroscopy. The probe is scanned back and forth along a contact line of known length on the sample surface while the horizontal deflection data is recorded. The feedback signals must be optimised since the normal deflection, proportional to the applied load, must remain constant during the measurement. A typical plot of raw data is shown in Fig. (4.8) and is known as a *friction loop*.[75]
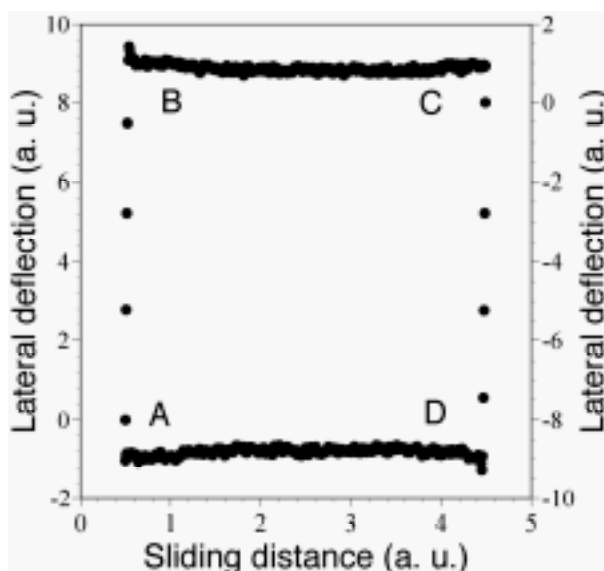

Fig. 4.8 Typical raw data (friction loop) obtained at constant load. Note that ABC denotes positive deflections and CDA negative deflections.

The probe starts at point *A*, where it experiences an increasing static friction force. Sliding begins when the static friction force is overcome, at point *B*, and continues until point *C* is reached. *BC* is known as the dynamic friction region. The motion is then reversed, and the a static friction force keeps the probe stationary from *C* to *D*. The cycle is completed with the dynamic friction region *DA*, bringing the probe back to the starting point *A*. Since the cantilever bends in opposite directions in *ABC* and *CDA*, these regions are defined as positive and negative deflections (see Fig.4.8). Consequently, the friction force is measured twice; once in each direction. There are several reasons for this. Firstly, when the probe encounters contact with the surface it might experience a lateral bending due to surface irregularities, giving a starting deflection value other than zero. Secondly, measuring friction in both directions averages any direction dependent friction. Thirdly, any unknown offset of the probe from the cantilever centreline results in different lateral spring constants for the two directions. The value evaluated from a friction loop is thus taken as half the value between forward and reverse scans in a friction loop. Each friction loop is performed at a constant applied load set by the user. Evaluation of friction as a function of applied load requires a substantial number of friction loops.

From a quantitative perspective, it is important to distinguish between friction force and lateral force. Sharp surface irregularities can induce "tripping" forces where the lateral signal is a combination of normal and lateral deflection due to the shaky motion of the probe over a large obstacle. This effect is usually seen as spikes in the friction loop and the effect increases with increasing sliding speeds, probe sharpness and acuteness. Another important aspect is the relative size of the static and dynamic friction regions. This is a delicate balance between sliding distance, torsional spring constant and probe size; the choice is dependent on which region one wants to highlight. One key-feature in friction loops from viscoelastic systems is the gradual transition from static to dynamic friction, which under the right conditions also reveals whether stick-slip will occur (see Chapter 6).

The conversion of lateral cantilever bending from voltage to friction force can be done either by using the lateral spring constant (N/m) or the torsional spring constant (N/rad). Some authors use the constant compliance region from a force-distance curve, whereas others use a "lateral constant compliance region" to convert deflection data.[78-80] The first method assumes equal bending both normally and laterally, and both methods assume a purely elastic contact. Other authors have invented conversion methods based on scanning at different angles.[76] Procedures that are more reliable have been developed where the bending angle rather than the lateral displacement is measured.[78,81-83] Recently, Cain *et al*[84] and Piétrement *et al*[85] further investigated the static friction part of the friction loop in an attempt to establish a standard calibration procedure for friction force measurement. Here the detector must also be given a factor describing the bending angle.

If the friction force is calculated with the lateral spring constant (N/m), a conversion factor describing the lateral *displacement*, not the bending, is needed. **Paper III** shows the error involved in using a sensitivity value obtained from a lateral constant compliance region, but describes how it can be successfully used in measurement of energy dissipation during friction-load experiments. When a cantilever bends laterally, the actual cantilever motion is a function of the probe arc length as the probe "rolls" on the surface during bending. Hence, the probe height can be included in the sensitivity to account for this. Alternatively, the sensitivity factor can be separated from geometrical terms. If the cantilever is described in terms of its torsional spring constant, k_θ, (N/m·rad) the friction force becomes

$$F_f = S_d k_\phi h P \tag{4.6}$$

where S_d is the detector factor (rad/V), h the probe height (m) and P input signal (V). The input signal is taken as half the value between forward and reverse scans in a friction loop.

Calculation of applied load requires calibration of the piezo (see below). During a friction measurement only a relative *detector* setpoint voltage is given, so it is important to keep track of both initial and final piezo signals. A previously determined conversion factor obtained from scanning features of known heights, S_{piezo}, is necessary for the piezo voltage to be expressed in units of length. The relation between piezo crystal and detector voltage is determined by the manufacturer and given as a specific constant, C_{det}. The applied load, L, becomes

$$L = (V_1^{det} - V_0^{det}) S_{piezo} C_{det} k_c \tag{4.7}$$

where V_1^{det} is the detector voltage at which a friction force has been measured, and V_0^{det} the initial detector voltage at zero load. An uncertainty exists in the position of zero applied load, particularly when the loads become comparable to the surface forces present. A convenient position to choose is the part at which the normal cantilever deflection is zero, *i.e.* point *A* in Fig. (4.6). Thus, the total load becomes

$$L_{tot} = L_{applied} + L_{force} \tag{4.8}$$

where an attractive interaction force is considered as an extra positive contribution to the total load. The same result should be obtained from taking a force curve, in the absence of drift. Moreover, in cases where a strong adhesion is present such a force is conventionally treated as a "negative" applied load. As discussed below, this negative load constitutes a non-stable sliding, leading to jump-off before the friction force reaches zero, and is readily predicted from contact mechanics theories.[86]

4.5 Calibration procedures

The reliability of AFM measurements, whether performing force spectroscopy or imaging magnetotactic bacteria, is a function of the intrinsic properties of the instrument materials. A piezoelectric actuator is truly a piece of advanced ceramic, with the ability of changing dimensions in response to an applied voltage. Nevertheless, care must be taken in using them – they often show transient behaviour. Detectors have the tendency of being non-linear, particularly as they consist of four parts clamped together. Moreover, although cantilever production has improved, the spring constants may deviate considerably from batch to batch and from the values provided by the manufacturer. Calibration is of fundamental concern, inevitable and nowadays routine-like for any trained microscopist.

Normal spring constant

Standard AFM imaging techniques require only a qualitative estimate of the cantilever spring constant to match with the sample stiffness. Since the AFM is mostly used for imaging, the manufacturers do not provide data on accurately determined spring constants.[*] It is a well-known fact that the stated value can differ by up to 20% for normal spring constants whereas the value of the lateral constant is not given at all.[73] For quantitative force measurements accurate determination of the spring constant is of utmost importance and has to be calibrated by the operator regardless of other sources of information. There are a number of methods available for obtaining the spring constant, based on either geometry or measurement of the resonant frequency. The former includes simple calculations from cantilever geometry,[87] whereas the latter include measurement of the shift in resonant frequency due to an added mass[88] and measurement of thermal noise[89]. Other methods frequently used are static deflection due to added mass[90] and a combination of cantilever mass, dimensions and resonant frequency[91]. The first three methods have all been used in the present work for determining the normal spring constant and will be presented here in more detail.

---

[*] Silicon-MDT recently offered customers cantilevers individually calibrated with a thermal method.

Cantilevers are manufactured with different shapes and spring constants, V-shaped Si_3N_4 and rectangular Si cantilevers being the most common.[92] The V-shaped levers are coated with gold for increased laser reflectivity which seriously affects the applicability of certain stiffness calculation methods. AFM cantilevers behave as Hookean springs, therefore the stiffness, k_c, is given by[11]

$$k_c = \frac{3EI}{L^3} = \frac{Ewt^3}{4L^3}$$

(4.9)

where E is Young's modulus, L the cantilever length, I the moment of inertia, w the leg width and t the leg thickness. Note that the latter part of Eq. (4.9) is valid only for a single beam cantilever. Sader[91] used the parallel beam approximation to extend this expression to V-shaped levers, thus introducing the angle 2θ between the legs, giving

$$k_c = \frac{Ewt^3}{2L^3} \cos\theta \left\{ 1 + \frac{4w^3}{b^3} \left(3\cos\theta - 2 \right) \right\}$$

(4.10)

where b is the distance between the legs at the base (see Fig. 4.9). Neumeister and Ducker[93] provide what is probably the most accurate expressions for V-shaped cantilever spring constants calculated from dimensions. The applicability of the geometrical approach is hampered by the need for evaluation of dimensions in a Scanning Electron Microscope, which requires permanently coating the cantilever with a metal. The thickness of the cantilever has to be determined with a high degree of accuracy in order for the stiffness to be defined with a maximum relative error of 20%. This is usually difficult since the thickness is of the order of 1 μm. The calculations are complicated by the effect of the gold layer deposited on the back of the cantilever due to the difference in Young's modulus for gold and silicon nitride.[87]
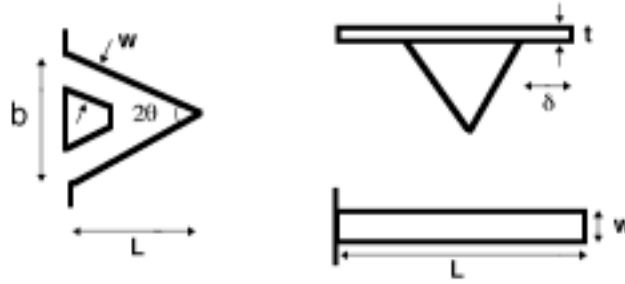

Fig. 4.9 Definition of V-shaped cantilever and tip geometry (left and top right) and rectangular cantilever (right) for calculation of normal and lateral spring constants.

Cleveland et al[88] introduced an experimental method for determining k_c, which is widely used because of its high accuracy and simplicity. By adding a weight of known mass to the cantilever, the resonant frequency will shift to a lower value. The spring constant is given by

$$k_c = (2\pi)^2 \frac{M}{(1/\omega_1^2) - (1/\omega_0^2)}$$

(4.11)

where M is the added mass and ω_0 and ω_1 are the unloaded and loaded resonant frequencies, respectively. The mass is added by placing microspheres of materials with high density (*e.g.* tungsten) and known radii on the cantilever end. However, it is no trivial task to place a sphere to within a micrometer without bending the cantilever and contaminating the surfaces. Consequently, in this work a microscope has been used in conjunction with a home-built holder, where two 10-micron thick glass fibres are attached. One is used for placing a small amount of adhesive on the cantilever, and the other is used for picking up a particle. Some viscous fluids have ideal adhesive properties at room temperature. In my case, earwax has been a long-running favourite, but facial grease[*] has also proved useful. Tungsten spheres[94] give good accuracy because of their high density and the possibility to attach them to the cantilever using a negligible amount of adhesive.

Fig. (4.10) shows a plot of added mass against frequency shift for the two tipless V-shaped cantilevers most used in this work. Independent measurements of cantilevers from the same batch by Guldberg-Pedersen resulted in a 90 % agreement.[95]

The equipartition theorem states that the thermal energy, k_BT, is equally divided into potential energy and kinetic energy if the cantilever behaves as a one-dimensional oscillator.[89,96] The spring constant can then be linked to the average fluctuations of the cantilever in thermal equilibrium according to

$$k_c = \frac{k_BT}{<x^2>}$$
(4.12)

where $<x^2>^{1/2}$ is the root-mean-square cantilever displacement. The method is most accurate for weak levers, made by several manufacturers, and is therefore frequently incorporated into the AFM software. However, low frequency noise compromises this method, as does the choice of time required for thermal equilibrium.

An improvement of this method has been used extensively for evaluation of spring constant, resonant frequency, quality factor and viscous drag coefficient of a cantilever at different distances from a surface.[96-103] According to the fluctuation-dissipation theorem the noise power spectrum is

$$\frac{d|z^2|}{d\omega} = \frac{k_BT}{\pi n} \frac{\gamma}{\left(\omega_0^2 - \omega^2\right)^2 + \gamma^2\omega^2}$$
(4.13)

where γ is the damping constant and m the effective cantilever mass. The spring constant is obtained from $\omega_0 = (k_c m)^{1/2}$. This procedure involves taking an AFM image in deflection mode with the feedback disabled and the cantilever far above the surface after thermal equilibrium has been reached. The image is then Fourier transformed and plotted as a function of frequency (Fig. 4.10). An iterative fitting of Eq. (4.13) provides the relevant parameters, once conversion from voltage to lengthscale and correct scaling has been done. A comparison between this method and the added mass method for a V-shaped cantilever yielded 95% agreement. For long, rectangular, cantilevers of very low resonant frequencies

---

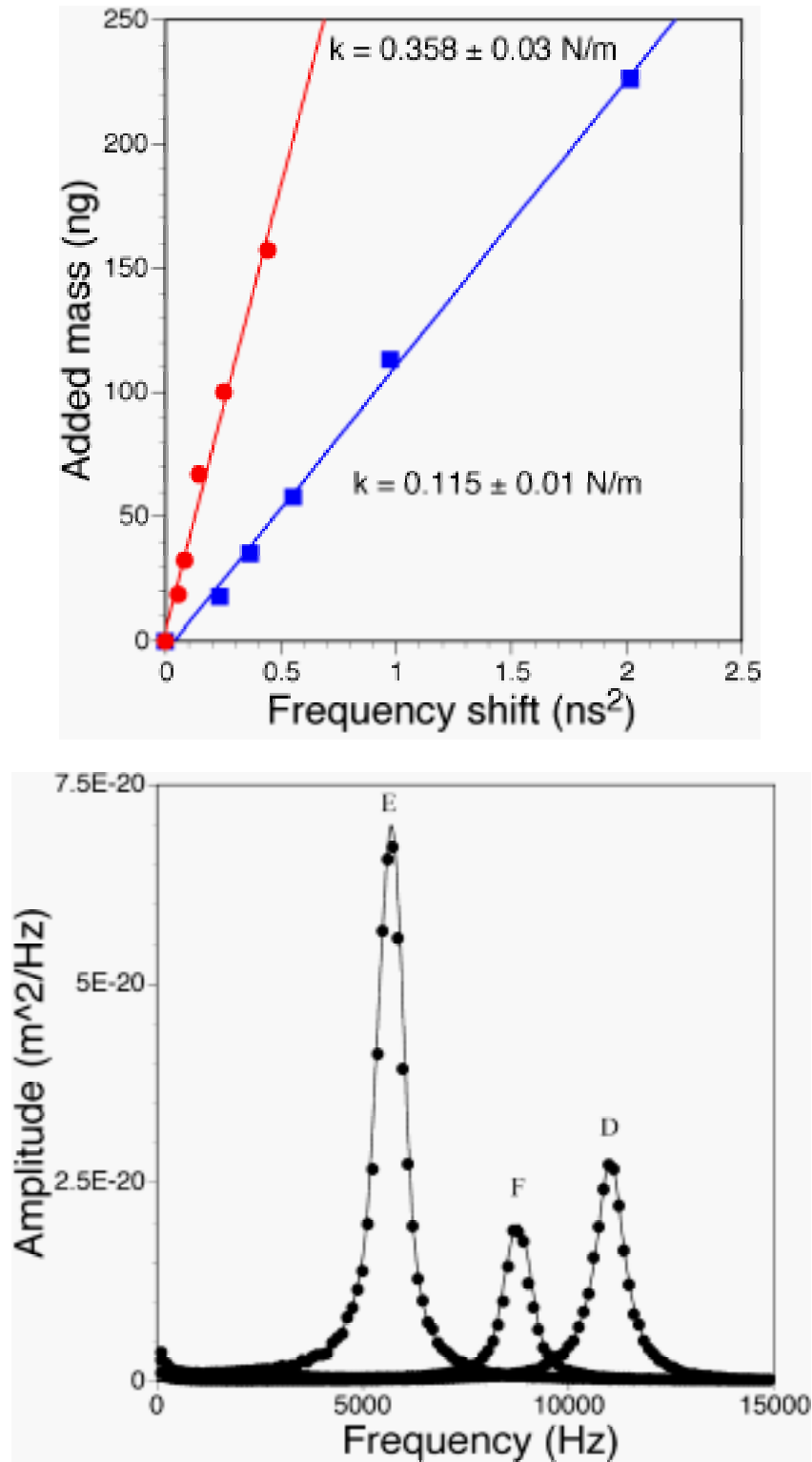[*] Kindly brought to my attention by Goran Bogdanovic

Fig. 4.10 <u>Top:</u> Evaluation of normal spring constants by the added mass method for V-shaped short, wide (J) and long, wide (B) tipless levers. <u>Bottom:</u> Fourier transformed cantilever amplitude induced by thermal vibrations for three rectangular cantilevers of different lengths, fitted to a Lorentzian function. The spring constants are 0.031 (D), 0.013 (E) and 0.043 (F) N/m, respectively.

this method proved to be the best in our case, because adding tungsten spheres shifted their frequencies below the resolution limit of the inbuilt spectrum analyser.

Torsional spring constant

Early friction measurements used the normal spring constant when transforming lateral deflections to frictional forces.[75] Since the stiffness in the two directions rarely coincide, one must also have knowledge of the lateral, or torsional, spring constant if the lateral detector signal is to be quantified into friction force. This is more difficult and an experimental method has not yet been as successfully developed as for normal spring constants. Frequency methods are not applicable since the torsional resonant frequencies are in the MHz regime. Extensive mechanical studies on cantilevers have yielded equations for the lateral stiffness of V-shaped cantilevers.[78,83,93,104] However, these are significantly oversimplified and more relevant to rectangular cantilevers. The expression for the lateral spring constant, k_{lat}, is given by

$$k_{lat} = \frac{Gwt^3}{3h^2L} \tag{4.14}$$

where G is the shear modulus and h is the tip height including half the cantilever thickness.[82,105,106] Hazel and Tsukruk[106] and Noy et al[107] suggested a ratio between the normal and lateral spring constants based on only the leg angle and cantilever length. Finite element calculations confirmed the accuracy of this method[106] but also indicate that coupling effects between normal and torsional deflection exist for V-shaped cantilevers, significantly reducing their appropriateness in quantitative friction force measurements.[108,109] Coupling effects are seen when normal deflections contribute to the lateral deflection and the cantilever twisting is not a linear function of the lateral force. Rectangular cantilevers bend linearly and are preferred to V-shaped; the latter should only be used at low applied loads.

The procedure for determining torsional spring constants of rectangular cantilevers used in this work consisted of measuring the shift in resonance frequency and calculating the normal stiffness according to the added mass method. The lateral spring constant is subsequently calculated from the ratio of Eq. (4.14) and Eq. (4.9)

$$\frac{k_{lat}}{k_c} = \frac{2L^2}{3h^2(1+v)} \tag{4.15}$$

which only depends on cantilever length, probe height and Poisson's ratio. This procedure prevents inconsistent calculation errors introduced from non-coupled stiffness equations.

Paper IV presents a novel technique for experimental determination of cantilever torsional spring constants. The technique is non-destructive, requires only a substrate with a sharp feature, is valid regardless of cantilever geometry or AFM used and is based on a sound theory of mechanics of materials. In fact, it can be used *in situ* prior to friction measurements. Similar procedures have appeared more recently, but require a rigid glass fibre to be glued to the cantilever.[81,110] Our procedure is based on simultaneous measurement of normal and lateral deflections during a force curve against a sharp surface feature. By monitoring the position of the sharp feature such that the cantilever lands different distances from the
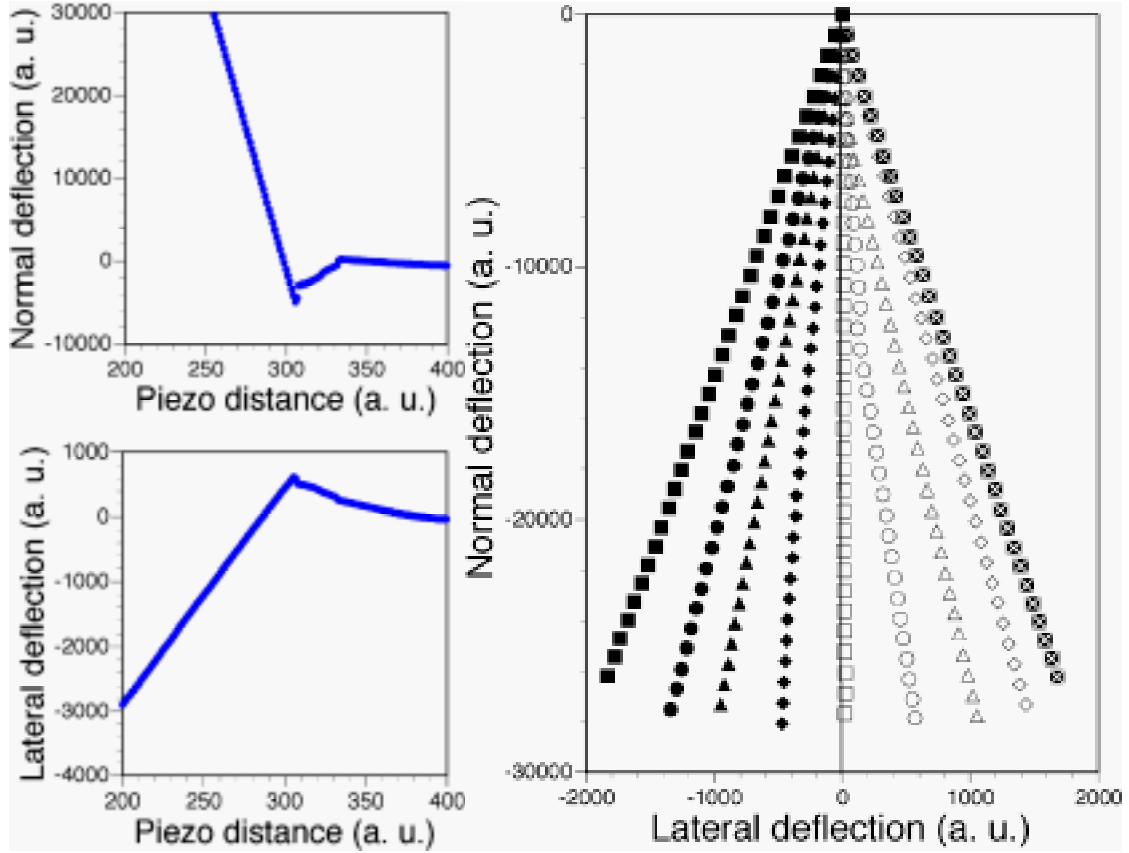
*Fig. 4.11 Raw data from calibration of torsional spring constants. <u>Left:</u> Force curves in the normal (top) and lateral (below) direction. <u>Right:</u> Constant compliance slope ratio for different values of ±a from the centreline (G). See **Paper IV** for details.*

centreline of the cantilever long axis, the resulting moment can be related to the torsional spring constant according to

$$k_\phi \phi = Fa \tag{4.16}$$

where k_ϕ is the torsional spring constant, ϕ the bending angle, F the applied load and a the distance associated with the moment. The connection to the normal spring constant, torsional constant compliance slope (C_ϕ) and the normal constant compliance slope at certain values of a (C_z^a) via an angle detector constant β is

$$\frac{C_\phi C_z^0}{k_c C_z^a} = \frac{\beta}{k_\phi} a \tag{4.17}$$

Fig. (4.11) shows a simultaneously obtained normal and lateral force curve and a collection of torsional constant compliance slopes for different values of a used for evaluation of the torsional spring constant.

Customised ordered tipless, uncoated, rectangular cantilevers made from silicon were used for experimental determination of torsional spring constants. Three cantilevers of different

lengths, varying from 90 to 130 μm, gave spring constants of the order of 20 nNm/rad, which disagreed by a factor of 2-5 to the calculated values using Eq. (4.14). An inconsistent trend was also seen with respect to cantilever length. Several reasons can explain this discrepancy. First, calculated values depend on material properties, which can vary depending on deposition technique. Second, the dimensions and normal spring constants provided by the manufacturer are consistently erroneous. Thickness variation between different cantilever chips is probably the main source for the discrepancies in the spring constants obtained. Careful calibration of the piezo was performed before proceeding with the measurements. Estimating all experimentally obtained parameters in Eq. (4.17) to be of 99% accuracy, leaves the normal spring constant as the largest source of error. The added mass method is accurate to 90 %, therefore the experimentally obtained torsional spring constants are pessimistically estimated to an uncertainty of 15 % at the most.

Detector calibration

Most AFM detectors consist of position sensitive photodiodes in a quadrant arrangement (Fig. 4.12). The vertical and lateral signals are taken as the difference between opposing halves scaled by the sum of all four quadrants. This ensures that background stray light is cancelled out. One advantage of this detector layout is that it is immune to lateral misalignments. Detectors are known to be non-linear and need independent calibration schemes. Calibration procedures vary depending on what kind of signal is used for measurement. Force curves require a special method, whereas imaging rarely requires deflection units to be converted, because the signals are mainly used for feedback purposes and the surface feature heights are obtained from the piezo motion.

$$Vertical = \frac{[(A+B)-(C+D)]}{[(A+B+C+D)]}$$

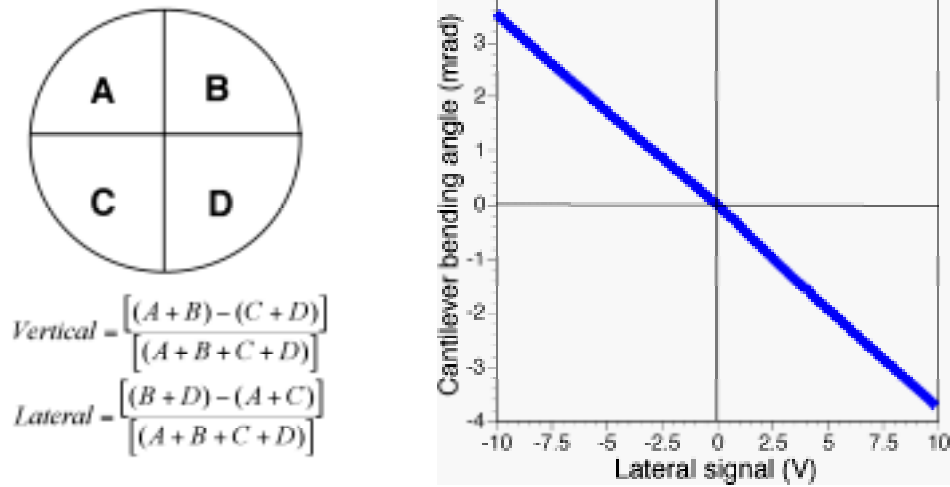$$Lateral = \frac{[(B+D)-(A+C)]}{[(A+B+C+D)]}$$

Fig. 4.12 Detector photodiode arrangement and their contribution to signal output (left). Calibration of detector sensitivity to lateral cantilever bending (right). The most non-linear region is around zero lateral deflection.

The main mode where a detailed knowledge of the detector response is needed is in quantitative friction measurements. **Paper III** describes a fast and convenient detector calibration method independent of experimental set-up. Here the laser is focused on a reflective flat sample and directed into the detector. A stepper motor or a translation stage is

used to tilt the sample to known lateral angles. Recording the lateral detector signal at different angles provides a sensitivity factor describing torsional bending, independent of the cantilever used. The angle-deflection ratio is constant and obtained from a linear fit to the data (Fig. 4.12). We have used this technique for three different detectors of the same model and brand and found large differences. Even when neglecting some obviously non-linear detector areas, the sensitivity factors differed by up to 400%. Clearly, the particular detector used must be individually calibrated and non-linear areas avoided.

Piezo electric scanners

SPM scanners are made of piezoelectric ceramic materials that respond with a change in geometry to an applied voltage, enabling them to act as extremely fine positioning stages with sub-angstrom resolution. Most scanners are made by sintering a pressed body of lead zirconium titanate, resulting in a polycrystalline material of randomly aligned dipole moments in the crystals. Heat treatment followed by rapid cooling aligns and freezes the dipoles in the aligned state. Depoling occurs if the scanner is not used over a period of weeks (ageing), but also if subjected to temperatures in excess of 150°C. Hence, SPM operation above room temperature requires a thermally isolated scanner (cantilever thermal drift is an additional obstacle for successful imaging). The amount of expansion of the piezo crystal is determined by a sensitivity factor, setting the relative motion for a given applied voltage in each direction.

The relationship between voltage and expansion is not linear, and the sensitivity also changes with time due to intrinsic nonlinearity, hysteresis, creep and ageing of the piezoelectric scanner material. Nonlinearity is manifested in non-uniform spacing and curvature in images of periodic structures. Hysteresis is best detected by comparing forward and reverse scans for shifts in surface features. Creep is an effect of time-dependence in the response to a voltage of the piezoelectric material. Zooming in on a smaller area during scanning is likely to be affected by creep, but easily eliminated by repeated scanning. The intrinsic behaviour of scanners necessitates several parameters to correct for the non-ideal motion. This means that scanner sensitivity values must be calibrated on a regular basis.

All scanners used here have been calibrated by software controlled procedures after scanning a reference grid of known surface feature dimensions of the same scale as that of the subsequent measurement. Estimated dimension error after calibration in the xyz-directions is less than 1%. A complementary calibration procedure relying on laser interference has also been used.[111]

5. SILICON NITRIDE SURFACE FORCE MEASUREMENTS

Numerous force measurements have been reported where one surface consists of silicon nitride, owing to the fact that many cantilever tips are made from deposition of silicon nitride. Specific measurements between symmetric silicon nitride surfaces were first reported by *Senden et al.*[112] Although their purpose was to establish a procedure for non-contact imaging, utilising the electric double layer repulsion, values for surface charge density and potential were extracted from fits to DLVO-theory in alkali electrolyte solutions. Two subsequent papers examined silicon nitride interactions in more detail.[113,114] Practical aspects of silicon nitride interactions have been reported by several authors;[80,115-117] *e.g.* surfactant adsorption has been correlated with suspension stability, and surface charging has been related to differences in the magnitude of the adhesion force.

5.1 van der Waals interactions

Attractive van der Waals forces have, for obvious reasons, been measured at early stages of AFM development.[118,119] When Weisenhorn *et al* found that the imaging force applied on the sample could be dramatically reduced if the system was immersed in water, it was not only assigned to a reduced adhesion force but also to a smaller Hamaker constant.[120] This was a great leap forward towards imaging soft, biological, samples and also a kick-off for specific force measurements.

The AFM cantilever tip can safely be approximated as consisting of a pyramidal base and a spherical cap[121,122] with radius R in the case of tip-sample interactions over separations less than 5 nm (see Fig. 5.1). The situation is much more complex at larger separations where the interaction also is affected by the pyramidal base. The van der Waals force between a tip and a flat substrate can be expressed as

$$F_{vdW}(D) = -\frac{A_{132}R}{6D^2} \qquad (5.1)$$

where D is the separation distance and A_{132} the Hamaker constant for materials *1* and *2* interacting over medium *3*.

Eq. (5.1) clearly illustrates that the van der Waals force is attractive (negative) if the Hamaker constant is positive, and repulsive (positive) if the Hamaker constant is negative. Repulsive van der Waals forces have been known to exist in certain systems for some time, *e.g.* in liquid helium wetting of almost any surfaces, but direct and controlled experimental evidence have been scarce. Visser[123] has given an early overview of work on negative Hamaker constants based mainly on surface tension data and particle rejection at solidification fronts. Negative constants have also been derived from adsorption of sucrose at the air/water interface[124] and from wetting transition behaviour.[125]

In the wake of AFM force measurements, repulsive van der Waals forces have been predicted in highly polar liquids, where the interaction was attributed to a strong entropic contribution from the zero-frequency term of the Hamaker constant.[126] Weisenhorn *et al*[127] confirmed this with force measurements between a silicon nitride tip and mica in formamide. Hutter and
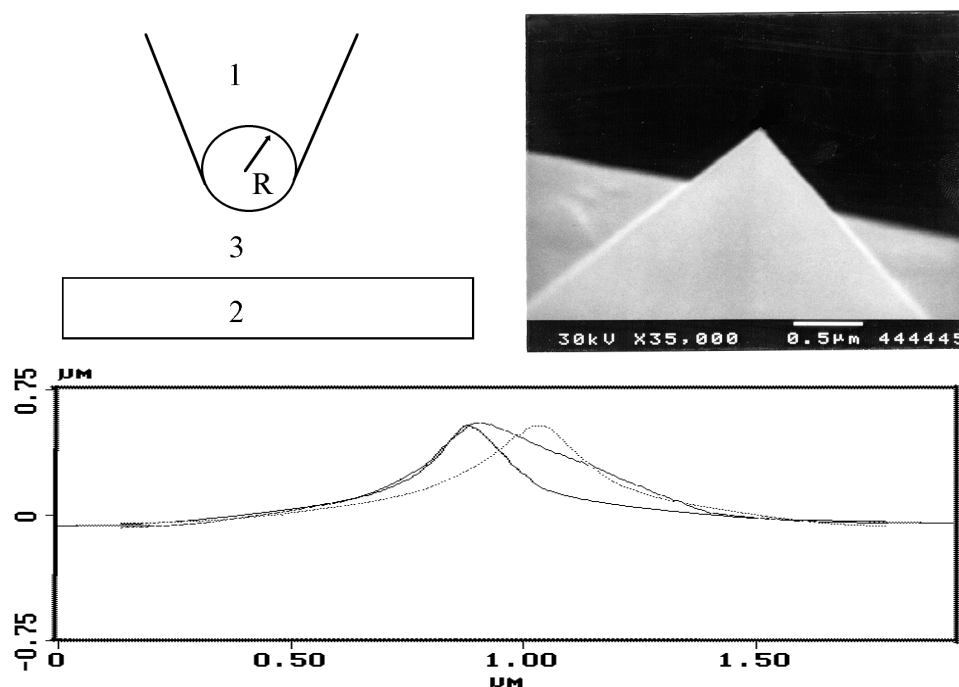
Fig. 5.1 Tip geometry represented as a pyramidal base with spherical cap of radius R (top left). The radius is evaluated from SEM-images (top right). Tip shape evaluated from inverted imaging at 0°, 60° and 120° tip rotation (bottom).

Bechhoefer[128,129] went a step further when they showed experimentally how the dispersion force was attractive, close to zero and repulsive between a silicon nitride tip and mica in ethanol, 1-methylnaphtalene and 1-bromonaphtalene, respectively. Their purpose was to eliminate the long-ranged attraction to improve imaging quality. Recently Milling *et al*[130] presented the first direct AFM measurements of repulsive van der Waals forces in different liquids, where the predicted outcome was based on Lifshitz theory. Their results, using gold and PTFE surfaces, were unexpectedly attractive in polar solvents but repulsive in apolar liquids.

In the study of both attractive and repulsive van der Waals interactions in **Paper I**, force measurements were conducted in two different media of low dielectric constants. Measurements were performed between insulating, non-magnetic materials in non-polar media in order to attribute the measured forces to a van der Waals force only. 1-bromonaphthalene and diiodomethane were chosen as media for interaction between two silicon nitride surfaces (symmetric system) and between silicon nitride and silica (asymmetric system). An AFM tip consisting of amorphous silicon nitride was used together with a polished, polycrystalline silicon nitride substrate, etched in hydrofluoric acid, as the symmetric system. Silica surfaces consisted of glass and an oxidised silicon wafer. The dielectric response function for all materials and media were evaluated according to the procedure outlined in *Chapter 2* and the resulting Hamaker constants and van der Waals interactions are shown in Table 5.1.

Table 5.1   Nonretarded Hamaker constants and resulting van der Waals interaction for the systems in this study.

System (tip - medium - substrate)	$A_{132}/10^{-20}$ J	Resulting interaction
Si_3N_4 - diiodomethane - β-Si_3N_4	1.0	Attractive
Si_3N_4 - 1-bromonaphthalene - β-Si_3N_4	2.8	Attractive
Si_3N_4 - diiodomethane - SiO_2	-0.8	Repulsive
Si_3N_4 - 1-bromonaphthalene - SiO_2	-0.2	Repulsive

The sphere-plane geometry of the tip-plate interaction was substantiated by measuring a tip radius from SEM-images, giving values varying between approximately 40 and 60 nm for cantilevers from the same batch (Fig. 5.1). Force-distance curves for the symmetric and asymmetric systems across diiodomethane are shown in Fig. (5.2) together with raw cantilever deflection and piezo movement data overlain with theoretical van der Waals curves. Approach speed was kept between 5 nm/s and 500 nm/s, slow enough for hydrodynamic effects to be of minor importance. Slower speeds led to more distortion and uneven cantilever bending in contact (the same trends were seen for higher speeds).

The asymmetric system displays a short-ranged repulsion in both approach and retraction curves, which is attributed to a repulsive van der Waals force as indicated by the theoretical fit. For the symmetric system, an attractive jump-in is observed on approach and a strong adhesion observed on retraction. The magnitude of the force and the distance dependence correspond well to an attractive van der Waals force. The interaction range is sufficiently large for Lifshitz theory to be applicable.[131] A similar behaviour was obtained in 1-bromonaphthalene, but here the forces were even more short-ranged, as predicted from Lifshitz theory. These forces barely exceeded the instrument resolution of the present experimental set-up ($\approx$20 pN), but the change from a repulsive to an attractive interaction could nevertheless be seen. No significant alterations occurred when changing the oxidised wafer to the glass surface.

An interesting feature seen in the raw data, inset in Fig. (5.2), is the hysteresis between approach and retraction curves.[69,132] Depending on the sign of interaction, the retraction curve shifts above or below the approach curve due to the exerted viscous force on the cantilever as it is withdrawn from the sample surface. The viscosity of the liquids may in fact be calculated from force measurements if the cantilever geometry is correctly modelled.

Replacing one surface with another and turning an attractive van der Waals force into repulsion has important implications in several areas. Firstly, the weak repulsion facilitates imaging on sensitive, biological samples, *e.g.* DNA, where the tip-sample contact force must be minimised to prevent destruction. Secondly, the absence of adhesion could improve industrial processes such as filtration where otherwise an ever-present attractive van der Waals force inevitably induces agglomeration in the membrane.
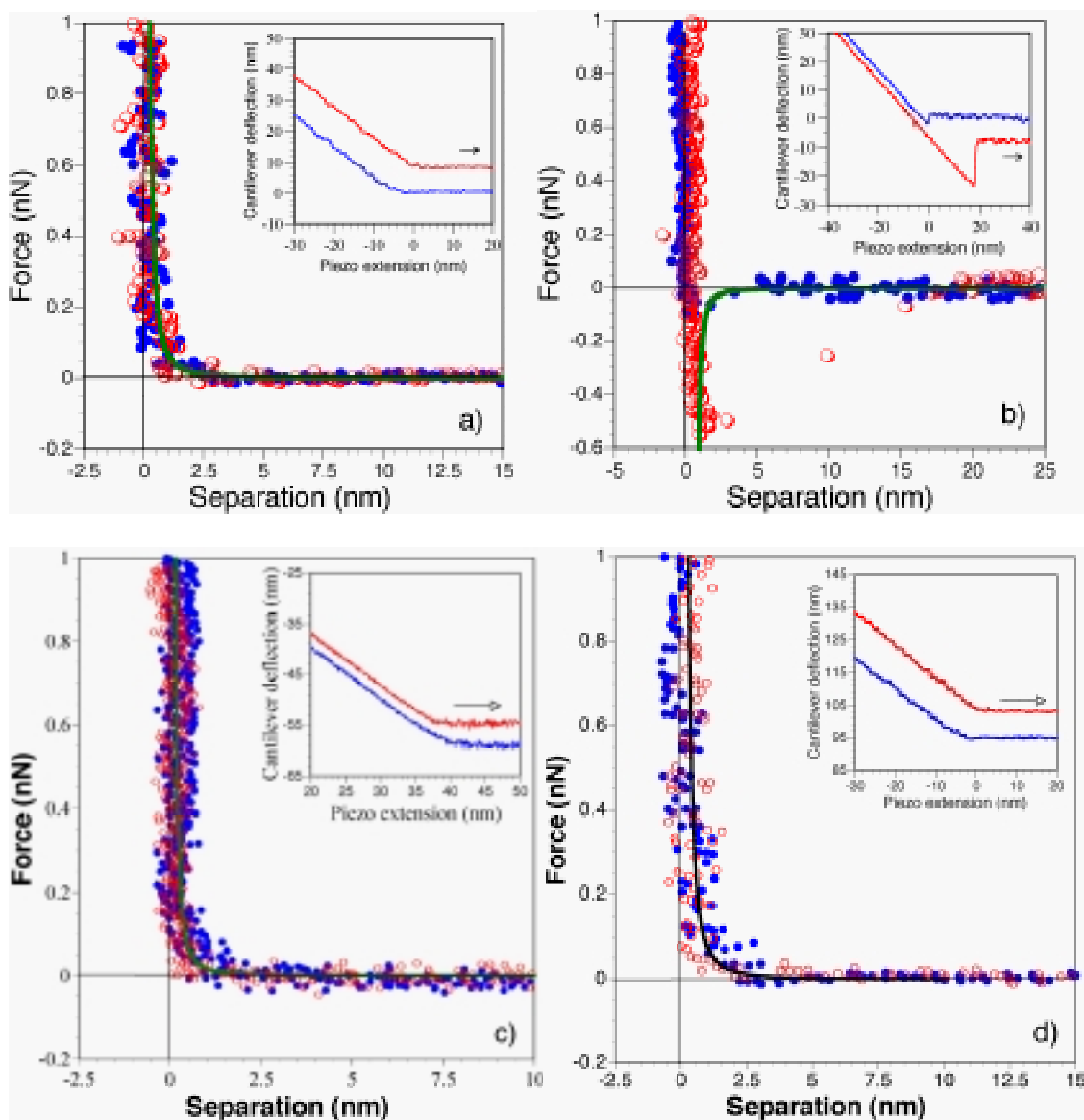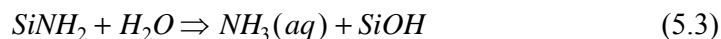
Fig. 5.2 Force-distance curves for (a) silicon nitride/diiodomethane/silica (b) silicon nitride/diiodomethane/ silicon nitride (c) SiO$_2$/1-bromonaphtalene/silicon nitride and (d) SiO$_2$/diiodomethane/silicon nitride. An oxidised Si-wafer was used as SiO$_2$ surface in (c) and (d). The line represents theoretical calculation, filled circles approach data and open circle retraction data.

5.1 Silicon nitride surface chemistry

Thermodynamic calculations from free energy data show that silicon nitride is unstable in both air and water. An oxidised surface film will inevitably form, leading to a compositional gradient from stoichiometrical silicon nitride (Si$_3$N$_4$) to silicon oxynitride (Si$_2$N$_2$O) and silica (SiO$_2$).[133,134] The oxidised surface film is removable by etching in hydrofluoric acid (HF) or by leaching in aqueous solutions. Dissolution of silica increases with pH due to the presence of catalytic hydroxyl ions (OH⁻). Depending on the degree of oxidation, the iep will vary

considerably; a thick oxide film shifts the iep towards pH 3, whereas a freshly treated silicon nitride surface iep can be as high as pH 9.

The chemical reactions in aqueous solutions also show that ammonia is released during leaching. The most probable hydrolysis reaction sequence is

$$Si_3N + H_2O \Rightarrow Si_2NH + SiOH \qquad (5.1)$$

$$Si_2NH + H_2O \Rightarrow SiNH_2 + SiOH \qquad (5.2)$$

$$SiNH_2 + H_2O \Rightarrow NH_3(aq) + SiOH \qquad (5.3)$$

Silazane, or primary silylamine groups ($SiNH_2$), are rapidly hydrolysed to secondary amine groups (Si_2NH). If reaction (5.3) is not completely driven to the right the isoelectric point will be determined by the relative amounts of basic silylamine and acidic, amphoteric silanol ($SiOH$) groups. Depending on the pH, the surface charge will be positive, net zero (zwitterionic) or negative.

Table 5.1 shows data from ESCA measurements for various silicon nitride surfaces where the atomic ratios N/Si and O/Si have been determined and correlated to isoelectric points extracted from surface force measurements. There is a substantial difference between the three silicon nitride surfaces investigated. The AFM cantilever chip was contaminated as received with a carbon-rich film, probably originating from the mask during the chemical vapour deposition (CVD) process. However, the packaging material was recently shown to coat the tips with silicon oil, and could be a universal source of contamination.[135]

Table 5.1 Surface functional group atomic ratios and isoelectric point for three different silicon nitride surfaces. The isoelectric points were determined from AFM force measurements, except nitrided SiO_2 where also electrokinetic measurements were performed.

Surface	Source	Surface treatment	N/Si	O/Si	pH$_{iep}$
CVD chip*	DI, USA	Untreated	0.73	0.55	N/A
CVD chip*	DI, USA	Plasma[1]	1.12	1.01	-
CVD chip*	DI, USA	Plasma[2]	1.23	0.82	4.5
CVD chip*	DI, USA	Heat treated[3]	0.92	1.23	-
CVD chip*	DI, USA	Etched 5 min in 10% HF	-	-	4.5-6
CVD chip*	DI, USA	Etched 3 h in 10% HF	0.96	0.34	9
CVD wafer	SilicaTek, USA	Untreated	1.10	0.41	4.7
CVD wafer	SilicaTek, USA	Leached 24 h at pH 11	-	-	4.8
CVD wafer	SilicaTek, USA	Etched 2 min in 40% HF	-	-	9
Nitrided SiO_2[#]	Sandvik[‡]	Untreated	1.00	1.06	4.0-4.5

*AFM cantilever chip. Untreated surface consists of an unknown carbon-rich film.
[1] Plasma 500 W for 30 seconds.
[2] Plasma 1000 W for 1 minute.
[3] 300° C for 12 hours.
[#] SiO_2-spheres were obtained from Bangs Laboratories (Fishers, IN, USA).
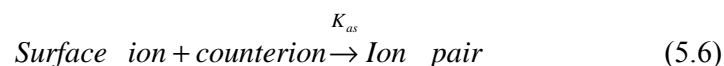[‡] Spheres were nitrided in ammonia for 4 days at 1000° C.

A similar CVD-coated wafer from SilicaTek (Tempe, AZ, USA) proved to be the most silicon nitride-like surface upon receipt. Finally, a silica sphere nitrided in ammonia was investigated after four days of nitridation (see **Paper VII**). A comparison of the atomic ratios of O and Si reveals that the relatively low amount of O for untreated surfaces is enough for shifting the isoelectric point close to that of silica. Plasma treatment removes organic content, albeit via oxidising the surface. Etching in hydrofluoric acid (HF) has a profound effect on the surface chemistry. The reduced O/Si ratio in the ESCA spectrum proves that diluted hydrofluoric acid solutions can be used for controlling the relative amounts of surface groups and the isoelectric point of a silicon nitride surface.

5.3 Charge regulated double layer interactions

Theoretical treatment of force measurements in aqueous electrolyte solutions requires a solution to the Poisson-Boltzmann equation. Linearised solutions only hold for low to moderate surface potentials and low ionic concentrations. The Guoy-Chapman model assumes that one or both surfaces maintain constant charge or constant potential during the interaction, even at a high degree of double layer overlap. A more realistic and thermodynamically substantiated model is charge regulation, where the specific chemistry of the interacting surfaces determines surface potential, surface charge and density of surface groups.

Charge regulation applied to AFM force versus distance data evaluated numerically gives surface composition, charge and potential for surfaces following the regulated boundary conditions. Since the surface chemistry of silicon nitride and silica is well known, a simple model relating site densities of ionisable surface groups to the isoelectric point has been established.[134] Altering the composition of the oxidised surface film shifts the isoelectric point of silicon nitride over a wide pH range.

The charge regulation model employed for silicon nitride has been described elsewhere and is based on the reaction set[31,136]

$$Si_2NH + H^+ \xrightarrow{K_p} Si_2NH_2^+ \tag{5.4}$$

$$SiOH \xrightarrow{K_d} SiO^- + H^+ \tag{5.5}$$

$$Surface\ ion + counterion \xrightarrow{K_{as}} Ion\ pair \tag{5.6}$$

with the potential dependent effective equilibrium constants given by

$$K_i = K_i^0 \exp(-u_s \sum_j \upsilon_{ij} z_j) \tag{5.7}$$

where K_i^0 is the intrinsic equilibrium constant characterising the ith equilibrium at zero potential, u_s is the dimensionless surface potential, and υ_{ij} and z_j are the stoichiometric

coefficient and the charge number of the jth component of the ith reaction, respectively. For a hydroxylated silica surface, Eq. (5.4) should be replaced by

$$SiOH + H^+ \xrightarrow{K_p} SiOH_2^+ \tag{5.8}$$

A mass balance of Eq. (5.4-5.6) provides the connection between surface charge density and ionisable surface groups via

$$\sigma = eN_A \left(\left\{ Si_2NH_2^+ \right\} - \left\{ SiO^- \right\} \right) \tag{5.9}$$

where e is the elementary charge and N_A Avogadro's number.

The charge regulation model enters the solution of the Poisson-Boltzmann equation for the electric double-layer in

$$\begin{cases} \dfrac{d^2u}{dx^2} = \sinh u, \quad \left. \dfrac{du}{dx} \right|_{x=0} = 0 \\[2ex] \sigma = \dfrac{2en}{\kappa} \int\limits_{0}^{\kappa H/2} \sinh u \, dx \end{cases} \tag{5.10}$$

where the potential distribution is described relative to the middle-plane potential u_0.
The total interaction force, including a van der Waals force between plane-parallel surfaces, is calculated from the Derjaguin approximation as

$$F(H) = \frac{4\pi R}{\kappa} \int\limits_{\kappa H/2}^{\infty} p \, dx \tag{5.11}$$

where the electrostatic pressure, p, is $p=2nk_BT(\cosh u_0 -1)$.

The solution to these sets of equations has been evaluated with a computational procedure based on two nested iteration cycles. Force measurements between two etched and two plasma treated silicon nitride surfaces consisting of a tip and a flat substrate of the same chemical composition were conducted in an aqueous electrolyte solution in the pH range 3-11 (**Paper II**). The silica system consisted of a glass sphere attached to a tipless cantilever and an oxidised silica plate. From the experimental force curves, a number of measurement points are chosen and organised in triplets as force-separation-pH. These points serve as the basis for obtaining surface ionisation parameters, which are evaluated by minimisation of the deviation between the experimental and calculated force curves. Fixed values were assigned to the association constant and the Hamaker constant. Site densities and protonation constants of the Si_2NH and $SiOH$ groups, and the tip radius were used as fitting parameters and assigned relevant starting values.

Experimental force curves are shown in Fig. (5.3) for plasma cleaned silicon nitride surfaces. The force is purely attractive at pH 3.5 but an increasing repulsion is seen at successively higher pH. The van der Waals force is completely overcome by electrostatic repulsion above
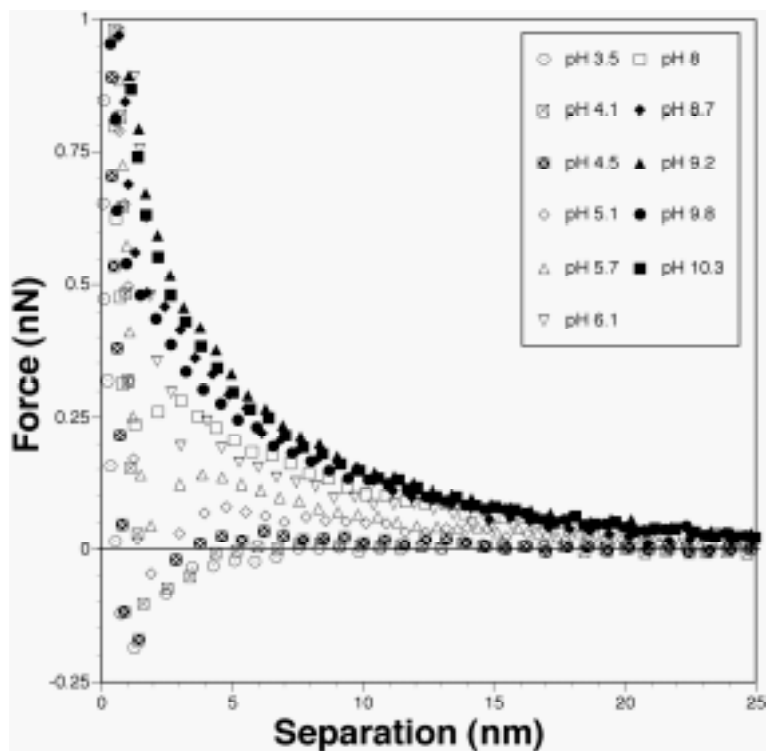
Fig. 5.3 Force measurement as a function of separation and pH in 1 mM KCl between two
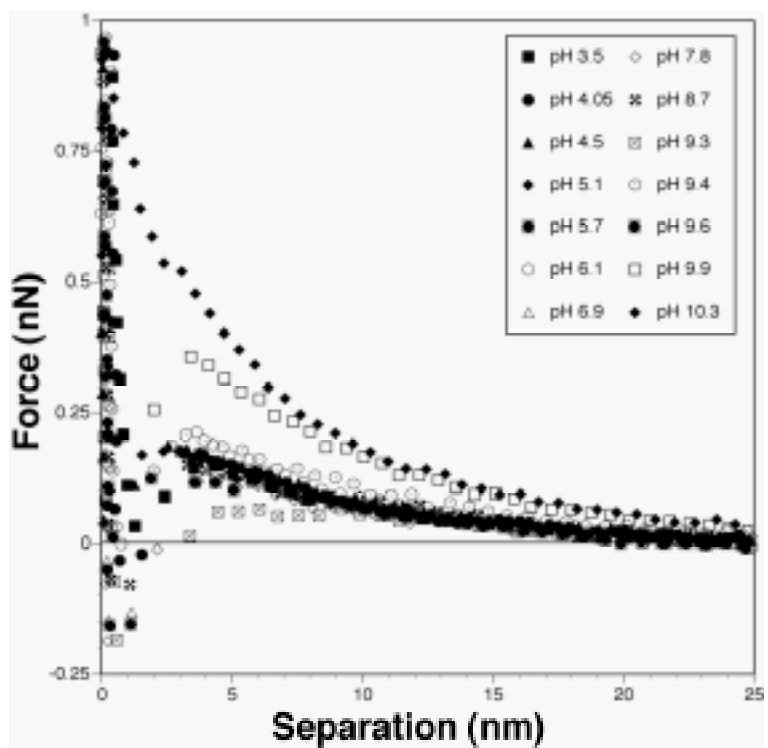identical, amorphous, plasma cleaned silicon nitride surfaces.

Fig. 5.4 Force measurement as a function of separation and pH in 1 mM KCl between two
identical, amorphous, etched silicon nitride surfaces.

pH 9. The low isoelectric point indicates that the surfaces are heavily oxidised. Force curves between etched silicon nitride surfaces (Fig. 5.4) show that the isoelectric point has been shifted to a much higher pH due to a decrease in silanol group density and exposal of the actual nitride surface.

The tip/pyramid geometry discussion above for short-ranged van der Waals forces implies that force measurements with a pyramid could be erroneous for longer ranged electrostatic forces. Drummond and Senden[113,114] have overcome this problem by ascribing the tip geometry to a large-scale curvature with a clearly defined radius of typically 200 nm. The effective radius was calculated from DLVO-theory using a constant potential obtained from surfactant coated silica surfaces. This effective long-range radius is certain to fail in describing the interaction at close separations but proves reliable for investigation of double layer forces. The same procedure was adopted in the silicon nitride measurements presented here by using the radius as a fitting parameter, and the computed value is to be seen as an effective radius rather than the actual tip end curvature.

Fitting experimental force curves to DLVO-theory using the boundary conditions of constant charge or constant potential yields values of charge and potential that are independent of separation distance. The numerical procedure employed here computes the distance dependence of both surface charge and surface potential. Fig. (5.5) shows potential and charge density for both silicon nitride systems and the silica system at an intersurface distance of 1 nm. Note how the isoelectric point for plasma treated silicon nitride surfaces is closer to silica than to etched silicon nitride, with similar charge densities at low pH. In addition, the density of surface groups can be derived from the fitting procedure via the mass action law and mass balance conditions.
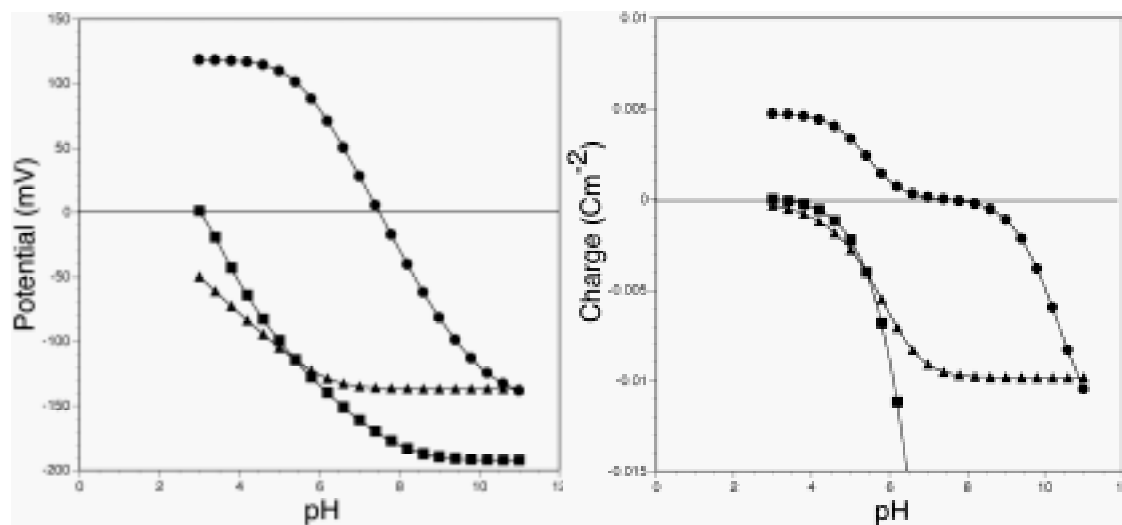

Fig. 5.5 Potential (left) and charge density (right) as a function of pH for plasma treated silicon nitride (B), etched silicon nitride (J) and silica (H). Both potential and charge are distance dependent; the results shown here have been numerically obtained at a surface separation of 1 nm. The plasma treated surface charge density saturates at -0.13 C m^{-2} (one charge per 1.2 nm^2) at high pH.

Densities of the surface species for the etched silicon nitride system are shown in Fig. (5.6). Here the isoelectric point (or the point of zero charge) can be seen at the intersection of $Si_2NH_2^+$ and SiO^- density plots. Another observation at extreme pH and small separations, is the formation of ion pairs between surface groups and electrolyte ions in solution.

The novel procedure adapted here to obtain surface composition, potential and charge information from AFM force measurements – evaluated with a numerical computation using charge regulation – has some interesting applications. First, it can be used as a complementary technique to pH-potentiometric titration for surface charge determination. Second, the results reflect the actual surfaces and can be used for simulation of force profiles and colloidal stability.
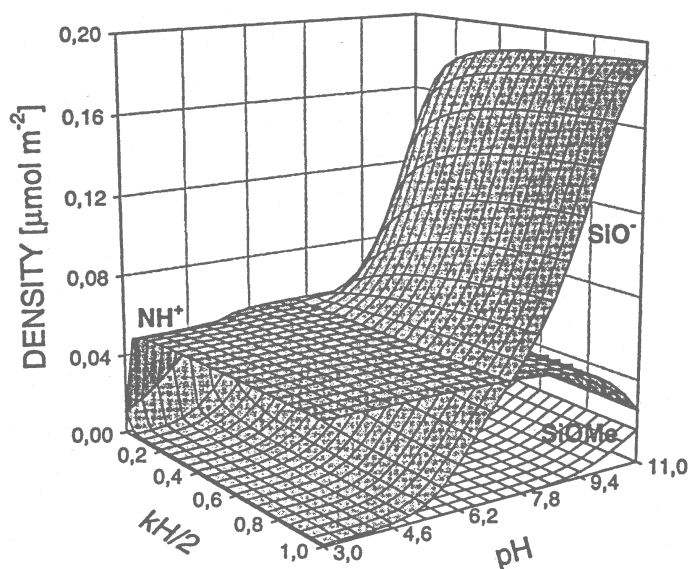

Fig. 5.6 Surface species composition of an etched silicon nitride surface, measured in 1 mM NaCl.

5.4 Colloidal probe interactions

The small contact area experienced in AFM surface force measurements where a pyramidal tip is being used results in pressures of several atmospheres. This limits the use of tip-substrate force measurements to systems that can endure such high contact pressures.

In order to overcome these drawbacks, a novel silicon nitride probe produced by Dr. Joseph Yanez at AB Sandvik Coromant has been introduced (see **Paper VII**). The probe is based on nitridation of uniform silica microspheres (Bangs Laboratories, IN, USA) in ammonia at temperatures up to 1000 °C. At intermediate temperatures, primary amine groups are formed from the interaction between ammonia and surface silanol groups.[137] Higher temperatures promote the formation of amine groups, eventually generating a nitride surface through condensation reactions. ESCA-analysis proved the surface to have a high N/Si ratio (see Table 5.1). Results from electrokinetic measurements of the nitrided spheres resulted in an isoelectric point in the pH range 4–4.5.
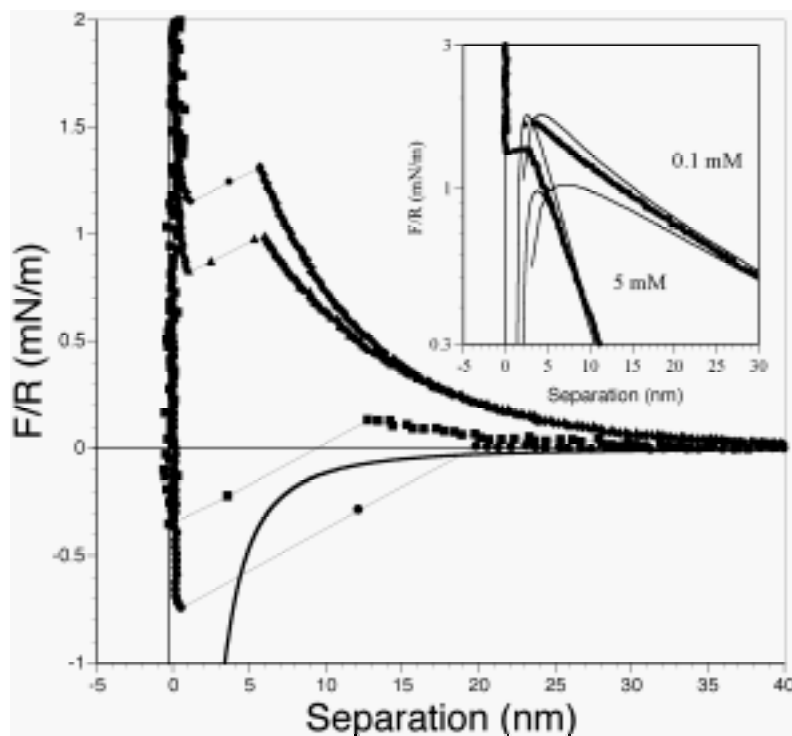
Fig. 5.7   Normalised forces measured between a Si_3N_4 colloidal probe and a Si_3N_4 flat surface in 1 mM NaCl at pH 3.5 (B), 4.1 (J), 4.9 (H) and 5.5 (F). The thick line is the expected van der Waals-force, whereas the thin lines are meant to guide the eyes. The inset shows a semilogarithmic plot of measurements at pH 8.5 for 0.1 mM and 5 mM NaCl. Lines in the inset are fits to DLVO-theory with constant charge and constant potential boundary conditions. The fitted potentials are $|\psi_0|$=90 mV and $|\psi_0|$=50 mV at low and high electrolyte concentrations, respectively.

Fig. (5.7) shows normalised force measurements of the nitrided probe against a silicon nitride wafer at different pH values and electrolyte concentrations. A purely attractive region is detected in the pH range 4.1-4.5. The thick line is the expected van der Waals force; it is clearly too short ranged to account for the attraction. The zwitterionic nature of silicon nitride, and the mismatch in isoelectric point of the probe and the surface, indicates that an attractive electrostatic force is present between pH 4.1 and 4.5. Measurements at all other pH values up to 8.5 resulted in a long ranged electrostatic repulsion followed by an attractive van der Waals force. The inset shows curves taken at two different electrolyte concentrations at pH 8.5. The lines are fits to DLVO-theory with constant charge and constant potential boundary conditions. The decay length and jump to contact agree well with the expected behaviour. Extracted surface potentials from fits to DLVO-theory, assumed to be identical for both surfaces, correlate well with previously reported values for silicon nitride.[134] However, the tendency of a decreasing surface potential with increasing ionic strength indicates that specific ion-pair formation of surface groups and counterions is different for silanol and silylamine groups, indicative of a charge regulated interaction mechanism (see **Paper II**).
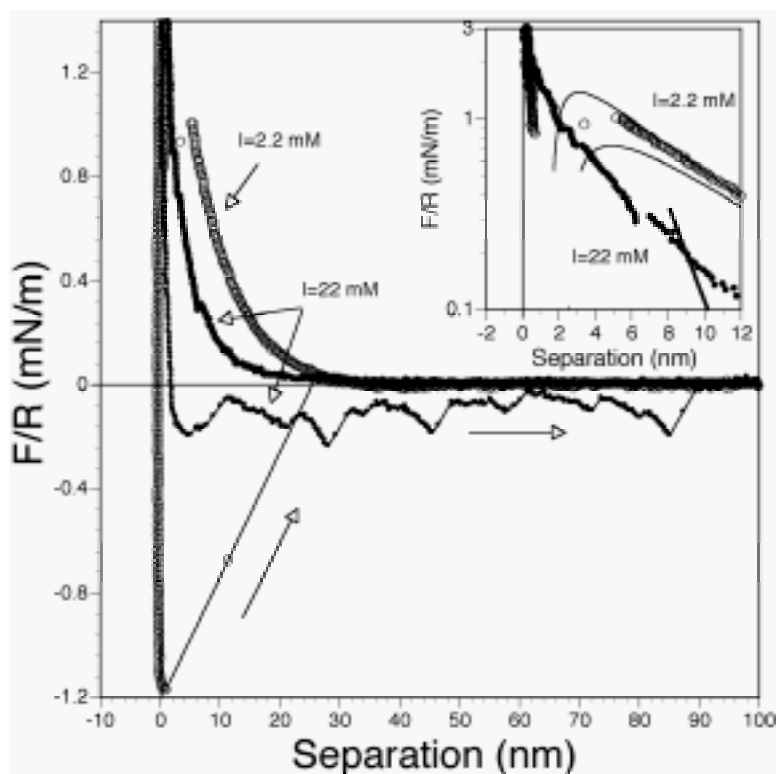
53

Fig. 5.8   Comparison of force measurement cycles of compression and decompression in 500 ppm PAA-50000 solution containing $0.1 \times 10^{-3} M$ YCl$_3$ at pH 5.5. The total ionic strength, is $I=2.2 \times 10^{-2} M$ (■) and $I=2.2 \times 10^{-3} M$ (●). The inset shows the compression curves on a semilogarithmic scale with fits to DLVO-theory.

Force measurements have also been performed in the presence of poly(acrylic acid) (PAA). PAA is a thoroughly investigated anionic polyelectrolyte that has proven useful in stabilising silicon nitride,[138] zirconia,[139-141] titania,[142] and alumina[143] systems.

Fig. (5.8) shows two measurement cycles of compression and decompression taken in two Y^{3+}-PAA solutions of different total ionic strengths (I). The PAA layer thickness is found to be less than 1 nm when adsorbed from a solution of I=2.2 mM. Measurements performed at the higher ionic strength I=22 mM give a total layer thickness of 3 nm, leading to a short ranged steric repulsion. Adsorption of PAA is promoted at higher ionic strengths by screening of the repulsive electrostatic interaction between the negatively charged polyelectrolyte and the weakly negatively charged substrate (pH>pH$_{iep}$). The effect on the steric interaction range is, however, minor. Specific surface–segment interactions leads to an essentially flat polymer conformation at the surface.

The decompression curves in Fig. (5.8) indicate a large detachment force at the higher total ionic strength, but a strong, short ranged adhesive force at the lower ionic strength. This behaviour is strongly affected by addition of multivalent cations and PAA complex formation.[144]

6. FRICTION FORCE MEASUREMENTS

The field of nanotribology has developed rapidly with the emergence of friction force microscopy (FFM).[145] A growing awareness of the importance of nanoscale properties is likely to attract interest in FFM from a wide range of disciplines. The versatility in choice of probe and environment is unmatched. Despite this fact, until now there has been a limited interest in using colloidal probes for friction force measurements[81] and experimental findings have been reported mainly for chemically modified tips.[107] Cantilevers used for force spectroscopy may not be suitable for FFM due to non-linear bending, resulting in unrealistically large coupling between vertical and lateral signals.[*] However, custom-made cantilevers are now being offered for every field of scanning probe microscopy. In conjunction with the progress in lateral force calibration methods, we are about to witness a boost similar to that of the colloidal probe technique in force spectroscopy, half a decade ago.

6.1 Iron friction in powder compaction

Friction is a gigantic problem in powder compaction. During the initial filling of powder in the die, flowability properties influence the maximum packing density. As the pressure is applied, the number of neighbouring particles touching each other increases, and the normal stress in the contact points increase leading to an increased frictional resistance. Wear occurs against the die-wall and the upper and lower punch during the whole pressing process. Organic additives are often used as lubricating agents to increase the flowability during forming and as binders for improving green strength of the compact. An optimised powder-to-lubricant ratio must be found in order to minimise clogging in the feed system and wear during and after compaction.

In **Paper III** we study the influence of lubrication on the micromechanical properties of iron particles sliding on a polished iron sample. There are several advantages of using FFM for this purpose. First, using a particle of the actual powder to be pressed, as the probe, makes the measurements very relevant for understanding the pressing properties better. Second, particle interactions can be studied at a relevant length scale, both normally and laterally. Finally, inserting the results in an appropriate model can give the stiffness (force per unit displacement) and contact dynamics during shearing of adsorbed lubricant films.

The relative strength of the cantilever and materials determines whether stiffness properties can be extracted from normal or lateral force measurements. Johnson gives the normal stiffness, k_{zc}, for a sphere in contact with a flat surface as[86]

$$k_{zc} = 2E^* a \tag{6.1}$$

and the lateral stiffness, k_c, as

$$k_c = 8G^* a \tag{6.2}$$

---

[*] This is particularly true for large colloidal probes and V-shaped cantilevers.

where a is the contact radius, E^* is the combined Young's modulus ($3/4 \cdot K$, see Eq. 5.5) and $G^* = E^*/2(1+v)$ is the combined shear modulus. The cantilever normal stiffness is typically 0.01-1 N/m, whereas the lateral stiffness of the cantilever is three or four orders of magnitude higher.[66] Many materials have a stiffness of this order, rendering lateral measurements ideal for determination of contact stiffness variations.[146-148] In such cases a model of springs in series yields

$$k_{tot} = \left(\frac{1}{k_c} + \frac{1}{k_{lever}} \right)^{-1} \tag{6.3}$$

where k_{lever} is the cantilever lateral spring constant, and k_{tot} is the total stiffness of the system as evaluated from the slope of the static friction force in a friction loop. Simultaneous measurement of friction and stiffness in cycles of loading and unloading therefore gives a thorough understanding of the system's shearing behaviour.

Measurements of friction force and stiffness against applied load is seen in Fig. (6.1) for an iron probe sliding on a polished iron substrate in the presence and absence of lubricants. The loading and unloading curves for bare surfaces in air display a small hysteresis and have a friction coefficient of approximately 0.5. When surfaces are coated with EBS (wax) and zinc stearate (ZS), the friction coefficient is significantly reduced. Considerable hysteresis, however, is apparent between the loading and unloading curves. The origin of the hysteresis can be explained from the stiffness dependence on load. Coated surfaces exhibit hysteresis in both friction and stiffness measurements. In contrast, the total stiffness for bare iron surfaces asymptotically reaches the value for the lateral spring constant, 19.8 N/m. This is predicted from Eq. (6.3) since the iron stiffness is much higher than the cantilever stiffness. Consequently, at high applied loads all deformation is taken up by the cantilever. As loading and unloading curves overlap only elastic deformation has occurred.
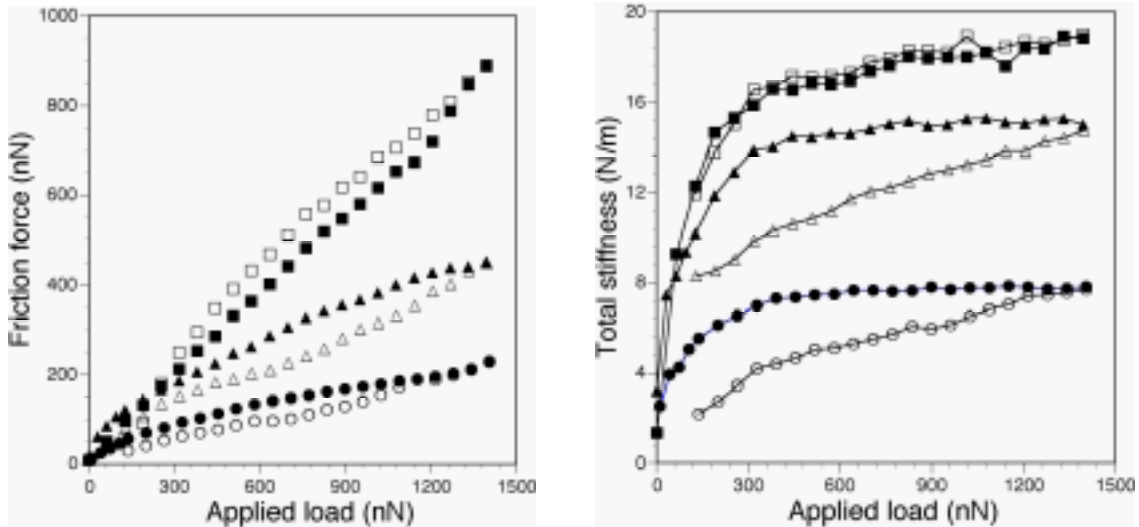

Fig. 6.1 _Left:_ Friction-load measurements on Fe-Fe (■), Fe-EBS-Fe (Δ) and Fe-ZS-Fe (●). _Right:_ Total system stiffness measurements. Filled symbol denotes unloading curve.

The ZS coated surfaces exhibit an increase in the total stiffness at increasing applied load. The stiffness finally reaches a plateau at high applied loads; this is equivalent to the shear strength of the contact. The hysteresis between the loading and unloading curves indicates that a non-elastic deformation has occurred. The EBS and ZS coated surfaces only reach 73 % and 35 %, respectively, of the cantilever stiffness which is explained by energy dissipation and surface layer deformation in the contact zone. The binder may also undergo conformational (viscoelastic) changes, or simply melt, which could explain why the unloading friction curve yields higher friction forces than the loading curve.

The stiffness hysteresis implies that elastic contact mechanics models do not apply for the lubricated surfaces. Note that this conclusion could not have been drawn from the unloading curve alone; friction measurements tend to be displayed using data from decreasing loads, which may not be eligible if further quantification is intended.

6.2 Granule friction in powder compaction

Reducing friction in granulated ceramic powder compaction is of major concern in terms of the uniformity and density of the final component (*cf.* Chapter 1). Direct measurements of granule friction are scarce. Current methods are based mainly on examination of the ejection pressure,[149] calculation from shear strength measurements[150,151] or studies of tap density and apparent density ratios.[152] Other methods such as angle of repose and flowability do not describe the granule sliding behaviour under an applied load.

The frictional characteristics depend to a large extent on the concentration of binder. The binder can migrate to the surface during spray drying, particularly if it is water-soluble.[153,154] The hygroscopic nature of certain binders affects the granule surface properties. An increased softening occurs at higher humidity, leading to considerable difficulties in granule handling during certain periods of the year[155] because of stickiness and low flowability.

Paper VI describes how FFM can be successfully used in powder technology for direct evaluation of friction coefficients and the adhesion force between individual granules. Silicon nitride granules of different binder concentration produced from a colloidally stable suspension were investigated with friction measurements as a function of humidity and applied load. The binder consisted of poly(ethylene glycol), PEG, of mixed molecular weights. The measurements were performed between a single granule and a polished, hard metal substrate, and between two granules. The measurements relate to internal (granule-granule) and external (granule-wall) friction in a compaction process. Additionally, the granules were characterised using conventional methods, *e.g.* flowability and angle of repose.

Results from granule–substrate measurements at the intermediate relative humidity of 45% are shown in Fig. (6.2). At this humidity the friction-load curves show clear trends and are mutually shifted with respect to friction force. Evaluation of the coefficient of friction reveals that it becomes higher for granules of lower PEG content. These granules exhibit a rougher contact with less lubricating aid from the binder. Hence, Amonton's law describes the
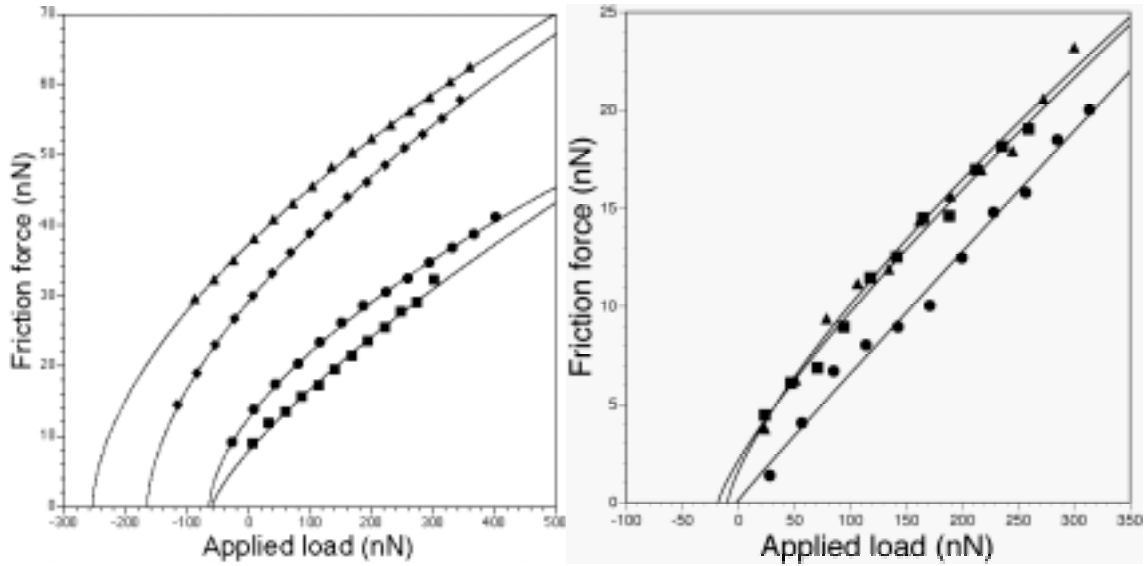
Fig. 6.2 Friction measurements at 45% RH between a granule and a hard metal substrate (left), and between two granules at 38 % RH (right). The binder concentration is 0.81% (B), 1.62% (J), 3.25% (H) and 6.5% (F). The curves are fits to Eq. (3.5).

friction-load dependence very well. At successively higher PEG concentration, the curves become more non-linear, followed by an increase in adhesion force. The data is fitted to Eq. (3.5), where a higher load index for granules of low binder content is equivalent to a rougher contact with a progressively lesser impact of deformation on the sliding friction behaviour.

Also shown in Fig. (6.2) are friction measurements between two individual granules at a relative humidity of 38%. Fitting these data to the same equation as above reveals a load index almost conforming to unity. Hence, these results closely follow Amonton's law.

Friction coefficients and adhesion forces as a function of humidity and PEG-concentration are summarised in Figs. (6.3-6.4), where equivalent properties for granule-granule measurements at low humidity are also indicated. Higher humidity softened the granules too much for a granule-granule contact to be stable. Note that the coefficient of friction is higher for substrate measurements, regardless of the binder content, implying that granule-wall friction dominates the pressing response at low humidity.

Granule strength is highly dependent on the binder properties. The softening effect of granules containing acrylic binders at high humidity has been related to a decrease in binder glass transition temperature (T_g).[156] The T_g of PEG is, however, rather non-sensitive to humidity, although the uptake of water is substantial.[157] The reduction in granule surface hardness, and related increase in the adhesion force, with increasing humidity is probably related to a decrease in PEG shear modulus.
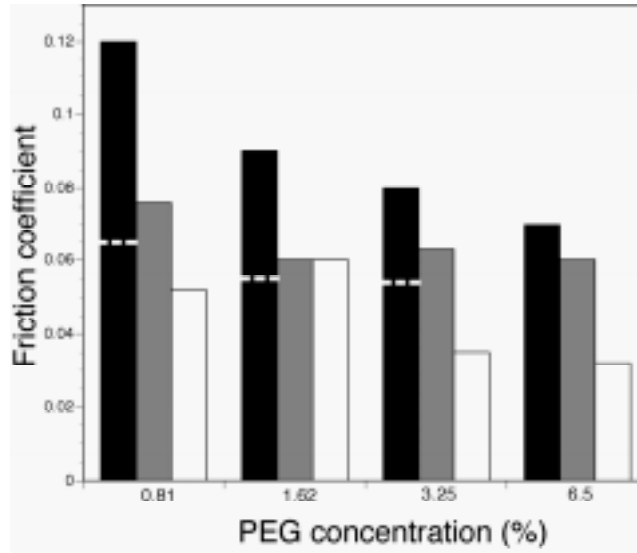
Fig. 6.3 Summary of friction coefficients from granule-substrate measurements. Columns indicate measurements done at 38% RH (black), 45% RH (grey) and 60% RH (white). The bold white lines at 38% RH represents results for granule-granule measurements.
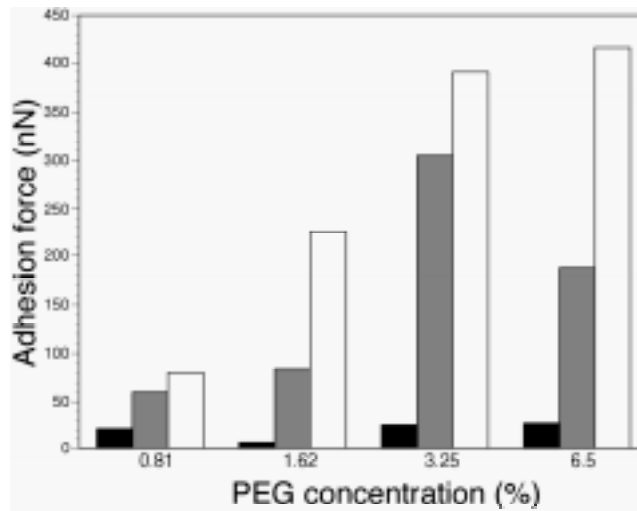

Fig. 6.4 Summary of adhesion forces from granule-substrate measurements. Columns indicate measurements done at 38% RH (black), 45% RH (grey) and 60% RH (white). In comparison, granule-granule adhesion was negligible.

6.3 Microscopic stick-slip

The phenomenon known to scientists as stick-slip (door-squeaking, tooth-grinding or pig-snorting to the layman) is an unwanted frictional response industrially associated with wear and high costs. In powder compaction the ejection of the pressed part may be smooth or highly resistive depending on whether the dies are lubricated or not, see Fig. (6.5). The sliding behaviour between rough surfaces in contact may exhibit stick-slip if the stiffness of the system generates a spring force smaller than the static friction force.[158] This is equivalent to having a spring velocity smaller than the critical velocity for stick-slip, and is mainly a matter

59

of inertia effects in which a critical tangential stress deforms the contacting surfaces. Such motion becomes very irregular, with sticking times and stick-slip amplitudes of random distributions.
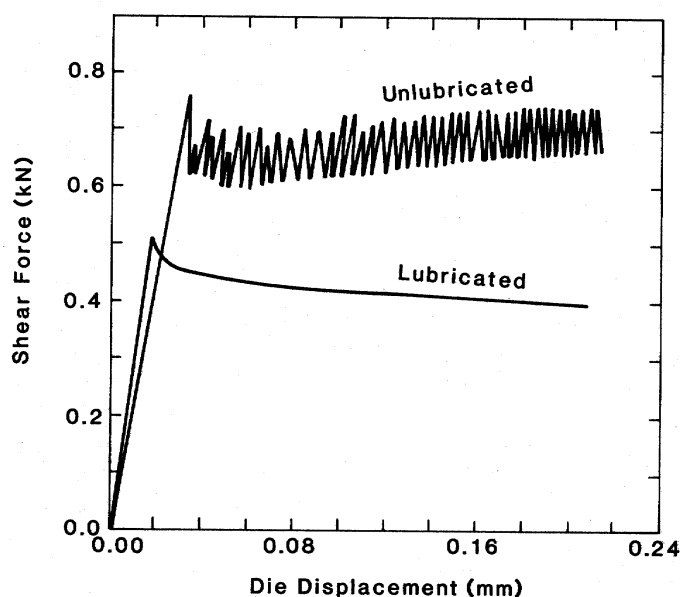

Fig. 6.5 The stress acting on a pressed component during ejection from the die. Lubrication lowers the friction and generates steady sliding instead of irregular stick-slip motion. From Reed.[159]

The only regular stick-slip motion exhibited by unlubricated surfaces detected by FFM occurs on an atomic scale. A tungsten tip sliding on graphite,[75] mica[160] and self-assembled monolayers[161] has been shown to follow the atomic corrugations in a saw-tooth like fashion. Quantitative studies on confined liquids have been studied by Israelachvili and co-workers with the SFA for a long time.[40] Shear measurements provided novel knowledge about the transition from continuum to molecular behaviour of very thin films, showing that the viscosity could be described by the bulk value down to a few molecular layers.[42,162] These films were reported to exhibit both solid-like and liquid-like properties depending on the film thickness and the molecular ordering. It is now widely believed that a confined lubricant is in an elastic, glassy state (freezing) during sticking and a more fluidised state (melting) during slip and transition to steady sliding.[163,164] Molecular dynamic simulations have confirmed both the phase transition of the interfacial material, the elastic response up to the yield point and the subsequent stick-slip motion.[165,166]

Paper V presents FFM measurements where highly regular stick-slip motion occurs over several micrometers between a colloidal silica probe and a flat silica wafer. The silica surfaces are coated with an adsorbed monolayer of 2-hydroxy stearic acid (2-HSA). The paper also presents measurements for another system, consisting of 12-hydroxy stearic acid (12-HSA) coated silica surfaces, that did not exhibit stick-slip but smooth sliding over the entire load and velocity regime studied.

The friction-load cycles for both systems are shown in Fig. (6.6). The 2-HSA case initially displays a linear increase in friction force with load, soon transforming to an exponential

behaviour. A viscoelastic relaxation mechanism may be responsible for the rapid escalation in friction force if wear can be ruled out. The hysteresis seen in the friction-load cycle and the equivalent hysteresis in the stiffness-load data indicates strong energy dissipation, clearly invalidating further quantification using elastic contact mechanics theory (*cf.* **Paper III** and above).
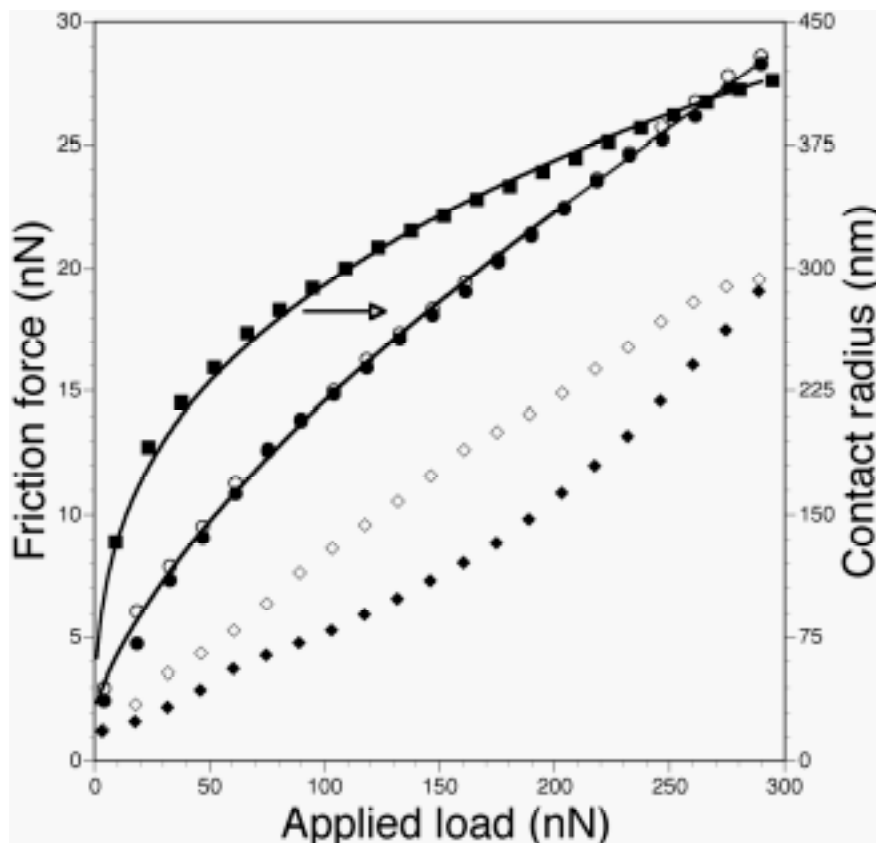

Fig. 6.6 Friction force measurement cycles on surfaces coated with 2-HSA (F, Å) and 12-HSA (J, E), and contact radius for 12-HSA (B). Filled symbols denote increasing applied load and hollow symbols decreasing applied load. The lines are fits to Maugis contact mechanics theory.

Changing the surface coating from 2-HSA to 12-HSA results in a totally different friction behaviour. The loading and unloading friction and stiffness data overlap with minimal hysteresis over the same loading range, thus validating the friction dependence on contact area. Carpick *et al* have formulated a generalised procedure for obtaining the Maugis parameter, λ, from friction-load data.[167] This fit, shown in Fig. (6.6), reveals that λ is between the values associated with DMT and JKR theories. Subsequent calculation of contact radius using fitting parameters adapted from the friction-load data is also shown in Fig. (6.6). Assuming a circular contact area yields a highest applied pressure of 500 kPa and an estimated value of the combined shear modulus, G^*, of approximately 20 kPa. The value of G^* is about three orders of magnitude lower than that estimated from materials properties of the contacting silica surfaces. Hence, the shearing properties are controlled by the stearic acid layers and not the underlying surfaces.

61

Friction loops obtained for the 2-HSA coating displayed a static friction region ending in a yield point, acting as a transition energy barrier prior to steady sliding. Jang and Tichy have correlated the static friction to a critical shear stress governed by two relaxation times; one is responsible for the build-up of the barrier, the other determines the subsequent slow decay into steady kinetic friction.[168,169] The complete equation of motion for such a phenomenological nanorheological model indicates that the criterion for stick-slip to occur is an instability where the shear stress falls with respect to shear rate. This is equivalent of accelerated sliding when the static friction force increases faster than the cantilever spring force, *i.e.* $F_s(t) > kvt$. Stick-slip motion may thus be induced at a certain critical velocity, v_c, resulting from a transition between ordered and disordered sliding states of the thin film.[165,166]

The critical velocity invoking stick-slip motion at a certain applied load is found by continuously decreasing the sliding velocity, see Fig. (6.7). In *a* and *b*, steady sliding occurs after the yield point is reached. A discontinuous transition induces probe slippage in *c*. Small kinetic friction force fluctuations indicate that the critical velocity is almost attained. Further lowering of the velocity induces regular stick-slip motion, which is commonly related to a transition of the molecular state during a stick-slip period from glassy to a more fluidised order. Batista and Carlson[170] compare the change of ordering to a state variable, θ, where $\theta = 0$ corresponds to a fluidised film at high sliding velocities, and $\theta = 1$ to a solid-like, glassy film at low velocities. This state variable depends on time according to

$$\theta = \frac{\theta_0}{\theta_0 + (1 - \theta_0)e^{-t/\tau}} \tag{6.4}$$

where τ is a characteristic time associated with the phase transition, and $\theta = \theta_0$ at *t=0* is given by a scaling law involving the critical velocity, a characteristic distance, and time of the interface over which melting takes place. The stick-slip periodicity may thus be modelled using

$$F(t) = F_k^{\min} + \Delta F \theta \tag{6.5}$$

where $F_k^{\min}$ is the minimum kinetic friction force and ΔF the stick-slip amplitude.

Fig. (6.8) shows an arbitrarily chosen region modelled using the above equations. The stick-slip induced at the slightly higher frequency was fitted using $\theta_0 = 0.05$, whereas the lower velocity was found to fit well using $\theta_0 = 0.35$. The latter value correlates to a more glassy character, a rapid slippage rate and a longer phase growth distance.

The stick-slip periodicity remains approximately constant at 200 nm with a threefold increase in velocity. The contact radius calculated for the case of 12-HSA is roughly equal to the stick-slip periodicity of 2-HSA at the same applied load. This means that the stick-slip motion occurs in several periodical microslips within the contact zone at high pressures.
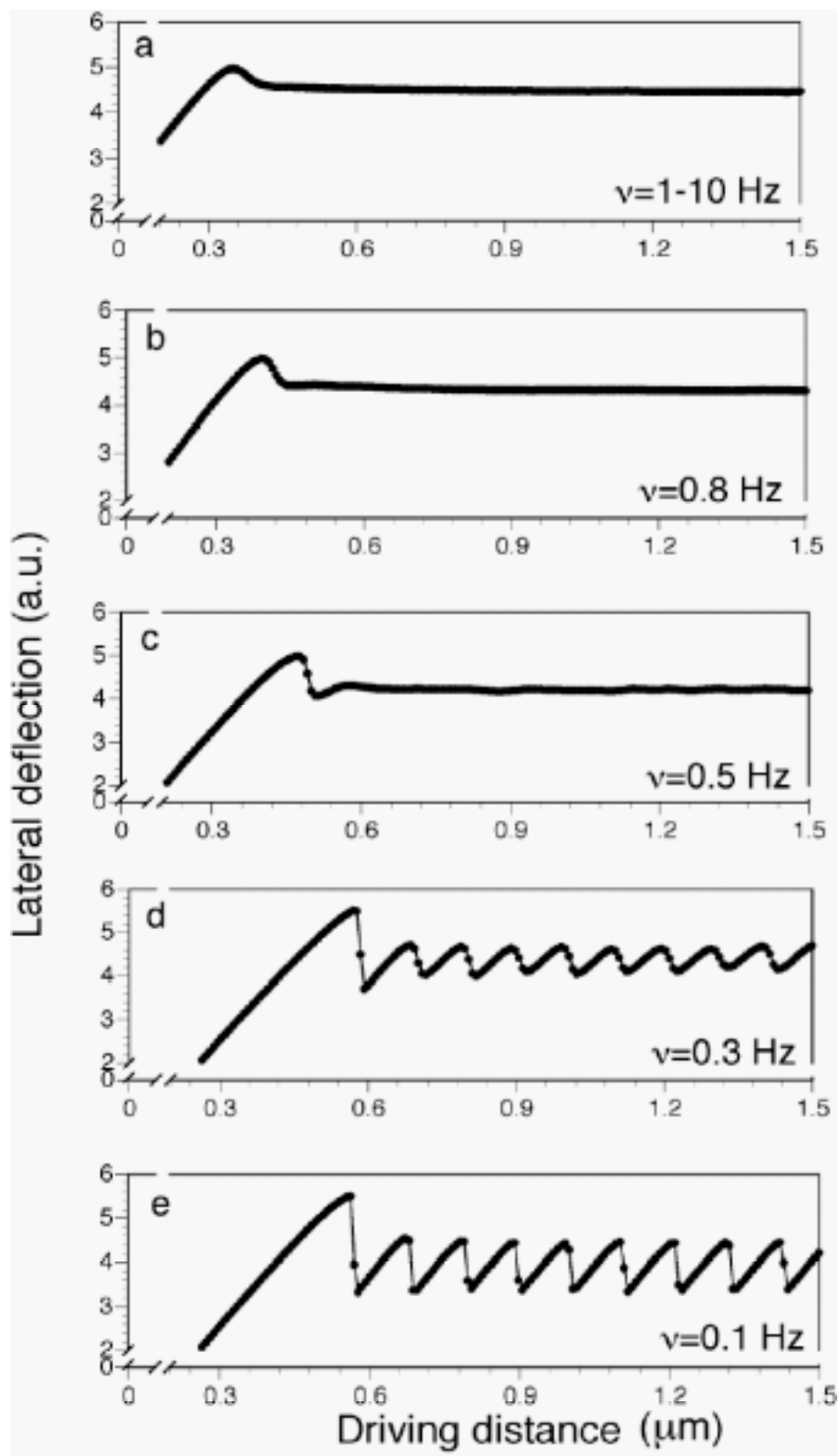
Fig. 6.7 The evolution of stick-slip motion from steady sliding when the frequency is reduced for 2-HSA coated silica surfaces. The critical sliding frequency is 0.4 Hz for this particular load.

63

Yoshizawa *et al*[171] found that the friction becomes maximum during the transition from a solidlike to a liquidlike state of the confined lubricant. Consequently, whether stick-slip motion will occur is in every sense a function of monolayer relaxation times in relation to sliding velocity and how much the associated Deborah number deviates from unity.
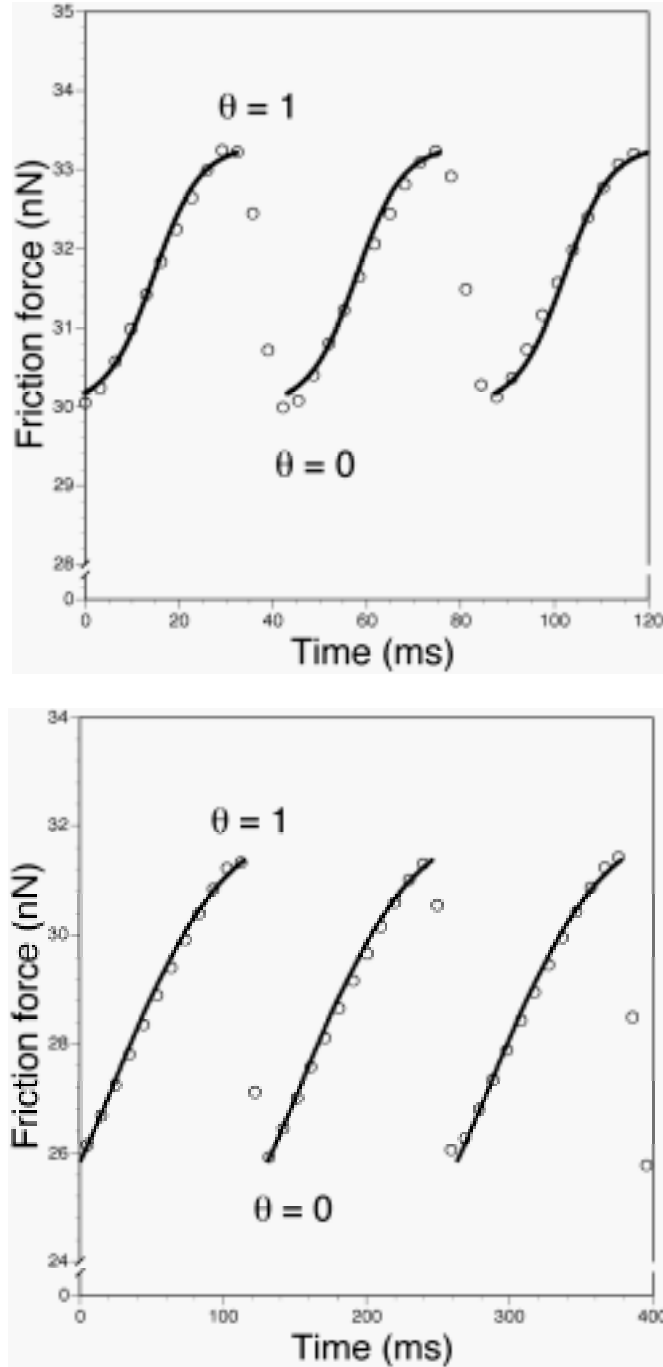

Fig. 6.8 Stick-slip motion fitted to the fluidisation state variable, θ, at a sliding frequency of 0.3 Hz (top) and 0.1 Hz (bottom). The interfacial material changes state from liquid-like (θ = 0) to solid-like (θ = 1) in repeatable cycles.

7. PROSPECTS FOR FUTURE RESEARCH

I hope that someone will be sincerely interested in the results or techniques presented in this thesis and use it for future projects. Should that be the case, I am happy to point the interested person in these directions:

Recent results by Feiler *et al*[110] suggest surface separation rather than surface chemistry controls friction. The surface separation distance in contact is partly determined by the interaction potential. It could be worth investigating the effect of a repulsive van der Waals force on the separation distance; the absence of an adhesive force component would constitute an ideal condition for studying nanoscale energy dissipation through friction forces only.

In the context of computer modelling of surface force measurements between charge regulated surfaces, it should be possible to extend the application to interactions with polyelectrolytes. This requires a substantial effort and understanding of appropriate theories, but the outcome would benefit from the numerous surface-polymer combinations possible with the colloidal probe technique.

The granule friction measurements presented here can be directly applied to other powder processing areas, *e.g.* pharmaceutical research or the cosmetics industry. Density and strength requirements of a compacted body vary considerably from one application to another; friction and adhesion studies of prospective powders or additives may provide a simple means to an optimised powder-powder contact behaviour.

The full potential of the AFM has not yet been reached regarding stick-slip measurements. Appropriate models in conjunction with carefully designed experiments can improve knowledge and test theories of such diverse areas as nanorheology and earthquake dynamics. Who knows, it may also provide new insight into the motion of the three phase line in papermaking processes?

8. REFERENCES

1. **Pugh, R. J. & Bergström, L.** "*Surface and colloid chemistry in advanced ceramics processing"* (Marcel Dekker Inc., New York, 1994).
2. **Richerson, D. W.** "*Modern ceramic engineering"* (Marcel Dekker Inc., New York, 1982).
3. **Sigmund, W. M., Bell, N. S. & Bergström, L.** "*Novel powder-processing methods for advanced ceramics*". J. Am. Ceram. Soc. **83**, 1557-1574 (2000).
4. **Özkan, N.** "*Compaction and sintering of ceramic powders*" (Imperial College of Science, Technology and Medicine, London, 1994).
5. **Lange, F. F.** "*Powder processing science and technology for increased reliability*". J. Am. Ceram. Soc. **72**, 3-15 (1989).
6. **Bergström, L.** in "*Surface and colloid chemistry in advanced ceramics processing"* 193-245 (Marcel Dekker Inc., New York, 1994).
7. **German, R. M.** "*Powder metallurgy science"* (MPIF, Princeton, 1994).
8. **Walker, W. J. & Reed, J. S.** "*Influence of slurry parameters on the characteristics of spray-dried granules*". J. Am. Ceram. Soc. **82**, 1711-1719 (1999).
9. **Schneider, S.** "*Engineered materials handbook: Ceramics and glasses"* (ASM international, 1991).
10. **Deis, T. A. & Lannutti, J. J.** "*X-ray computed tomography for evaluation of density gradient formation during the compaction of spray-dried granules*". J. Am. Ceram. Soc. **81**, 1237-1247 (1998).
11. **Sarid, D.** "*Scanning force microscopy"* (Oxford University Press, New York, 1994).
12. **Meyer, E.** "*Atomic Force Microscopy*". Progr. Surf. Sci. **41**, 3-49 (1992).
13. **Maurice, P. A.** "*Applications of atomic-force microscopy in environmental colloid and surface chemistry*". Coll. Surf. A **107**, 57-75 (1996).
14. **Meurk, A.** "*Surface force and friction measurements with an atomic force microscope*" (Royal Institute of Technology, Stockholm, 1999).
15. **Israelachvili, J. N.** "*Intermolecular and Surface Forces"* (Academic Press Inc., New York, 1992).
16. **Hamaker, H. C.** "*The London-van der Waals attraction between spherical particles*". Physica **4** (1937).
17. **Russel, W. B., Saville, D. A. & Schowalter, W. R.** "*Colloidal dispersions"* (Cambridge University Press, Cambridge, 1989).
18. **Lifshitz, E. M.** "*The theory of molecular attractive forces between solids*". Sov. Phys. JETP (Engl. Transl.) **2**, 73-83 (1956).
19. **Hough, D. B. & White, L. R.** "*The calculation of Hamaker constants from Lifshitz theory with applications to wetting phenomena*". Adv. Coll. Interface Sci, **14**, 3-29 (1980).
20. **Parsegian, V. A. & Ninham, B. W.** "*Application of the Lifshitz theory to the calculation of van der Waals forces across thin lipid films*". Nature **224**, 1197-1198 (1969).
21. **Gingell, D. & Parsegian, V. A.** "*Computation of van der Waals interactions in aqueous systems using reflectivity data*". J. Theor. Biol. **36**, 41-52 (1972).
22. **Mahanty, J. & Ninham, B. W.** "*Dispersion Forces"* (Academic Press Ltd, London, 1976).
23. **Bergström, L.** "*Hamaker constants of inorganic materials*". Adv. Coll. Interface Sci. **70**, 125-169 (1997).
24. **Hunter, R. J.** "*Introduction to Modern Colloid Science"* (Oxford University Press, Oxford, 1993).

25. **Verwey, E. G. W. & Overbeek, T. G.** "*Theory of stability of lyophobic colloids"* (Elsevier, Amsterdam, 1948).
26. **Knackstedt, M. A. & Ninham, B. W.** "*Correlations and thermodynamic coefficients in dilute asymmetric electrolyte solutions*". J. Phys. Chem. **100**, 1330-1335 (1996).
27. **Carnie, S. L., Chan, D. Y. C. & Gunning, J. S.** "*Electrical double-layer interaction between dissimilar spherical colloidal particles and between a sphere and a plate: The linearized Poisson-Boltzmann theory*". Langmuir **10**, 2993-3009 (1994).
28. **Warszynski, P. & Adamczyk, Z.** "*Calculations of double layer electrostatic interactions for the sphere/plane geometry*". J. Coll. Interface Sci **187**, 283-295 (1997).
29. **Chan, D., Perram, J. W. & White, L. R.** "*Regulation of surface potential at amphoteric surfaces during particle-particle interaction*". J. Chem. Soc. Farad. Trans. I **72**, 1046-1057 (1974).
30. **Chan, D., Healy, T. W. & White, L. R.** "*Electrical double layer interactions under regulation by surface ionization equilibria - Dissimilar amphoteric surfaces*". J. Chem. Soc. Farad. Trans. I **72**, 2844-2865 (1976).
31. **Zhmud, B. V. & Bergström, L.** in "*Surfaces of Nanoparticles and Porous Materials"* 567-592 (Marcel Dekker Inc., New York, 1998).
32. **Reiner, E. S. & Radke, C. J.** "*Double layer interactions between charge-regulated colloidal surfaces: Pair potentials for spherical particles bearing ionogenic surface groups*". Adv. Coll. Interface Sci. **47**, 59-149 (1993).
33. **Chan, D. Y. C. & Carnie, S. L.** "*Interaction free energy between plates with charge regulation: A linearized model*". J. Coll. Interface Sci. **161**, 260-264 (1993).
34. **Ettelaie, R. & Buscall, R.** "*Electrical double layer interactions for spherical charge regulating colloidal particles*". Adv. Coll. Interface Sci. **61**, 131-160 (1995).
35. **Claesson, P. C.** personal communication. (1998).
36. **Derjaguin, B. V. & Landau, L.** "*Theory of the stability of strongly charged lyophobic sols and the adhesion of strongly charged particles in solutions of electrolytes*". Acta Phys. Chim. URSS **14**, 633 (1941).
37. **Deryaguin, B. V.** "*Untersuchungen über die Reibung und Adhäsion, IV.*". Kolloid Z **69**, 155 (1934).
38. **White, L. R.** "*On the Deryaguin approximation for the interaction of macrobodies*". J. Coll. Interface Sci. **95**, 286-288 (1983).
39. **Stankovich, J. & Carnie, S. L.** "*Electrical double layer interaction between dissimilar spherical colloidal particles and between a sphere and a plate: Nonlinear Poisson-Boltzmann theory*". Langmuir **12**, 1453-1461 (1996).
40. **Meyer, E., Overney, R. M., Dransfeld, K. & Gyalog, T.** "*Nanoscience: Friction and rheology on the nanometer scale"* (World Scientific Publishing Co., Singapore, 1998).
41. **Berman, A. & Israelachvili, J.** in "*Micro/Nanotribology and its applications"* (ed. Bhushan, B.) 317-329 (Kluwer Academic Publishers, Dordrecht, 1997).
42. **Gee, M. L., McGuiggan, P. M., Israelachvili, J. N. & Homola, A. M.** "*Liquid to solidlike transitions of molecularly thin films under shear*". J. Phys. Chem. **93**, 1895-1906 (1990).
43. **Briscoe, B. J. & Tabor, F. R. S.** in "*Polymer surfaces"* (eds. Clark, D. T. & Feast, W. J.) 1-24 (John Wiley & Sons, New York, 1978).
44. **Briscoe, B. J. & Adams, M. J.** "*Tribology in particulate technology"* (Adam Hilger, Bristol, 1987).

45. **Israelachvili, J. N.** in "*Fundamentals of friction: Macroscopic and microscopic processes"* (eds. Singer, I. L. & Pollock, H. M.) 351-386 (Kluwer Academic Publishers, Dordrecht, 1992).

46. **Yoshizawa, H., Chen, Y. L. & Israelachvili, J.** "*Fundamental mechanisms of interfacial friction. 1. Relation between adhesion and friction*". J. Phys. Chem. **97**, 4128-4140 (1993).

47. **Israelachvili, J. N., Chen, Y. L. & Yoshizawa, H.** "*Relationship between adhesion and friction forces*". J. Adh. Sci. Technol. **8**, 1231-1249 (1994).

48. **Heuberger, M., Dietler, G. & Schlapbach, L.** "*Elastic deformations of tip and sample during atomic force microscope measurements*". J. Vac. Sci. Technol. B **14**, 1250-1254 (1996).

49. **Derjaguin, B. V., Müller, V. M. & Toporov, Y. P.** "*Effect of contact deformations on the adhesion of particles*". J. Coll. Interface Sci. **53**, 314-326 (1975).

50. **Johnson, K. L., Kendall, K. & Roberts, A. D.** "*Surface energy and the contact of elastic solids*". Proc. R. Soc. Lond. A. **324**, 301-313 (1971).

51. **Burnham, N. A. & Kulik, A. J.** in "*Handbook of Micro/Nanotribology"* (ed. Bhushan, B.) 247-271 (CRC Press, Boca Raton, 1999).

52. **Maugis, D.** "*Adhesion of spheres: The JKR-DMT transition using a Dugdale model*". J. Coll. Interface Sci. **150**, 243-269 (1991).

53. **Johnson, K. L.** "*Adhesion and friction between a smooth elastic spherical asperity and a plane surface*". Proc. R. Soc. Lond. A **453**, 163-179 (1997).

54. **Lin, F. & Meier, D. J.** "*Atomic-scale resolution in atomic force microscopy*". Langmuir **10**, 1660-1662 (1994).

55. **Binnig, G., Quate, C. F. & Gerber, C.** "*Atomic force microscope*". Phys. Rev. Lett. **56**, 930-933 (1986).

56. **Binnig, G. & Rohrer, H.** "*Scanning tunneling microscopy*". Physica B **127**, 37-45 (1984).

57. **Binnig, G. K.** "*Atomic-force microscopy*". Physica Scripta **T19**, 53-54 (1987).

58. **Bottomley, L. A.** "*Scanning probe microscopy*". Anal. Chem. **70**, 425R-475R (1998).

59. **Claesson, P. M., Ederth, T., Bergeron, V. & Rutland, M. W.** "*Techniques for measuring surface forces*". Adv. Coll. Interface Sci. **67**, 119-183 (1996).

60. **Ma, H., Jimenez, J. & Rajagopalan, R.** "*Brownian fluctuation spectroscopy using atomic force microscopy*". Langmuir **16**, 2254-2261 (2000).

61. **Viani, M. B., Schäffer, T. E., Chand, A., Rief, M., Gaub, H. E. & Hansma, P. K.** "*Small cantilevers for force spectroscopy of single molecules*". J. Appl. Phys. **86**, 2258-2262 (1999).

62. **Radmacher, M., Cleveland, J. P. & Hansma, P. K.** "*Improvement of thermally induced bending of cantilevers used for atomic force microscopy*". Scanning **17**, 117-121 (1995).

63. **Capella, B. & Dietler, G.** "*Force-distance curves by atomic force microscopy*". Surf. Sci. Rep. **34**, 1-104 (1999).

64. **Jarvis, S. P., Yamada, H., Yamamoto, S. I., Tokumoto, H. & Pethica, J. B.** "*Direct mechanical measurement of interatomic potentials*". Nature **384** (1996).

65. **Burnham, N. A., Colton, R. J. & Pollock, H. M.** "*Interpretation issues in force microscopy*". J. Vac. Sci. Technol. A **9**, 2548-2556 (1991).

66. **Carpick, R. W., Ogletree, D. F. & Salmeron, M.** "*Lateral stiffness: A new nanomechanical measurement for the determination of shear strengths with friction force microscopy*". Appl. Phys. Lett. **70**, 1548-1550 (1997).

67. **Burnham, N. A. & Colton, R. J.** in "*Scanning tunneling microscopy and spectroscopy: Theory, techniques and applications*" (ed. Bonnell, D. A.) 191-249 (VCH Publishers, New York, 1993).

68. **Landman, U., Luedtke, W. D., Ouyang, J. & Xia, T. K.** "*Nanotribology and the stability of nanostructures*". Jpn J. Appl. Phys. **32**, 1444-1462 (1993).

69. **Hoh, J. H. & Engel, A.** "*Friction effects on force measurements with an atomic force microscope*". Langmuir **9**, 3310-3312 (1993).

70. **Attard, P., Carambassis, A. & Rutland, M. W.** "*Dynamic surface force measurement. 2. Friction and the atomic force microscope*". Langmuir **15**, 553-563 (1999).

71. **Schillén, K., Claesson, P. M., Malmsten, M., Linse, P. & Booth, C. J.** "*Properties of poly(ethylene oxide)-poly(butylene oxide) diblock copolymers at the interface between hydrophobic surfaces and water*". J. Phys. Chem. B **101**, 4238-4252 (1997).

72. **Ducker, W. A., Senden, T. J. & Pashley, R. M.** "*Direct measurement of colloidal forces using an atomic force microscope*". Nature **353**, 239-241 (1991).

73. **Braithwaite, G.** "*Colloidal interactions measured using a modified force microscope*" (Imperial College of Science, Technology and Medicine, London, UK, 1996).

74. TiN whiskers were kindly provided by Pernilla Peterson, Stockholm University. (1998).

75. **Mate, C. M., McClelland, G. M., Erlandsson, R. & Chiang, S.** "*Atomic-scale friction of a tungsten tip on a graphite surface*". Phys. Rev. Lett. **59**, 1942-1945 (1987).

76. **Bhushan, B.** "*Handbook of micro/nanotrinology*" (CRC Press, New York, 1995).

77. **Bhushan, B.** "*Micro/Nanotribology and its applications*" (Kluwer Academic Publishers, Amsterdam, 1997).

78. **Liu, E., Blanpain, B. & Celis, J. P.** "*Calibration procedures for frictional measurements with a lateral force microscope*". Wear **192**, 141-150 (1996).

79. **Fujisawa, S., Kishi, E., Sugawara, Y. & Morita, S.** "*Lateral force curve for atomic force/lateral force microscope calibration*". Appl. Phys. Lett. **66**, 526-528 (1995).

80. **Tsukruk, V. V. & Bliznyuk, V. N.** "*Adhesive and friction forces between chemically modified silicon and silicon nitride surfaces*". Langmuir **14**, 446-455 (1998).

81. **Toikka, G., Hayes, R. A. & Ralston, J.** "*The application of lateral force microscopy to particle removal in aqueous polymer solutions*". J. Adhesion Sic Technol. **11**, 1479-1489 (1997).

82. **Putman, C., Igarashi, M. & Kaneko, R.** "*Determination of friction coefficients by friction force microscopy*". Jpn. J. Appl. Phys. **34**, L264-L267 (1995).

83. **Ogletree, D. F., Carpick, R. W. & Salmeron, M.** "*Calibration of frictional forces in atomic force microscopy*". Rev. Sci. Instrum. **67**, 3298-3306 (1996).

84. **Cain, R. G., Biggs, S. & Page, N. W.** "*Force calibration in lateral force microscopy*". J. Coll. Interface Sci. **227**, 55-65 (2000).

85. **Piétrement, O., Beaudoin, J. L. & Troyon, M.** "*A new calibration method of the lateral contact stiffness and lateral force using modulated lateral force microscopy*". Trib. Lett. **7**, 213-220 (2000).

86. **Johnson, K. L.** "*Contact mechanics*" (Cambridge University Press, Cambridge, 1987).

87. **Sader, J. E., Larson, I., Mulvaney, P. & White, L. R.** "*Method for the calibration of atomic force microscope cantilevers*". Rev. Sci. Instrum. **66**, 3789-3798 (1995).

88. **Cleveland, J. P., Manne, S., Bocek, D. & Hansma, P. K.** "*A nondestructive method for determining the spring constant of cantilevers for scanning force microscopy*". Rev. Sci. Instrum. **64**, 403-405 (1993).

89. **Hutter, J. L. & Bechhoefer, J.** "*Calibration of atomic-force microscope tips*". Rev. Sci. Instrum. **64**, 1868-1873 (1993).

90. **Senden, T. J. & Ducker, W. A.** "*Experimental determination of spring constants in atomic force microscopy*". Langmuir **10**, 1003-1004 (1994).

91. **Sader, J. E.** "*Parallell beam approximation for v-shaped atomic force microscope cantilevers*". Rev. Sci. Instrum. **66**, 4583-4587 (1995).

92. **Digital Instruments, Topometrix, Park Scientific Instruments, Nanosensors, Olympus, Silicon-MDT & DME**. personal communication. (1996-2000).

93. **Neumeister, J. M. & Ducker, W. A.** "*Lateral, normal and longitudinal spring constants of atomic force microscopy cantilevres*". Rev. Sci. Instrum. **66**, 4583-4587 (1994).

94. Tungsten spheres were kindly provided by Ian Larson and are from the same batch as that of Cleveland *et al*. (1997).

95. **Guldberg-Pedersen, H.** "*Particle interactions: An AFM study of colloidal systems*" (, 1998).

96. **Walters, D. A., Cleveland, J. P., Thomson, N. H., Hansma, P. K., Wendman, M. A., Gurley, G. & Elings, V.** "*Short cantilevers for atomic force microscopy*". Rev. Sci. Instrum. **67**, 3583-3590 (1996).

97. **Roters, A. & Johannsman, D.** "*Distance-dependent noise measurements in scanning force microscopy*". J. Phys. Cond. Matt. **8**, 7561-7577 (1996).

98. **Salapaka, M. V., Bergh, H. S., Lai, J., Majumdar, A. & McFarland, E.** "*Multi-mode noise analysis of cantilevers for scanning probe microscopy*". J. Appl. Phys. **81**, 2480-2487 (1997).

99. **Roters, A., Gelbert, M., Schimmel, M., Rühe, J. & Johannsman, D.** "*Static and dynamic profiles of tethered polymer layers probed by analyzing the noise of an atomic force microscope*". Phys. Rev. E **56**, 3256-3264 (1997).

100. **Sader, J. E.** "*Frequency response of cantilever beams immersed in viscous fluids with applications to the atomic force microscope*". J. Appl. Phys. **84**, 64-76 (1998).

101. **Chon, J. W. M., Mulvaney, P. & Sader, J. E.** "*Experimental validation of theoretical models for the frequency response of atomic force microscope cantilever beams immersed in fluids*". J. Appl. Phys. **87**, 3978-3988 (2000).

102. **Gelbert, M., Roters, A., Schimmel, M., Rühe, J. & Johannsman, D.** "*Viscoelastic spectra of soft polymer interfaces obtained by noise analysis of AFM cantilevers*". Surf. Interface Anal. **27**, 572-577 (1999).

103. **Gelbert, M., Biesalski, M., Rühe, J. & Johannsman, D.** "*Collapse of polyelectrolyte brushes probed by noise analysis of a scanning force micsoscope cantilever*". Langmuir **16**, 5774-5784 (2000).

104. **Warmack, R. J., Zheng, X. Y., Thundat, T. & Allison, D. P.** "*Friction effects in the deflection of atomic force microscope cantilevers*". Rev. Sci. Instrum. **65**, 394-399 (1994).

105. **Meyer, E., Lüthi, R., Howald, L. & Güntherodt, H. J.** in "*Forces in Scanning Probe Methods"* (ed. Güntherodt, H. J.) 285-306 (Kluwer Academic Publishers, Amsterdam, 1995).

106. **Hazel, J. L. & Tsukruk, V. V.** "*Friction force microscopy measurements: Normal and torsional spring constants for V-shaped cantilevers*". J. Trib. **121**, 1-6 (1999).

107. **Noy, A., Frisbie, C. D., Rozsnyai, L. F., Wrighton, M. S. & Lieber, C. M.** "*Chemical force microscopy: Exploiting chemically-modified tips to quantify*

adhesion, friction and functional group distributions in molecular assemblies". J. Am. Chem. Soc. **117**, 7943-7951 (1995).

108. **Labardi, M., Allegrini, M., Salerno, M., Frediani, C. & Ascoli, C.** "*Dynamical friction coefficient maps using a scanning force and friction microscope*". Appl. Phys. A **59**, 3-10 (1994).

109. **Mitsuya, Y., Ohshima, Y. & Nonogaki, T.** "*Coupling and nonlinear effects of cantilever deflection and torsion encountered when simultaneously measuring vertical and lateral forces using the scanning probe method*". Wear **211**, 198-202 (1997).

110. **Feiler, A., Attard, P. & Larson, I.** "*Calibration of the torsional spring constant and the lateral photodiode response of frictional force microscopes*". Rev. Sci. Instrum. **accepted** (2000).

111. **Jaschke, M. & Butt, H. J.** "*Height calibration of optical lever atomic force microscopes by simple laser interferometry*". Rev. Sci. Instrum. **66** (1995).

112. **Senden, T. J., Drummond, C. J. & Kékicheff, P.** "*Atomic force microscopy: Imaging with electrical double layer interactions*". Langmuir **10**, 358-362 (1994).

113. **Drummond, C. J. & Senden, T. J.** "*Examination of the geometry of long-range tip-sample interaction in atomic force microscopy*". Coll. Surf. A **87**, 217-234 (1994).

114. **Senden, T. J. & Drummond, C. J.** "*Surface chemistry and tip-sample interactions in atomic force microscopy*". Coll. Surf. A **94**, 29-51 (1995).

115. **Ducker, W. A., Xu, Z. & Israelachvili, J. N.** "*Measurements of hydrophobic and DLVO forces in bubble-surface interactions in aqueous solutions*". Langmuir **10**, 3279-3289 (1994).

116. **Ducker, W. A. & Clarke, D. R.** "*Controlled modification of silicon nitride interactions in water via zwitterionic surfactant adsorption*". Coll. Surf. A **94**, 275-292 (1994).

117. **Lea, A. S., Andrade, J. D. & Hlady, V.** "*Compression of polyehtylene glycol chains grafted onto silicon nitride surface as measured by scanning force microscopy*". Coll. Surf. A **93**, 349-357 (1994).

118. **Burnham, N. A. & Colton, R. J.** "*Measuring the nanomechanical properties and surface forces of materials using an atomic force microscope*". J. Vac. Sci. Technol. A **7**, 2906-2913 (1989).

119. **Burnham, N. A., Dominguez, D. D., Mowery, R. L. & Colton, R. J.** "*Probing the surface forces of monolayer films with an atomic-force microscope*". Phys. Rev. Lett. **64**, 1931-1934 (1990).

120. **Weisenhorn, A. L., Hansma, P. K., Albrecht, T. R. & Quate, C. F.** "*Forces in atomic force microscopy in air and water*". Appl. Phys. Lett. **54**, 2651-2653 (1989).

121. **Moiseev, Y. N., Mostepanenko, V. M., Panov, V. I. & Sokolov, I. Y.** "*Force dependences for the definition of the atomic force microscopy spatial resolution*". Phys. Lett.A **132**, 354-358 (1988).

122. **Sokolov, I. Y.** "*On the limits of the spectroscopic ability of AFM and the interaction between an AFM tip and a sample*". Surf. Sci. **311**, 287-294 (1994).

123. **Visser, J.** "*The concept of negative Hamaker coefficients. 1. History and present status*". Adv. Coll. Interface Sci. **15**, 157-169 (1981).

124. **Chaudhury, M. K. & Good, R. J.** "*A quantitative theory of negative adsorption of nonelectrolytes caused by repulsive van der Waals forces*". Langmuir **1**, 673-678 (1985).

125. **Frenzl, W.** "*Continuous wetting transitions in systems with van der Waals interaction*". Ber. Bunsenges. Phys. Chem. **98**, 389-391 (1994).

126. **Hartmann, U.** "*Manifestation of zero-point quantum fluctuations in atomic force microscopy*". Phys. Rev. B **42**, 1541-1546 (1990).

127. **Weisenhorn, A. L., Maivald, P., Butt, H. J. & Hansma, P. K.** "*Measuring adhesion, attraction and repulsion between surfaces in liquids with an atomic force microscope*". Phys. Rev. B **45**, 11226-11232 (1992).

128. **Hutter, J. L. & Bechhoefer, J.** "*Manipulation of van der Waals forces to improve image resolution in atomic-force microscopy*". J. Appl. Phys. **73**, 4123-4129 (1993).

129. **Hutter, J. L. & Bechhoefer, J.** "*Measurement and manipulation of van der Waals forces in atomic-force microscopy*". J. Vac. Sci. Technol. B **12**, 2251-2253 (1994).

130. **Milling, A., Mulvaney, P. & Larson, I.** "*Direct measurement of repulsive van der Waals interactions using an atomic force microscope*". J. Coll. Interface Sci. **180**, 46-465 (1996).

131. **Israelachvili, J. N.** personal communication. (1996).

132. **Siedle, P. & Butt, H. J.** "*Artifacts in force measurements with the atomic force microscope due to digitization*". Langmuir **11**, 1065-1068 (1995).

133. **Bergström, L. & Pugh, R. J.** "*Interfacial characterization of silicon nitride powders*". J. Am. Ceram. Soc. **72**, 103-109 (1989).

134. **Bergström, L. & Bostedt, E.** "*Surface chemistry of silicon nitride powders: Electrokinetic behaviour and ESCA studies*". Coll. Surf. **49**, 183-197 (1990).

135. **Lo, Y. S., Huefner, N. D., W.S., C., Dryden , P., Hagenhoff, B. & Beebe, T. P.** "*Organic and inorganic contamination on commercial AFM cantilevers*". Langmuir **15**, 6522-6526 (1999).

136. **Zhmud, B. V.** "*Charge regulation at the surface of porous solids: A comparison between the results obtained using different potential-to-charge relations*". J. Coll. Interface Sci. **183**, 111-117 (1996).

137. **Brow, R. K. & Pantano, C. G.** "*Thermochemical nitridation of microporous silica films in ammonia*". J. Am. Ceram. Soc. **70**, 9-14 (1987).

138. **Hackley, V. A.** "*Colloidal processing of silicon nitride with poly(acrylic acid): I, Adsorption and electrostatic interactions*". J. Am. Ceram. Soc. **80**, 2315-2325 (1997).

139. **Biggs, S. & Healy, T. W.** "*Electrosteric stabilisation of colloidal zirconia with low-molecular-weight polyacrylic acid*". J. Chem. Soc. Faraday Trans. **90**, 3415-3421 (1994).

140. **Leong, Y. K., Scales, P. J., Healy, T. W. & Boger, D. V.** "*Interparticle forces arising from adsorbed polyelectrolytes in colloidal suspensions*". Coll. Surf. A **95**, 43-52 (1995).

141. **Pedersen, H. G. & Bergström, L.** "*Forces measured between zirconia surfaces in poly(acrylic acid) solutions*". J. Am. Ceram. Soc. **82**, 1137-1145 (1999).

142. **Foissy, A., Attar, A. E. & Lamarche, J. M.** "*Adsorption of polyacrylic acid on titanium dioxide*". J. Coll. Interface Sci. **96**, 275-287 (1983).

143. **Tjipangandjara, K. F. & Somasundaran, P.** "*Effects of changes in adsorbed polyacrylic acid conformation on alumina flocculation*". Coll. Surf. **55**, 245-255 (1991).

144. **Laarz, E. & Bergström, L.** "*The effect of anionic polyelectrolytes on the properties of aqueous silicon nitride suspensions*". J. Euro. Ceram. Soc. **20**, 431-440 (2000).

145. **Singer, I. L. & Pollock, H. M.** "*Fundamentals of friction: Macroscopic and microscopic processes"* (eds. Singer, I. L. & Pollock, H. M.) (Kluwer Academic Publishers, Dordrecht, 1992).

146. **Colchero, J., Luna, M. & Baró, A. M.** "*Lock-in technique for measuring friction on a nanometer scale*". Appl. Phys. Lett. **68**, 2896-2898 (1996).

147. **Lantz, M. A., O'Shea, S. J., Hoole, A. C. F. & Welland, M. E.** "*Lateral stiffness of the tip and tip-sample contact in frictional force microscope*". Appl. Phys. Lett. **70**, 970-972 (1997).

148. **Lantz, M. A., O'Shea, S. J., Welland, M. E. & Johnson, K. L.** "*Atomic-force-microscope study of contact area and friction on NbSe$_2$*". Phys. Rev. B **55**, 10776-10785 (1997).

149. **Carlström, E.** in "*Surface and colloid chemistry in advanced ceramics processing*" (eds. Pugh, R. J. & Bergström, L.) 245-278 (Marcel Dekker Inc., New York, 1994).

150. **Yousuff, M. & Page, N. W.** "*Particle material, morphology and load effects on internal friction in powders*". Powder Technol. **76**, 299-307 (1993).

151. **Shinohara, K., Oida, M. & Golman, B.** "*Effect of particle shape on angle of internal friction by triaxial compression test*". Powder Technol. **107**, 131-136 (2000).

152. **Chan, L. C. Y. & Page, N. W.** "*Particle fractal and load effects on internal friction in powders*". Powder Technol. **90**, 259-266 (1997).

153. **Zhang, Y., Tang, X., Uchida, N. & Uematsu, K.** "*Binder surface segregation during spray drying of ceramic slurry*". J. Mater. Res. **13**, 1881-1887 (1998).

154. **Baklouti, S., Chartier, T. & Baumard, J. F.** "*Binder distribution in spray-dried alumina agglomerates*". J. Euro. Ceram. Soc. **18**, 2117-2121 (1998).

155. **Shinohara, N., Okumiya, M., Hotta, T., Nakahira, K., Naito, M. & Uematsu, K.** "*Effect of seasons on density, strength of alumina*". Am. Ceram. Soc. Bull. **78**, 81-84 (1999).

156. **Whitman, D. W., Cumbers, D. I. & Wu, X. K.** "*Humidity sensitivity of dry-press binders*". Am. Ceram. Soc. Bull. **74**, 76-79 (1995).

157. **Wu, X. K., Whitman, D. W., Kaufell, W. L., Finch, W. C. & Cumbers, D. I.** "*Acrylic binders for dry pressing ceramics*". Ceram. Eng. Sci. Proc. **18**, 422-438 (1997).

158. **Persson, B. N. J.** "*Sliding friction: Physical principles and applications*" (Springer Verlag, Berlin, 1998).

159. **Reed, J. S.** "*Introduction to the principles of ceramic processing*" (John Wiley & Sons, New York, 1988).

160. **Erlandsson, R., Hadziioannu, G., Mate, C. M., McClelland, G. M. & Chiang, S.** "*Atomic scale friction between the muscovite mica cleavage plane and a tungsten tip*". J. Chem. Phys. **89**, 5190-5193 (1988).

161. **Liu, Y., Wu, T. & Evans, D. F.** "*Lateral force microscopy study on the shear properties of self-assembled monolayers of dialkyammonium surfactant on mica*". Langmuir **10**, 2241-2245 (1994).

162. **Israelachvili, J. N.** "*Measurement of the viscosity of liquids in very thin films*". J. Coll. Interface Sci. **110**, 263-271 (1986).

163. **Berman, A. D., Ducker, W. A. & Israelachvili, J. N.** "*Origin and characterization of different stick-slip friction mechanisms*". Langmuir **12**, 4559-4563 (1996).

164. **Carlson, J. M. & Batista, A. A.** "*Constitutive relation for the friction between lubricated surfaces*". Phys. Rev. E **53**, 4153-4165 (1996).

165. **Thompson, P. A. & Robbins, M. O.** "*Origin of stick-slip motion in boundary lubrication*". Science **250**, 792-794 (1990).

166. **Robbins, M. O. & Thompson, P. A.** "*Critical velocity of stick-slip motion*". Science **253**, 915-917 (1991).

167. **Carpick, R. W., Ogletree, D. F. & Salmeron, M.** "*A general equation for fitting contact area and friction vs load measurements*". J. Coll. Interface Sci. **211**, 395-400 (1999).

168. **Dorier, C. & Tichy, J.** "*Behaviour of a Bingham-like viscous fluid in lubrication flows*". J. Non-Newt. Fluid Mech. **45**, 291-310 (1992).

169. **Jang, S. & Tichy, J.** "*Rheological models for stick-slip behaviour*". J. Trib. **119**, 626-631 (1997).

170. **Batista, A. A. & Carlson, J. M.** "*Bifurcations from steady sliding to stick slip in boundary lubrication*". Phys. Rev. E **57**, 4986- (1998).

171. **Yoshizawa, H. & Israelachvili, J. N.** "*Fundamental mechanisms of interfacial friction. 2. Stick-slip friction of spherical and chain molecules*". J. Phys. Chem. **97**, 11300-11313 (1993).

ACKNOWLEDGEMENTS

I would like to thank Dr Lennart Bergström, not only for sharing his scientific knowledge and being a good supervisor, but also for many friendly moments during all these years.
I am also indebted to Prof. Paul Luckham and Prof. David Rowcliffe for help during the early years.

Dr Henrik Guldberg-Pedersen and Dr Ian Larson, I owe you a big part of this thesis. Henrik for so many things outside the lab, and Ian for just about everything.

Dr Mark Rutland – it's been a real pleasure working with you. Thanks for the proof-reading.

Dr Joseph Yanez, another friendly acquaintance, also contributing to my scientific papers.

Peter and Eric at YKI have been two best friends throughout this period. Good luck and thanks for everything!

Evgeni, Locky and Goran – thanks for a perfect mix of collaboration, friendship and CD-swapping.

Brian Sundlof is thanked for thorough proof-reading.

Andzelika, without you I would still be looking for petri-dishes, plastic cups and glue.

Boris and Ann-Charlotte for great collaboration. Katrin – always willing to discuss friction.

Peder, Ingvar, Britt, Ann, Annika O and many others at YKI for always taking time when being asked.

Gavin, Parbin, Asad, Mani, Giuseppe, Richard and Kate at Imperial College for a great time.

My sister, mother and father, and friends for continuos personal encouragement.

Finally, my love Karin, thanks for your support, professional collaboration and the essence of life.